Hybrid NeuroMEMS: Simultaneous Recording of Neural Electro-potentials and Neural Biomarkers

Thesis by

Mohamad Hajj Hassan

Department of Electrical and Computer Engineering

McGill University, Montreal

February 2010

A thesis submitted to McGill University in partial fulfillment of the requirements of the Degree of

Doctor of Philosophy

Acknowledgements

I would first and foremost like to express my gratitude to my advisor, Professor Vamsy Chodavarapu. Without his advice, guidance, and support, I would not have accomplished what I have achieved in my three years at McGill University. What I learnt from him is far beyond research.

The interdisciplinary nature of my work has allowed me to have many great collaborators. I would like to thank Prof. Sam Musallam, Prof. Mark Andrews, and Prof. Janet Henderson. They have provided much guidance and assistance for my research and gave me very helpful proofreading of my published articles.

The same gratitude goes to all my colleagues in the Sensor Microsystems Laboratory: Maurice Cheung, Ebrahim Ghafar-Zadeh and Lei Yao for their assistance in my projects.

I am deeply grateful to my parents, my sister, Fatima, and my brother, Houssein, and his family who are always there for me. Finally, my deepest gratitude is to my wife Roba Hajj-Hassan, with whom I am so lucky to be married. Her support and encouragement are a constant source of power enabling me to face any challenge. Our son, Ali Hajj-Hassan, has been growing up during the time I was writing this thesis deserves attention; his smiles and laughter always keep me optimistic, energized, and inspired.

Abstract

Neural microelectrodes are an important and essential component in neuroscience and neural prosthetics. Single or arrays of microelectrodes are implanted in different areas of the brain to record and/or stimulate specific sites in the brain. They are currently used in many clinical settings for diagnosis of brain diseases such as seizers, epilepsy, migraine, Alzheimer's, and dementia. They are used to stimulate sub-cortical structures in patients with Parkinson's disease. At the same time, they assist paralyzed patients by allowing them to operate computers or robots using their neural activity. In neural prosthetic systems, implanted microelectrodes record the electrical potentials generated by specific thoughts and relay the signals to algorithms/robots trained to interpret these thoughts and perform specific actions.

The work in this thesis is focused on developing novel elongated multi-site multimodal neural electrodes that can record electrical signals and brain tissue oxygenation. These electrodes reach depths greater than 10mm in the brain. The majority of the research efforts have concentrated on the fabrication and integration of optical biochemical sensors with neural microelectrodes. The neural biomarker sensors are made using sol-gel derived xerogel thin films that encapsulate specific analyte responsive luminophores in their nanostructured pores. The desired neural biomarker is brain tissue oxygenation. These contributions have led to the first prototype demonstration of a hybrid silicon neural probe integrating a fiber optic coated with oxygen (O_2)-responsive xerogel inside the neural microelectrodes. The recording of brain tissue oxygenation along with electrical activity could help the

development of intelligent neural prosthesis/brain machine interfaces as well as aid in providing new foresights into complex brain diseases and disorders.

Compared with the traditional silicon neural probes, our microfabricated multimodal neural probes (being reinforced) are much longer and stronger microelectrodes (10.5 mm long, able to penetrate the *pia* layer in the brain) with lower stress and better penetration ability. These multimodal probes provide additional signals which will increase the information yield when compared to standard probes that record just electro-potentials. At the same time, our new probe arrays are shown to improve biocompatibility (with their surface textured with porous silicon).

In the future, based on the principles described here, monitoring of many other biomarkers including glucose, pH, and neurotransmitters is possible. This can be achieved by integrating various optical biochemical sensors that are responsive to these biomarkers with neural electrodes.

Résumé

En neuroscience et neuroprosthétique, des matrices de microélectrodes sont implantées dans différentes régions du cerveau pour enregistrer les activités électriques des neurones. Elles sont utilisées pour diagnostiquer des maladies comme l'épilepsie, Alzheimer et la démence ou pour stimuler des structures sous corticaux chez les patients atteints de la maladie De Parkinson. En même temps, ces électrodes aident les personnes paralysées à opérer et contrôler des ordinateurs ou des robots en utilisant leurs activités électriques neuronales. Les microélectrodes enregistrent ces signaux électriques qui sont produites par les pensées du patient et les transmettent à l'extérieur du cerveau pour être traités par des algorithmes dédiés à interpréter ces pensées.

Les électrodes neuronales commerciales peuvent seulement enregistrer les signaux électriques des neurones. Dans ce projet, nous proposons l'intégration des sondes optiques avec des électrodes longues et renforcées ce qui permet d'enregistrer simultanément les activités électriques neuronales et la variation de concentration de l'oxygène dans le cerveau. Grâce à ces électrodes hybrides longues et renforcées, l'accès à des régions plus profondes du cerveau pour chercher plus d'informations est possible, plus d'informations sur le fonctionnement du cerveau et le transfert des signaux entre les différentes régions qui constituent le cerveau peuvent être obtenues ce qui nous permet finalement de contrôler plus précisément les prothèses neuronales et aussi nous aide à mieux diagnostiquer les maladies du cerveau.

TABLE OF CONTENTS

CHAPTER 1 16
NEURAL PROBES 16
1.1 History of Neural Probes 16
1.2 Background for Neural Probes 18
1.3 Traditional Neural Probes 20
1.4 Silicon Based Neural Probes 24
1.5 Bulk Micromachining 25
1.6 Surface Micromachining 26
1.7 Silicon on Insulator (SOI) Based Neural Probes 30
1.8 Polymer Based Neural Probes 33
1.9 Applications of Neural Probes for Neural Prosthesis 35
1.10 Biocompatibility of Neural Probes 36
1.11 Summary 38
1.12 Dissertation Goals and Organization 39
CHAPTER 2 42
REINFORCEMENT OF NEURAL PROBES 42
2.1 Probe Design and Characteristics 44
2.2 Analytical Modeling of Neural Probe Mechanics 46
2.3 Numerical Modeling of Reinforced Electrodes 52
2.4 Fabrication Process of the MicraGem Array 56
2.5 Fabrication Process of the McGill Array 59
2.6 Mechanical Testing of the Electrodes 62
2.7 Summary 68
CHAPTER 3 70
OXYGEN SENSORY PLATFORM 70
3.1 Fluorescence Sensing 72
3.2 Fluorescence Detection from Xerogel-Based Sensors 73
3.3 Direct-Dispense Fabrication of Waveguide Structures 75
3.4 Xerogels Based Biochemical Sensor Arrays 79

3.1.1 Preparation of the Xerogel Oxygen (O2) Sensors 80
3.5 Experimental Results and Discussion 82
3.6 Summary 84
CHAPTER 4 86
HYBRID NEURAL PROBES 86
4.1 Design and Fabrication of the Hybrid Neural Microelectrodes 87
4.2 Preparation and Evaluation of Xerogel Based Oxygen Sensor 95
4.3 In Vivo Recording 96
4.4 Summary 97
CHAPTER 5 98
BIOCOMPATIBLE INTERFACE: POROUS SILICON 98
5.1 Fabrication of Porous Silicon 100
5.2 Fabrication of Porous Silicon Using XEF_2 101
5.3 Optical Characterization of the Porous Silicon Samples 105
5.4 Cell Culture 107
5.1.1 Materials and Methods 107
5.2.1 Results 108
5.3.1 Discussion 112
5.5 Summary 113
CHAPTER 6 115
CONCLUSION 115

LIST OF FIGURES

Figure 1-1: (a) Illustration of the use of neural probe to detect neural signals from the brain; (b) the use of multiple electrodes for recording extracellular neural signals. Taken from [59]. 18
Figure 1-2: Scanning electron micrographs of microelectrodes made with: (a) DC electropolishing technique; (b) Standard AC electroetching. Taken from [40]..... 21
Figure 1-3: (a) Floating multi-electrode array with short and long electrodes; (b) An SEM micrograph of an electrode used in the floating multi-electrode array (FMA) pretreated with A-174 Silane before being insulated with 3mμ of Parylene-C. The tip was exposed by a non-thermal ablation technique using a dual beam Eximer laser system. Taken from [43] and [63] respectively. 22
Figure 1-4: SEM Micrographs of: (a) Seven array microelectrode tip regions; (b) The Parylene electrode in a Parylene window on the tip. Taken from [64]..... 23
Figure 1-5: Electrodeposition of the mechanical layer in the probe shank. The SEM image shows the seed-layer regions that are not plated and those previously plated. The inset image on the low left shows the finished tip of the electroplated microprobe. Taken from [68]. 23
Figure 1-6: Illustration of bulk micromachining and surface micromachining. Taken from [59]. 25
Figure 1-7: (a) Scanning electron microscopy side view of a silicon probe substrate defined using a shallow (tip) and deep (shank) boron etch-step (above) and perspective view (below); (b) Photo of a 3-D 1024-site 128-channel neuroelectronic interface. Taken from [85]. 28
Figure 1-8: SEM micrograph of: (a) The Utah array; (b) The insulation coated electrodes with exposed platinum tips. Taken from [101]..... 29
Figure 1-9: Electrodes at the tip of each probe are separated by 45 μm spacing. Each electrode is 20μm x 20μm square. Taken from [84]. 31
Figure 1-10: Scanning electron micrograph of (a) A silicon probe with 1 shaft x 32 electrodes; (b) Close-up of a probe tip designed with 4^{o} taper angle. The interconnect lines shown are 1μm wide; (c) Close-up of a 10 μm x 10 μm Ir electrode site. Taken from [103]. 32
Figure 1-11: Scanning electron micrograph showing selectively opened electrode windows in the Si3N4 layer on a 64-site probe. Bright squares are opened windows. Distances shown are in micrometers. Taken from [106]. 32
Figure 1-12: 3D flexible probe array after folding. The recording pads are vertically aligned. [112]. 33
Figure 1-13: Optical microscope images of the polyimide neural probes (a) View of the electrode; (b) Top view of the three shanks. Taken from [113]..... 34

Figure 1-14: Schematic of the pathway of information flow for the cognitive-based neural prosthetic paradigm. 36
Figure 1-15: Design of the multimodal neural microelectrode combining neural electrical activity recording and optical sensor waveguiding structures. 39
Figure 2-1: Design of the two developed neural microelectrode array showing the recording sites, interconnects, and bond pads a) MicraGem array; b) McGill array. The figure is not to scale. 45
Figure 2-2: Meninges of the central nervous system. Taken from [139]. 46
Figure 2-3: Illustration of neural probe deflections during the insertion phase (a) without deflection; (b) bending; (c) buckling. 47
Figure 2-4: Geometric diagram of a single tapered probe electrode. 52
Figure 2-5: Behavior of the 2.5mm ((a),(b)); 4.5 mm ((c),(d)); and 6.5mm ((e),(f)) probes, without and with reinforcement respectively, when they are subjected to axial horizontal force. 55
Figure 2-6: Behavior of the 10.5mm long probe electrodes, (a) Without; (b) With reinforcement, when they are subjected to axial horizontal force. 56
Figure 2-7: Schematic illustration of the standard MicraGem microfabrication process. 57
Figure 2-8: SEM photos of the fabricated array using the standard MicraGem process (a) probe array; (b) tip of the electrode; (c) reinforced electrode at the middle region; (d) non-reinforced electrode. 59
Figure 2-9: Schematic illustration of the steps involved in the fabrication process of the McGill neural probe array. The figure is not to scale. 60
Figure 2-10: Microphotographs of the fabricated electrode array. (a) Picture of the fabricated electrode array; (b) Close-up view of the probe tip and the three 10μmx10μm recording sites; (c) Picture of the reinforcing structures; (d) View of the tapered base of the electrodes; (e) Cross-sectional view of the probe electrode. 61
Figure 2-11: The equivalent circuit of a microelectrode. 62
Figure 2-12: Impedance of the recording sites at 1 KHz. 63
Figure 2-13: Spikes and Local Field Potentials (LFPs) recorded from the rat barrel cortex. 64
Figure 2-14: Diagram of single probe electrode under buckling deflection condition. 65
Figure 2-15: Neural probe mounted on Printed Circuit Board (PCB). 66
Figure 2-16: Buckling testing of MicraGem and McGill arrays when pressed against hard plastic surface. 67
Figure 3-1: Representation using Jablonski diagram. Taken from [169]. 72
Figure 3-2: Simplified block diagram of the optical sensor system implementing the polymeric waveguide support platform and xerogel recognition materials. 74
Figure 3-3: Direct-dispense microfabrication system. 76

Figure 3-4: Fabrication process flow for the development of polymeric waveguide support platform using direct-dispense process and the immobilization of xerogel materials. 77
Figure 3-5: Microstructures fabricated using direct-dispense technique. (a) Microscopic image of a fabricated 500 μm diameter microchannel on a Printed Circuit Board (PCB); (b) Serpentine microchannel with an inner diameter of 150 μm and 200 μm outer diameter. 77
Figure 3-6: Fabricated epoxy waveguides using the direct-dispense deposition technique. (a) Shows the top-view of the fabricated 100 μm wide ridge waveguides spaced 75 μm apart with a pencil tip as reference; (b) Magnified top-view of a selected portion of the waveguides; (c) Multimode epoxy waveguides which conduct light from a blue (λpeak = 470 nm) LED; (d) Cross-sectional view of the waveguides; (e) Magnified top-view of the transparent waveguides under intense optical illumination which shows the straightness and reproducibility of the structures; (f) Deposited xerogel after aging. 79
Figure 3-7: Response of the O2 responsive xerogel sensor materials. 83
Figure 3-8: Stern-Volmer response of the xerogel O2 sensors. 84
Figure 4-1: Design of the multimodal neural microelectrode with integrated electro-potential recording and optical sensor waveguiding structures. 89
Figure 4-2: Fabrication process of the hybrid neural probe. (a) Dicing of silicon substrate; (b) Patterning of the metal layer to form the recording sites; (c) Etching of a rectangular cavity; (d) Patterning of the silicon substrate to form the neural electrode; (e) Deposition, patterning, and etching of Parylene C to expose the recording site and the bonding pad. 91
Figure 4-3: Microscope images of the fabricated hybrid multimodal neural probe (a) The 2-electrode hybrid neural array; (b) Close-up image of the probe electrodes; (c) Magnified view of the electro-potential recording site and the cavity hosting the optical sensors; (d) SEM image showing two cavities with enfaces spaced 1mm apart and neighboring two recording sites on the same neural electrode; (e) Magnified view of one recording site and an etched cavity; (f) SEM image showing two etched cavities and two bonding pads. 94
Figure 4-4: Measurement of the O_2 variation in area 5 in the parietal cortex of a nonhuman primate using O_2 responsive xerogel sensor. 97
Figure 5-1: Etch menu features 102
Figure 5-2: SEM images of the fabricated porous silicon samples with various pore sizes using XeF_2 dry etching process. (a) Sample A; (b) Sample B; (c) Sample C… 104
Figure 5-3: Cross-sectional SEM image of the porous silicon material (Sample B). 105
Figure 5-4: High resolution SEM images showing the top and bottom surface of the pore structures for the porous silicon samples. (a) Sample A; (b) Sample B; (c) Sample C. 106

Figure 5-5: Toluidine stain of mesenchymal stem cell on tissue culture plastic day 3, 4X. 107
Figure 5-6: Toluidine stained mesenchymal stem cell of tissue control plastic, day 6 4X. 108
Figure 5-7: Samples immersed in Alamar blue reagent 109
Figure 5-8: (a) This graph demonstrates the Alamar blue calculations for the plate 1 of the experiment four which consisted of triplicates of 0µm, 20µm, 30µm and tissue culture plastic. The right hand side graph; (b) This graph is the calculation taken for measuring the reduction of Alamar blue on a plate that consisted of same types of porous silicon as plate one except that instead of the tissue culture plastic, smooth titanium disks were used. There is a trend of increase in cell activity in both plates up until day 9. The cells grow better on the porous silicon wafers of 30µm pore size compare to the 20µm, 0µm and TCP. 110
Figure 5-9: (a) This graph demonstrates the Alamar blue calculations done on experiment five which was focused on comparing cell growth on porous silicon wafer with the pore size of 30µm and 20µm with the smooth surfaced titanium disks and the tissue culture plastic. The results indicate a growing trend of cells until day 9; the cells growth is more efficient on porous silicon of 20µm pore size. The graph on the right side; (b) This graph demonstrates the number of cells counted at three different time intervals. The numbers of cells are increasing up until day 9 and there are more cells located on the tissue culture plastic. 110
Figure 5-10: High resolution SEM images for stem cells growing on the 20 micron etched porous silicon sample 112

LIST OF TABLES

Table 2.1: Comparative buckling simulations results of the reinforced and non-reinforced electrodes of the Micragem and McGill arrays. 53
Table 2.2: Comparative buckling test results of different lengths of the reinforced and non-reinforced electrodes..... 68

PATENTS AND PUBLICATIONS

PROVISIONAL PATENT:

- "Localized Multiple Measurand Solid State Brain Probe", **M. Hajj-Hassan**, V. P. Chodavarapu, and S. Musallam, United States Provisional Patent 61/222,525. Filed: July 2, 2009.

REFEREED JOURNAL PUBLICATIONS:

- **M. Hajj-Hassan**, M. Cheung, V. Chodavarapu, *"Dry Etch Fabrication of Porous Silicon using Xenon Difluoride"*, Accepted for publication in Micro & Nano Letters, 2010.

- **M. Hajj-Hassan**, V. Chodavarapu, S. Musallam, "*Reinforced Silicon Neural Microelectrode Array Fabricated Using a Commercial MEMS process"*, SPIE Journal of Micro/Nanolithography, MEMS, and MOEMS, vol. 8(3), 2009. **(Selected for Virtual Journal of Biological Physics Research, Vol. 8, issue 3, August 2009).**

- **M. Hajj-Hassan**, V. Chodavarapu, S. Musallam, "*Microfabrication of Ultra-long Reinforced Silicon Neural Electrodes"*, Micro & Nano Letters, vol. 4, pp. 53-58, 2009. **(Featured Letter of the Issue)**

- **M. Hajj-Hassan**, T. Gonzalez, E. Ghafer-Zadeh, H. Djeghelian, V. Chodavarapu, M. Andrews, D. Therriault, "*Direct-Dispense Polymeric Waveguide Platform for Optical Chemical Sensors"*, Sensors, vol. 8, pp. 7636-7648, 2008.

- **M. Hajj-Hassan**, V. Chodavarapu, S. Musallam, *"NeuroMEMS: Neural Probe MicrotechnologieS"*, Sensors, vol. 8, pp. 6704-6726, 2008. **(Special Issue on BioMEMS).**

- **M. Hajj-Hassan**, S. J. Kim, M. Cheung, V. Chodavarapu, A. Cartwright, "*Porous Silicon and Porous Polymer Substrates for Optical Chemical Sensors"*, Submitted to SPIE Journal of Nanophotonics, January, 2010.

- **M. Hajj-Hassan,** M. Khayyat-Kholghi, H. Wang, V. Chodavarapu, J. E. Henderson, *"Response of Murine Bone Marrow-Derived Mesenchymal Stromal Cells to Dry-Etched Porous Silicon Scaffold"*, to be submitted to Journal of Biomaterials.

- **M. Hajj-Hassan,** C. Gross, V. Chodavarapu, S. Musallam, *"Multimodal Neural Probe Combining Microelectrode Arrays with Nanostructured Optical Oxygen Sensors"*, to be submitted to Journal of IEEE Transactions on Biomedical Engineering.

- M. Cheung, P.J.R. Roche, **M. Hajj-Hassan**, Andrew K. Kirk, V. Chodavarapu, *"Controlling Porosity and Optical Properties of Porous Silicon by optimization of a new hydrogen fluoride & dry etch Xenon fluoride process"*, to be submitted to Journal of Nanotechnology.

REFEREED CONFERENCE PROCEEDINGS AND PRESENTATIONS:

- **M. Hajj-Hassan**, M. Cheung, T. Gonzalez, V. Chodavarapu, M. Andrews, *"*Dry *etched nanoporous silicon substrates for optical biosensors"*, Proceedings of SPIE Photonics West (BiOS), San Francisco, 2010.

- **M. Hajj-Hassan**, S. Musallam, T. Gonzalez, E. Ghafer-Zadeh, D. Therriault, V. Chodavarapu, M. Andrews, *"Brain Machine Interfaces Combining Microelectrode Arrays with Nanostructured Optical Biochemical Sensors"*, Proceedings of SPIE Photonics West (BiOS), San Jose, 2009.

- M**. Hajj-Hassan**, T. Gonzalez, E. Ghafer-Zadeh, V. Chodavarapu, M. Andrews*, "Optical Biochemical Sensors by Direct-Writing of Nanostructured Recognition Elements*", Proceedings of 30th IEEE EMBS Conference, Vancouver, 2008. ***(Invited Paper)*.**

- **M. Hajj-Hassan**, T. Gonzalez, H. Djeghelian, E. Ghafer-Zadeh, D. Therriault, V. Chodavarapu, M. Andrews, "*Direct-write Patterning of Nanostructured Sensory Waveguides for Integrated Optical Bioimaging Applications*", Proceedings of SPIE Photonics West (BIOS), San Jose, 2008. ***(Invited Paper)*.**

- Lei Yao, **M. Hajj-Hassan**, Vamsy Chodavarapu, Arghavan Shabani, Beatrice Allain, Mohammed Zourob, Rosemonde Mandeville, "*CMOS Imager Microsystem for Multi-Bacteria Detection*", IEEE-CCECE 2008, Ontario, 2008.

- L. Yao, **M. Hajj-Hassan**, V. Chodavarapu, A. Shabani, M. Zourob, R. Mandeville, "*CMOS Capacitive Sensor System for Bacteria Detection Using Phage Organisms*", IEEE-NEWCAS, Montréal, 2008.

CONTRIBUTIONS OF AUTHORS

This thesis is based on five different published manuscripts. The candidate, Mohamad Hajj Hassan, is the primary author for all these manuscripts.

Chapter 1 is based on the review paper published by our group entitled "NeuroMEMS: Neural Probe Microtechnologies" Sensors, vol. 8, pp. 6704-6726, 2008.

Chapter 2 is based on the following two papers: **M. Hajj-Hassan**, V. Chodavarapu, S. Musallam, "Reinforced Silicon Neural Microelectrode Array Fabricated Using a Commercial MEMS process",SPIE Journal of Micro/Nanolithography, MEMS, and MOEMS, vol. 8(3), 2009., and **M. Hajj-Hassan**, V. Chodavarapu, S. Musallam "Microfabrication of Ultra-long Reinforced Silicon Neural Electrodes", Micro & Nano Letters, vol. 4, pp. 53-58, 2009.

Chapter 3 is based on the following paper: **M. Hajj-Hassan**, T. Gonzalez, E. Ghafer-Zadeh, H. Djeghelian, V. Chodavarapu, M. Andrews, D. Therriault, "Direct-Dispense Polymeric Waveguide Platform for Optical Chemical Sensors" Sensors,vol. 8, pp. 7636-7648, 2008. The xerogel sensors used in this paper were prepared by Timothy Gonzalez and Hagop Djeghelian. Ebrahim Ghafar-Zadeh helped in setting up the direct dispense robotic system to fabricate the ridge sensory waveguides.

Chapter 5 is based on the paper accepted for publication in Micro & Nano Letters, January 2010, and which is entitled "Dry Etch Fabrication of Porous Silicon using Xenon Difluoride", Maurice Cheung helped to optically characterize the porous silicon samples. The stem cell culture was performed by Maedeh Khayyat Kholghi.

CHAPTER 1

NEURAL PROBES

Neural probe technologies have already had a significant positive effect on our understanding of the brain by revealing the functioning of networks of biological neurons. Probes are implanted in different areas of the brain to record and/or stimulate specific sites in the brain. We find these devices assisting paralyzed patients by allowing them to operate computers or robots using their neural activity. In recent years, probe technologies were assisted by rapid advancements in microfabrication and microelectronic technologies and thus are enabling highly functional and robust neural probes which are opening new and exciting avenues in neural sciences and brain machine interfaces. With a wide variety of probes that have been designed, fabricated, and tested to date, this chapter is meant to familiarize the reader with the fundamental concepts governing the development neural probes and aims to provide an overview of the advances and recent progress in the microfabrication techniques of neural probes. In addition, we aim to highlight the challenges faced in developing and implementing elongated multi-site recording probes that are needed to monitor neural activity from deeper regions in the brain. Finally, we review techniques that can improve the biocompatibility of the neural probes to minimize the immune response and encourage neural growth around the electrodes for long term implantation studies.

1.1 History of Neural Probes

Scientists have strived to understand the nervous system and develop treatments for its disorders for many centuries. The first documented use of electrical current as a strategic approach to overcome a neural disease (paralysis) can be traced back to the year 1757 [1]. Many of the early research initiatives that investigated the possibility of using electrical signals to cure neural diseases can be found in the review by McNeal

[2]. In the year 1939, Hodgkin and Huxley first demonstrated the recording of action potentials from inside a nerve fiber [3]. Again in 1952, the group analytically described the mechanism of nerve excitation and the subsequent generation of action potentials [4-5]. Over the past several years, neural electrodes or probes became a key tool to record the action potentials from neurons [6-7], stimulate specific brain regions [8-15], and ultimately understand the functioning of the brain. The stimulation and recording from a single neuron [16-18] or complex networks of neurons using multiple electrodes [19-23] in cortical and sensory areas in brain [24-26] help in understanding various neural characteristics such as population encoding [27-28], somatosensory organization [29-31], nervous system behavior [32-34], and network connectivity [21].

To date, a wide range of neural electrodes have been used in basic neuroscience and neural prosthetic research (brain machine interfaces) starting with the early electrolyte-filled micropipettes [6, 35-38] and later metal electrodes to the current emerging MicroElectroMechanical Systems (MEMS) based electrodes and polymer electrodes. Since the 1950s, single wire metal microelectrodes have been commonly used to record electrical activity in the extracellular environments. These electrodes consist of an insulated metal wire except for the wire tip which represents the recording site [39-40]. Multiple metal electrode arrays have been used that are made of wire bundles [41], gluing individual metal wire electrodes together [42] or assembling several metal wires on a ceramic plate [43]. During 1970s, Wise and Angell took advantage of the developments in thin-film and integrated circuit microfabrication techniques and reported pioneering work on the first silicon-based microprobes to interface neural tissues [44]. Since then, widespread use of silicon micromachining techniques to develop miniaturized neural probes and probe arrays have led to the establishment of the field of Neural MEMS or NeuroMEMS [44-50]. More recently, polymeric microprobes have received a great deal of attention owing to their simple fabrication process, flexibility and biocompatibility [51-57]. For instance, polyimide based neural probes have been developed that are flexible and mechanically resistant with integrated electrodes on one or both sides of the shank [54] and others

have been reported with integrated microtank and microchannels for targeted drug delivery [51]. More recently, some research groups are aiming to develop hybrid neural probes which have the combined capability to record electrical activity as well as specific neural biochemical markers [58].

1.2 Background for Neural Probes

Neural probes are microstructures that form the connection between the biological neural tissue with physical devices and electronics. Typically, a MEMS-based neural probe consists of a single long protruding structure or electrode (of lengths ranging from 200μm to 15mm) preferably with thin thickness (thicknesses ranging from 10μm to 200μm). The electrode includes the recording sites, interconnect traces and back carrier area carrying the bonding pads to connect the probes to electronics. To really understand the signal processing performed in complex neural networks it quickly became clear that arrays of electrodes, and perhaps large arrays, would be needed. Figures 1.1(a) shows the typical neural signal (action potential) that the neural probes are used to detect from the brain. The illustration of the use of multiple electrodes for recording of extracellular neural signals is shown in Figure 1.1(b).

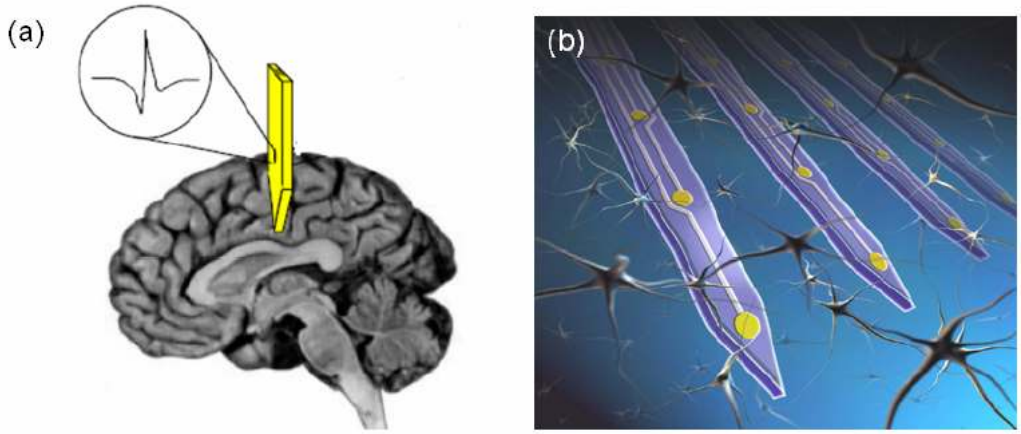

(a) **(b)**

Figure 1-1: (a) Illustration of the use of neural probe to detect neural signals from the brain; (b) the use of multiple electrodes for recording extracellular neural signals. Taken from [59].

Implantable neural probes for neuroscience and brain machine interfaces are generally preferred to have a minimum footprint as possible to minimize neural damage and incorporate structural features that facilitate easy entry and movement through the brain tissue. The smaller footprint for the neural probe will allow the probe to approach the target neurons as closely as possible and thus improving the signal-to-noise ratio of the recorded activity or target a very specific region to be stimulated. Further, there is growing need to insert large numbers of accurately spaced recording sites into small volumes which is promoting the application of thin-film and micromachining techniques to the microelectrode production. Ideally, electrodes with minimum thickness are preferred to reduce damage to the tissue when the probe is inserted into the brain. Moreover, miniaturization of the neural probes is very crucial to approach and efficiently interface the neural tissue at the scales of neural cells whose size typically range between 10 and 50μm in diameter and spaced 20nm apart [60]. In contrast, the electrode has to be wide enough to hold many recording sites to measure neural electrical activity at different depths and route interconnect traces to connect the recording sites to the bonding pads. In addition, the probes should incorporate sufficient mechanical strength to survive the compression and tension forces during the insertion and retraction phases respectively while implantation.

Many research groups investigating neural probe technologies are faced with different challenges including non-standard and unconventional fabrication processes leading to low yield and high cost, lack of on-site and monolithic Integrated Circuit (IC) integration leading to high noise and reduced sensitivity, shorter sized probes mainly limited by fabrication technology, low design flexibility, and limited selection of materials having the mechanical properties that fulfill both the implantation application requirements and being compatible with standard microfabrication processing. In addition, biocompatibility of the neural probes to minimize the foreign-body immune response plays an important role in determining long-term function of neural probes during implantation. These parameters in combination ultimately determine the microfabrication process needed to manufacture the neural probes.

1.3 Traditional Neural Probes

Metal neural probe, which enabled the initiation of many pioneering studies in neural sciences, represents one of the most widely used neural probes [12]. A metal neural probe typically consists of electrolytically sharpened wires that are commonly less than 100μm in diameter and are completely insulated except for a small exposed area at the tip which forms the recording or stimulation site. The electrodes have a tapered structure to enable convenient insertion in the brain tissue. The tapered structure is achieved by dipping the electrodes into an etching solution and slowly drawing out the electrode from the solution. For example, a tungsten wire can be tapered using a sodium hydroxide (NaOH) solution [61]. By varying the composition of the etching solution and speed with which the wire is drawn from the etchant one can control the taper of the electrode.

Typically used electrode materials include platinum, iridium, platinum-iridium, gold, stainless steel, tungsten, and molybdenum. Quartz glass, Teflon, polyimide, and Parylene materials are used for the insulation of these electrodes. The insulating materials ideally should have a high dielectric constant in order to minimize stray capacitances affecting the electrode during recording. A multiple-electrode array of these insulated wires can be made by gluing individual metal wire electrodes together or by using cut-off wire bundles. For instance, Vassiliy Tsytsarev *et al.* [62] have developed a new 8x8 planar array of metal electrodes for in vivo multisite extracellular recording from a rat auditory cortex. The electrode array was formed by alternately gluing, with epoxy, insulated platinum wire electrodes and insulated copper wire spacers. The array of wires was covered by polyethylene tubing and then inserted into stainless steel tubing. The electrode array was connected to the commercial MED64 system from Panasonic which is comprised of an integrated amplifier, connector, and software for data acquisition and analysis.

The exposed or non-insulated area of metal wire electrodes which forms the recording site is further processed for manipulating the impedance of the site. For instance,

Skrzypek and Keller covered a tungsten rod with polymethyl methacrylate (PMMA) and placed it in a Scanning Electron Microscope (SEM) such that the desired area on the probe tip was exposed by manual control of the SEM electron beam. The sample probes are shown in Figure 1.2 [40]. The degraded PMMA was removed using a solution of ethyl alcohol.

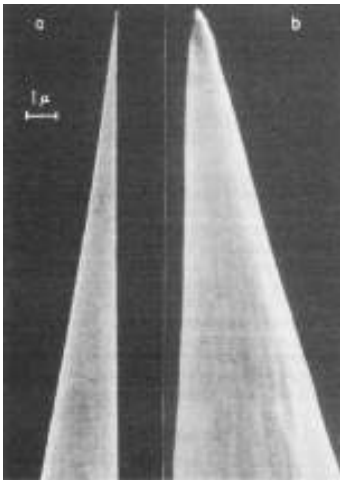

Figure 1-2: Scanning electron micrographs of microelectrodes made with: (a) DC electropolishing technique; (b) Standard AC electroetching. Taken from [40].

More recently, Musallam *et al.* has reported a floating array of metal probe by employing laser machining of a ceramic substrate to form recording holes [43]. The laser drilled holes are 90μm wide to accommodate electrodes having a diameter of 80μm. The probe wires are then coated with Parylene-C for insulation and the wire tips are exposed using a dual beam Eximer laser. The fabricated floating array is shown in Figure 1.3(a). The use of Eximer laser to etch Parylene-C was reported by Schmidt *et al.* as shown in Figure 1.3(b) [63].

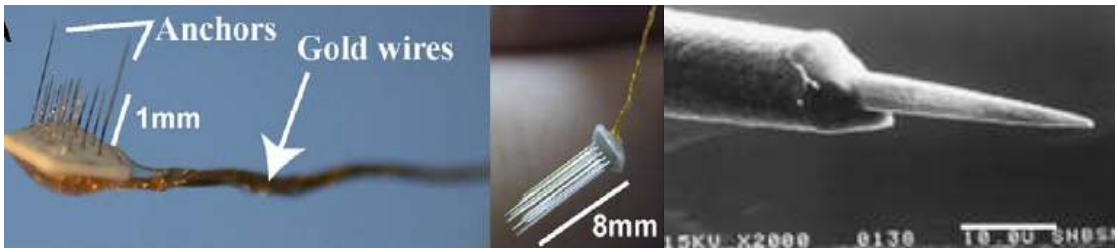

(a) **(b)**

Figure 1-3: (a) Floating multi-electrode array with short and long electrodes; (b) An SEM micrograph of an electrode used in the floating multi-electrode array (FMA) pretreated with A-174 Silane before being insulated with 3mμ of Parylene-C. The tip was exposed by a non-thermal ablation technique using a dual beam Eximer laser system. Taken from [43] and [63] respectively.

Although metal based electrodes are still employed successfully in both acute and chronic recording from the brain tissue, these kinds of electrodes can record activity only at their exposed tip. Increasing the number of recording sites requires increasing the number of electrodes which results in a linear increase in overall probe size and causes undesirable neural tissue damage. Further, it is difficult to insert a large number of probes accurately into a small volume of brain tissue. The main advantage of metal electrodes is the simplicity in their manufacturing. This simplicity also leads to its disadvantage which is the lack of common standards and automation in electrode manufacturing from one institution to other. Due to the lack of automation, the electrical characteristics of the recording tip vary from one microelectrode to the next within a batch, from batch to batch, and from one laboratory to other.

The micromachining of metal wire based neural probe arrays has been demonstrated using electroplating technique as it provides high aspect ratio structures for various metals. This process consists of fabricating multiple metal shafts on the same silicon substrate and then releasing them by back etching of the silicon. Insulation layer, consisting of Parylene-C as shown in Figure 1.4 [64] or silicon nitride [65], is applied and photolithographically patterned to expose the recording areas. Hiroaki Oka *et al.* [66] employed electroplating in developing a planar multielectrode array, known as the MED probe, to perform invitro electrophysiological studies on acute hippocampal slices. The array consists of 64 platinum black microelectrodes electroplated on a transparent Pyrex substrate. Layers of nickel and gold were nonelectrically plated to form bonding pads. Indium-tin oxide was selected for its transparency to form interconnects between the platinum electrode and the bonding pads. Finally, the array was insulated with polyimide except for the platinum electrodes and the bonding pads. Recently, electroplating was used to produce tapered shanks in a single plating step

[67-68]. The use of a patterned seed layer enables creation of 3-D structures with varying thickness and the process was first reported by Maciossek [69].

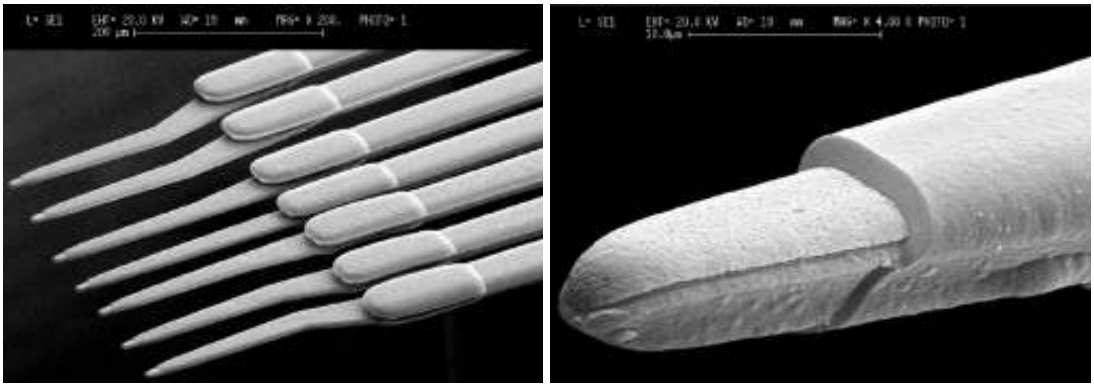

(a) **(b)**

Figure 1-4: SEM Micrographs of: (a) Seven array microelectrode tip regions; (b) The Parylene electrode in a Parylene window on the tip. Taken from [64].

The fabrication starts with patterning multiple regions of seed layer with all except one layer being electrically isolated from the electroplating. The electroplated nickel which was used in the process will grow upward and outward from the edges of the patterned seed layer and results in a structure with rounded edges both in- and out- of plane as shown in Figure 1.5.

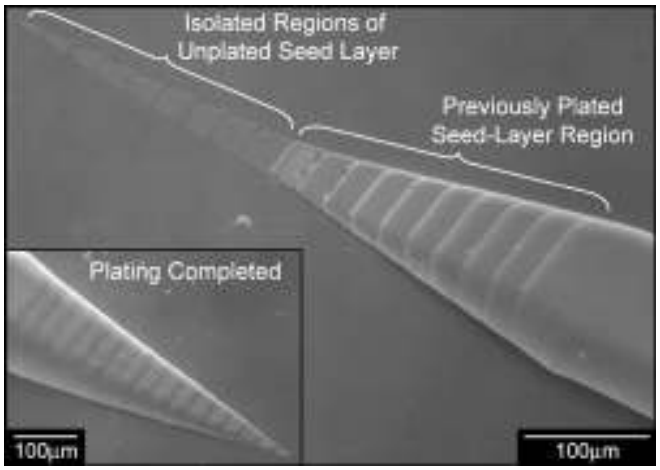

Figure 1-5: Electrodeposition of the mechanical layer in the probe shank. The SEM image shows the seed-layer regions that are not plated and those previously plated. The inset image on the low left shows the finished tip of the electroplated microprobe. Taken from [68].

During electrodeposition as the height of the electroplated metal equals the height of the neighboring electrically isolated region of the seed layer, plating will occur even on the insulated regions. The electroplating technique is mainly limited by anisotropic deposition rate due to the current crowding effect. Specifically, the electric field lines leave the cathode uniformly and crowd on the exposed metal regions on the wafer. The result is a higher deposition rate laterally than vertically. Moreover, wire-bonding cannot be used to connect the probes to external circuitry so wires have to be manually soldered to the probe bond pads. The silicon based probes discussed in the next section appear to be more attractive option than metal probes as each can carry many recording sites that are placed at relatively known positions on the probe. Thus, the increase in the number of the recording sites does not increase the overall probe size.

1.4 Silicon Based Neural Probes

Emerging from IC (Integrated Circuit) technologies, MEMS (Microelectromechanical Systems) is growing as a revolutionary technology that enables fabrication of mechanical elements, electronics, sensors, and actuators on common substrate. The advantages of MEMS technology include: suitability for high-volume and low-cost production; reduced size, mass, and power consumption; high functionality; improved reliability; novel solutions; and new applications. Because of its root in the IC industry, many of MEMS basic processing techniques are borrowed or adapted from IC technology, such as photolithography, oxidation, diffusion, ion implantation, chemical vapour deposition (CVD), evaporation, sputtering, wet chemical etching, and dry plasma etching. There are a number of features common in MEMS fabrication processes that are not as common in IC fabrication; these are: nonplanar substrate (i.e., relatively large 3-D features); the use of thick photoresist layers (for structure purposes or for long etching time); relatively high aspect ratio structures; relatively large feature sizes; unusual processing steps; and unusual materials (particularly important in terms of adhesion).

Silicon micromachining has been a key factor for the vast progress of MEMS. Silicon micromachining comprises two technologies: bulk micromachining, in which structures are etched into silicon substrate and surface micromachining, in which the micromechanical structures are formed from layers and films deposited on the silicon surface as depicted in Figure 1.6.

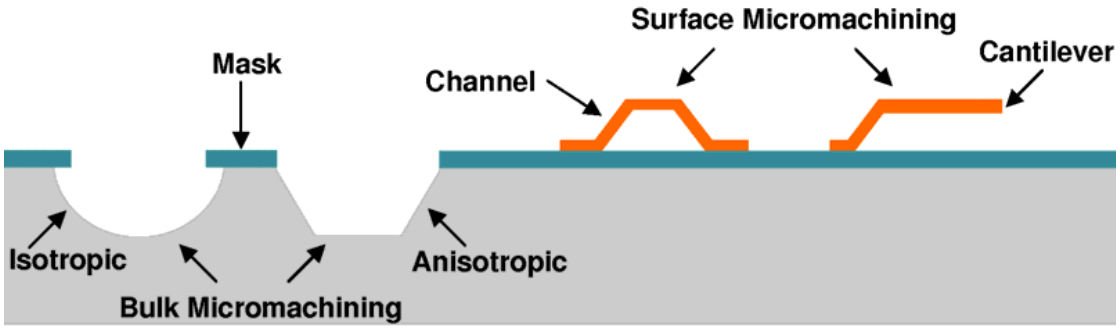

Figure 1-6: Illustration of bulk micromachining and surface micromachining. Taken from [59].

1.5 Bulk Micromachining

Bulk micromachining describes the fabrication process of a device taking advantage of all three space dimensions. In most applications single crystalline silicon is used as bulk material. Bulk micromachining defines structures by selectively etching inside a substrate. Isotropic wet etchant such as HNA (hydrofluoric acid + nitric acid + acetic acid), and anisotropic wet etchant such as solutions of KOH (potassium hydroxide), EDP (ethylene diamine pyrocatechol), TMAH (tetra-methyl-ammonium-hydroxide), and hydrazine-water are used. These anisotropic wet etchants have different etch rates in different crystal orientation of the silicon [70]. By combining anisotropic etching with boron implantation (P+ etch-stop) and electro-chemical etch-stop technique, varied silicon microstructures can be bulk machined.

Dry etching occurs through chemical or physical interaction between the ions in the gas and the atoms of the substrate. The non-plasma, isotropic dry etching is possible using XeF_2 (Xenon Difluoride) or a mixture of inter-halogen gases and provides very high selectivity for aluminum, silicon dioxide, silicon nitride, photoresist, etc. The

most common dry etching of bulk silicon is plasma etching and RIE (reactive ion etching), in which the external energy in the form of radio frequency (RF) power drives chemical reactions in low-pressure reaction chambers. A wide variety of chlorofluorocarbon gases, sulfur hexafluoride, bromine compounds and oxygen are commonly used as reactants. The anisotropic dry etching processes are widely used in MEMS because of the geometry flexibility and the less chemical contaminations as compared with wet etching. High aspect ratio microstructures can be obtained by deep reactive ion etching (DRIE) with "Bosch process", which is a room temperature process based on continuous cycling of passivation and etching steps.

1.6 Surface Micromachining

Unlike bulk micromachining, where a silicon substrate (wafer) is selectively etched to produce structures, surface micromachining is based on the deposition and etching of different structural layers on top of the substrate. Surface micromachining starts with a silicon wafer or other substrate and grows layers on top. These layers are selectively etched by photolithography and either a wet etch involving an acid or a dry etch involving an ionized gas or plasma. Surface micromachining requires a compatible set of structure materials, sacrificial materials, and chemical etchants. The structural materials must possess the physical and chemical properties that are suitable for the desired application. The sacrificial layers are used to make suspended structures. The sacrificial materials must have good properties to avoid device failure during fabrication. These properties include good adhesion and low-residual stresses to eliminate device failure by de-lamination and/or cracking. Common sacrificial materials are photoresist, polyimide, metals, phosphosilicate glass (PSG), and polysilicon.

The introduction of surface and bulk micromachining techniques played a significant role in standardizing the production of microprobes with very well defined shanks and precise placement of recording sites [71-72]. The high accuracy and repeatability inherent in these techniques have overcome the problems associated with manual

(non-automated) microelectrode fabrication. Moreover, batch processing can be utilized to mass-produce the microprobes at very low cost. Using silicon micromachining, one can obtain an active probe with on-probe signal processing circuitry and/or integrated micro actuators driving the electrode shank in order to track the neuron movement [73-80]. The fabrication of silicon based neural probes includes deposition of a metal layer on an insulated substrate and patterning the metal layer to form recording sites, read-out pads for connecting to external circuitry, and interconnecting traces between the recording sites and read-out pads. An insulating layer is then deposited over the whole structure and patterned to open access above the recording sites and bonding pads.

The substrate forms an important part of the probe structure providing the mechanical support. Ideally, the substrate must be biocompatible, small enough to obviate damage to the tissue and strong enough to penetrate the *pia arachnoid* membrane covering the brain. Silicon has well-recognized mechanical advantages suitable for neural probes and it allows the use of the well-established microfabrication technologies and equipment infrastructure developed for the integrated circuits industry leading to high precision and well-defined structural features. The use of silicon photolithography process allow excellent control over the recording site size, shape and spacing enabling multiple recording sites to be placed at variable heights on a single electrode shank. Such ability allows insertion of a large number of recording sites in a small volume which is not possible with metal wire arrays or bundles. Inclusion of integrated circuits can be performed directly on the probes and offers benefits in terms of better signal acquisition, reducing power line interference, and ultimately reducing the overall probe size by reducing the electrical cable sizes [74-84].

A well-known example of silicon based neural probes is the Michigan probes [85] and an example of which is shown in Figure 1.7. The research groups led by Wise and Najafi have developed a variety of neural electrodes including single-shaft, multi-shaft, and 3-D-stacked layouts [12, 44, 71, 74-92]. In addition, many of the developed electrodes are integrated with microelectronic circuitry for signal processing. The fabrication process for these probes typically involved anisotropic etching with

ethylene diamine pyrocatechol (EDP) and using a boron-etch-stop. The process is based on the fact that the etch rate for p-type silicon is much slower than for un-doped silicon. Boron diffusion is first performed on silicon to define the shaft shape in the substrate and followed by EDP wet etching to release the probe shafts by having a rounded cross-section and a rounded sharpened tip. Gold, platinum, or iridium metal is used for recording sites. The insulation on top of silicon substrate is made with triple layers of silicon dioxide, silicon nitride, and silicon dioxide. Finally, the interconnection is made with a 4–5 μm thick polysilicon cables which are reported as weak cables and easy to break leading to lower yield for long lengths because of the high aspect ratio and lack of robustness [85, 92-93].

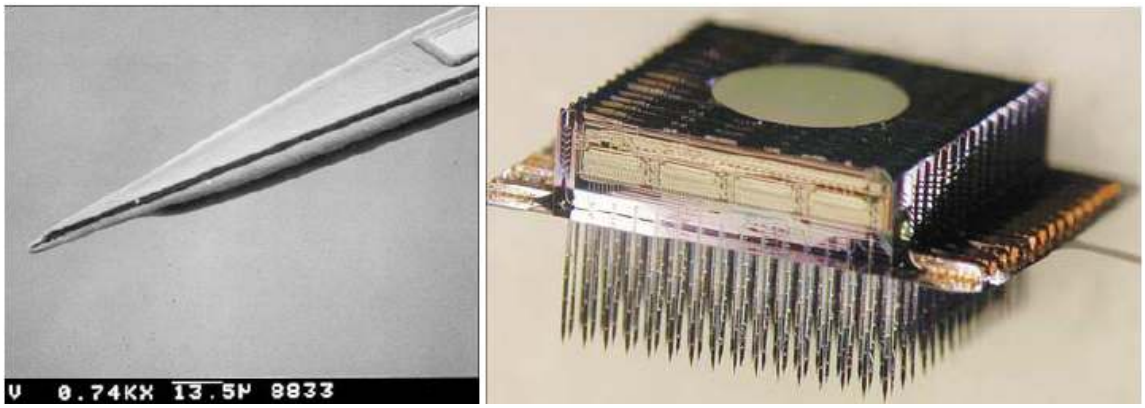

(a) **(b)**

Figure 1-7: (a) Scanning electron microscopy side view of a silicon probe substrate defined using a shallow (tip) and deep (shank) boron etch-step (above) and perspective view (below); (b) Photo of a 3-D 1024-site 128-channel neuroelectronic interface. Taken from [85].

Michigan probes have been successfully used in a number of neuroscience applications, but they also suffer from some disadvantages related to probe thickness and durability. Typically, wet etching can be employed for limited probe thickness and thus we find that the typical thickness of the Michigan probes is 15μm. These probes when pierced through the *pia* layer of the brain needed special guide tools for insertion. Mechanical weakness of the probes causes the probes to crack and shatter and may cause severe damage and disturbance to the brain tissue during insertion. Another well-known silicon based-probes incorporating multiple-electrode arrays is

the Utah probe and an example of which is shown in Figure 1.8 [94-101]. The Utah electrode arrays are typically made from 1.83mm thick boron doped silicon substrates (resistivity of 0.01 Ω-cm). A diamond dicing saw is used to create a grid pattern of 300μm deep grooves on the surface of the substrate. A sealing glass is deposited on the grid to create insulation between the electrode bases. Electrode columns are made by sawing a grid on the other side of the silicon and separated by the insulating glass layer. Acid etching smoothes the pillars and creates sharpened probe tips which are then coated with metal for recording and stimulation. Gold, platinum, and iridium are the commonly used metals for the recording purpose. Polyimide is used to coat the probes as the insulation layer with only the recording sites exposed.

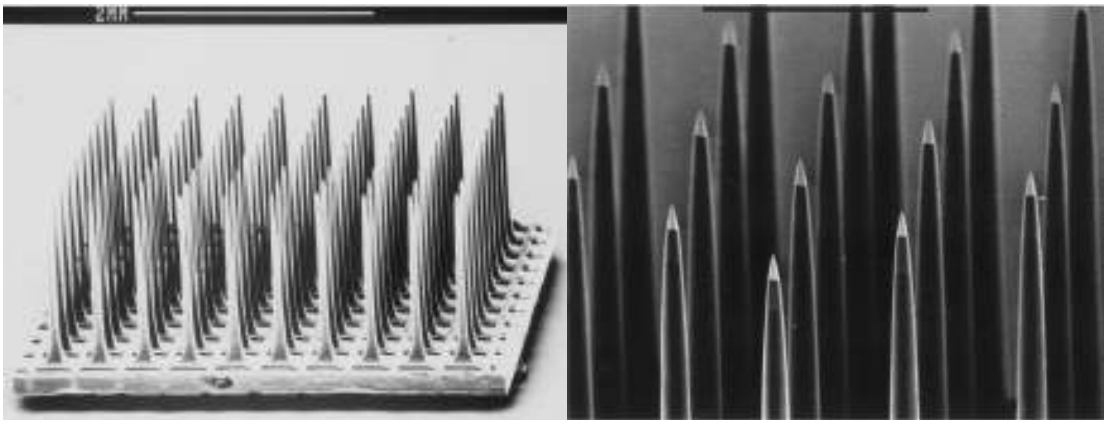

(a) **(b)**

Figure 1-8: SEM micrograph of: (a) The Utah array; (b) The insulation coated electrodes with exposed platinum tips. Taken from [101].

The Utah electrode arrays have a unique structure with the arrays pointing upwards (vertically oriented) as opposed to all other silicon neural probes which are built lying down (horizontally oriented). As a result, the probe length of the Utah electrode arrays is limited by the silicon wafer thickness. The longest reported probe length is only 1.5 mm. Further, only one recording site can be made on each probe shaft and the fabrication process is not a typical batch process and therefore suffers from low production rates. The interconnection of the Utah electrode arrays is made of a set of polyimide insulated gold wires and ultrasonically bonded on the back of the array to a set of aluminum read-out pads. The stiffness of the metal wire bundle makes these

unsuitable for chronic implantation in human brain and especially for the high-density electrode arrays.

1.7 Silicon on Insulator (SOI) Based Neural Probes

SOI wafers are produced by placing a thin, insulating layer such as silicon oxide (SiO2) or glass sandwiched between a thin layer of silicon (device layer) and the silicon substrate (handle wafer). SOI based neural probes employ the SiO_2 layer as an etch-stop layer. Several etching techniques are available where the etch rates for SiO_2 are much lower than for silicon. The handle wafer is back etched to release the probe shaft which means that the probe shaft thickness is defined by the thickness of the device layer. Different techniques have been used to develop neural probes using SOI wafers, starting with the use of backside wet-etching using potassium hydroxide (KOH) [102] solutions. Plasma etching technology for silicon was also employed which led to the establishment of new fabrication processes to develop neural probes. Plasma etching is a physical-chemical dry etching technique which offers several advantages over traditional wet etching including more reliability and yields a smoother and cleaner etched surface. The plasma etching also has other advantages including relative insensitivity of the etch rate for silicon to its electrical conductivity, less corrosion problems for metal features in the recording sites, and less undercutting and broadening of the photoresist features. Therefore, the use of SOI wafers combined with plasma etching technique provides a good control over the final probe thickness compared to using wet etching with a boron etch-stop. The SOI neural probes are made using CMOS-compatible batch process with multiple electrode sites on each probe shaft. Probes with different thicknesses can also be made by choosing SOI wafers with different device layer thicknesses [102-103].

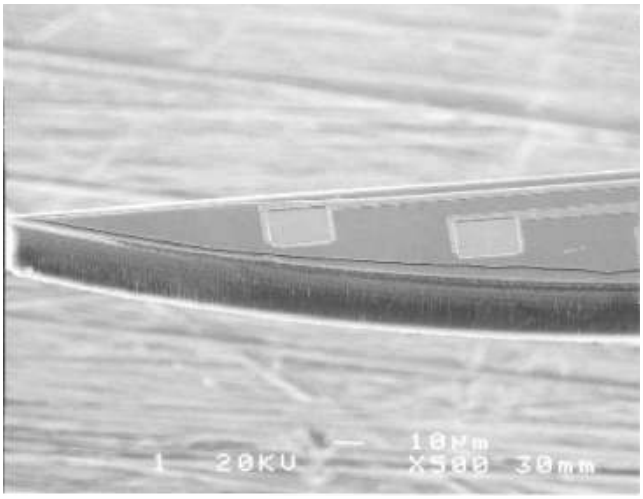

Figure 1-9: Electrodes at the tip of each probe are separated by 45 µm spacing. Each electrode is 20µm x 20µm square. Taken from [84].

A combination of plasma etching (to shape the probe shafts) with KOH wet etching of the handle wafer (to release the shafts) was used by Kewley *et al.* [104]. Another combination of SOI wet etching, to embed microchannel in the device layer, and plasma dry etching to release the probe shaft was also reported [84]. An improved technology to fabricate silicon neural probes using the Deep Reactive Ion Etching (DRIE) in SOI wafer to overcome the use of wet etching and boron etch stop was developed by Cheung *et al.* and these fabricated probes are shown in Figure 1.9 [84, 105]. Also, Norlin *et al.* used double-sided DRIE of a SOI substrate with the buried SiO2 layer acting as an etch stop to pattern forklike probe shafts as shown in Figure 1.10 [103].

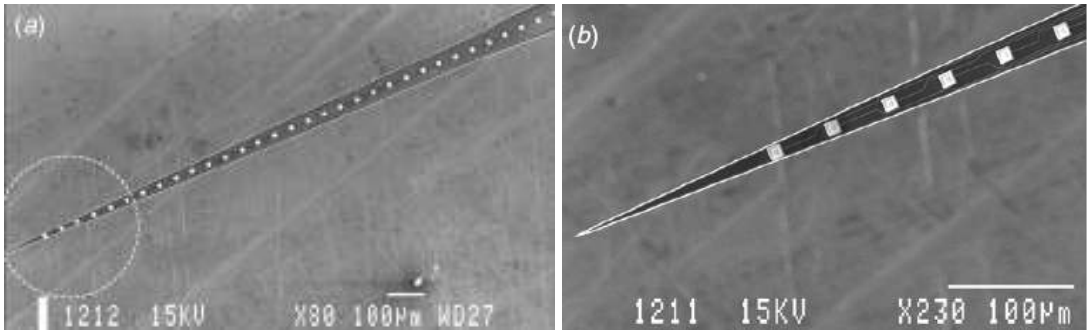

(a) **(b)**

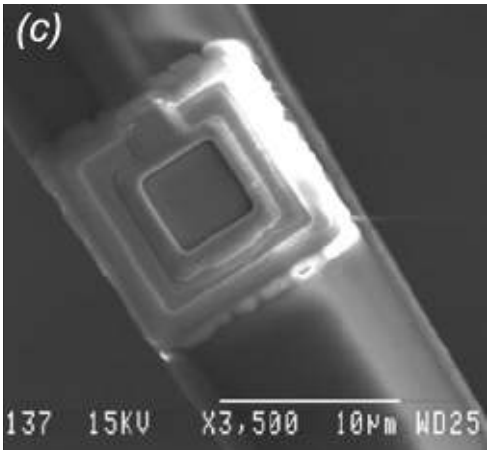

(c)

Figure 1-10: Scanning electron micrograph of (a) A silicon probe with 1 shaft x 32 electrodes; (b) Close-up of a probe tip designed with 4^{o} taper angle. The interconnect lines shown are 1µm wide; (c) Close-up of a 10 µm x 10 µm Ir electrode site. Taken from [103].

More recently, Kindlundh *et al.* used DRIE in combination with direct write laser lithography (DWL) for neural probe fabrication [106]. DWL is used to replace the photolithography technique with fixed lithographic mask sets and the process is relatively straightforward but is suitable mostly for small production volumes. The fabricated sample is shown in Figure 1.11.

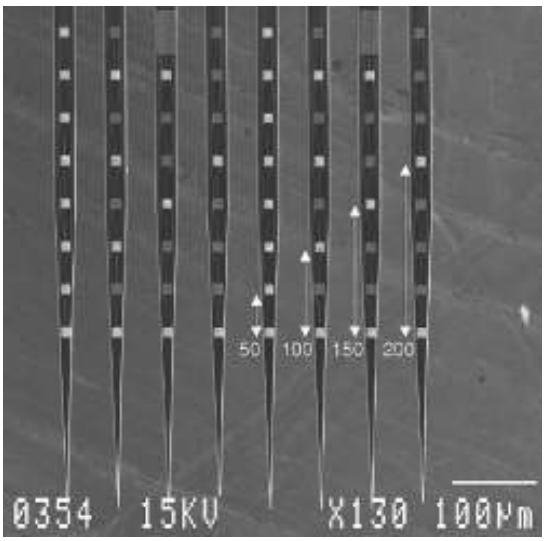

Figure 1-11: Scanning electron micrograph showing selectively opened electrode windows in the Si3N4 layer on a 64-site probe. Bright squares are opened windows. Distances shown are in micrometers. Taken from [106].

1.8 Polymer Based Neural Probes

The use of polymer materials for neural probes has been widely studied to replace the normal silicon nitride or silicon dioxide insulation layer deposited during the fabrication of silicon neural electrodes [64, 107-109]. Different biocompatible polymers such as polyimide [107] and Parylene-C are used to cover the metal and silicon region of the probes to form a biocompatible interface between the probe and the brain tissue. For example, polyimide was used to coat the Utah electrodes arrays [94-95]. Parylene-C was used as insulating layer on silicon probes [64]. More recently, polymers on metal probes was used wherein each probe encompasses a single recording site and a dual beam Eximer Laser system process was used to open the probe recording tips [43]. Polymer materials are also used for the interconnect cables. For example, microfabricated polyimide cables [110] and PDMS cables [111] are reported as interconnections for the silicon neural probes. However, unconventional bonding methods are still required to connect the polymer cables with the microfabricated silicon probes.

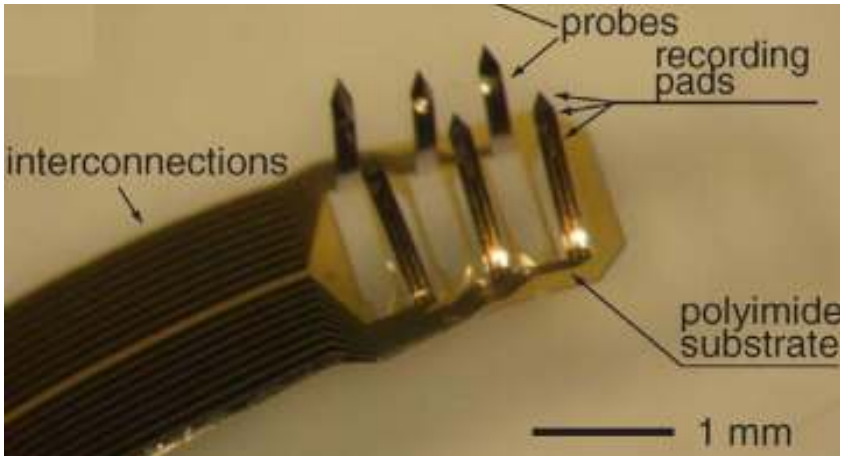

Figure 1-12: 3D flexible probe array after folding. The recording pads are vertically aligned. [112].

Rousche *et al.* [51] demonstrated a flexible polyimide neural probe wherein a gold metal layer was used for the recording sites. The interconnection traces and read-out pads are sandwiched between two polyimide layers. Similar devices were also

reported by Shoji Takeuchi *et al.* [112] as shown in Figure 1.12. 3-D probes can be formed by physically bending the polyimide shanks out of the 2-D plane. The use of polyimide improves the malleability match between a rigid electrode and soft tissue and the lack of which results in tissue damage if the electrode moves relative to brain. A major drawback to this design is that the electrodes are not stiff enough to pierce brain tissue on their own, so implant sites had to be created with metal wire or a scalpel before insertion. An improved polyimide probe was reported by Lee *et al.* [113] and is shown in Figure 1.13, where a 5-10μm thin silicon support layer formed from silicon-on insulator (SOI) substrate is attached to the desired region of the probe shaft to increase the stiffness. The stiffness of the electrode can be varied by changing the thickness of the silicon backbone layer. A similar polyimide probe with 15μm molybdenum backbone was developed by Blum *et al.* [114].

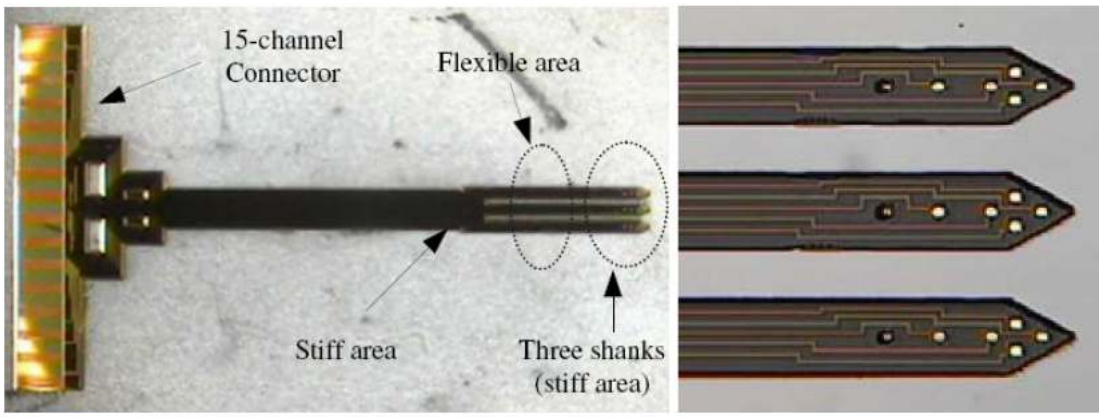

(a) **(b)**

Figure 1-13: Optical microscope images of the polyimide neural probes (a) View of the electrode; (b) Top view of the three shanks. Taken from [113].

The flexible polyimide electrodes suffer from disadvantages due to the lack of rigidity which causes buckling during insertion into the brain. Given this reason, long length polyimide probes cannot be used as they bend due to lack of rigidity and reduces the accuracy in targeting a selected region in the brain. Moreover, polyimide-based probes are prone to failure due to possible moisture absorption by polyimide. Given this, silicon-based neural probes appear to be more successful owing to the mechanical

properties of the silicon and the flexibility of patterning using standard microfabrication technologies.

1.9 Applications of Neural Probes for Neural Prosthesis

A neural prosthesis is a direct brain interface that enables a primate, via the use of surgically implanted electrode arrays and associated computer algorithms, to control external electromechanical devices by pure thought alone. The first beneficiaries of such technology are likely to be patients with spinal cord damage, peripheral nerve disease, or ALS (amyotrophic lateral sclerosis, also known as Lou Gehrig's disease). In the United States alone, there are 2.28 million patients with some form of paralysis. A primary issue in neuroprosthetic research is the choice of brain area from which prosthetic command signals are derived. Current studies around the world have focused primarily on deriving neuroprosthetic command signals from the motor cortex [115-118]. Recordings from multiple neurons are "decoded" to control the trajectories of a robotic limb or a cursor on a computer screen. In addition, progress has been made in using electroencephalogram (EEG)-based signals to derive neuroprosthetic commands.

At McGill, we have pursued an alternative and novel approach, which is to use high-level cognitive signals for controlling neural prostheses (Figure 1.14) [119-121]. Read-outs are made of the goals and intentions of the subject, rather than the instructions on how to obtain those goals. Smart output devices-such as robots, computers, or vehicles-using supervisory control systems, then manage carrying out the physical tasks required to complete the intended goal. The cognitive signals that can be read-out are complex and can include the expected value of an action and, perhaps in the future, speech, emotional state, and other higher cortical functions as well. An "expected value signal" is used by the brain to make decisions and can be used by prosthetics to interpret a subject's decisions, preferences, and motivation, all of which would help a paralyzed patient communicate better with the outside world.

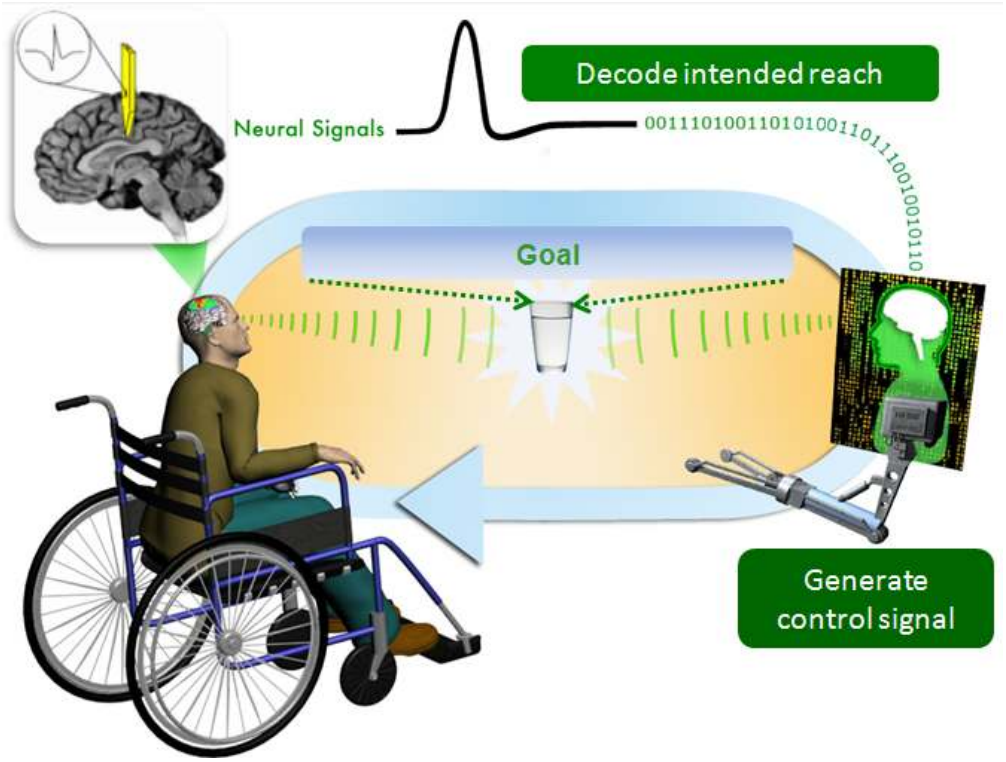

Figure 1-14: Schematic of the pathway of information flow for the cognitive-based neural prosthetic paradigm.

1.10 Biocompatibility of Neural Probes

Perhaps the greatest challenge facing the use of neural implants is the resultant tissue response to the neural injury which effects the long term functioning of the implanted neural probe. Signal deterioration soon after implantation of arrays has been reported by many groups. For these devices to be useful, they should ideally remain functional indefinitely for enabling self-contained and self governing brain machine interfaces. Signal deterioration has been attributed to the general immune activation of the brain in response to the presence of a foreign device. Insertion of the electrode ruptures the vasculature and destroys all neurons in its path. Immediately following the insertion of an array, an acute immune response is activated which facilitates the recruitment of glial cells [122]. Activated glial cells will commence digesting the cellular debris with enzymes. The extent of the response is a function of probe size [122], probe shape [123] and surface texture [124]. This initial response gives way to the chronic

response where scarring in the brain leads to the beginning of probe encapsulation [122].

Using immunohistology, Biran *et al.* [125] showed that the glial density around implanted probes increases with time, further isolating the electrodes from neurons. Further damage is elicited by the motion of the electrode within the brain [126]. The brain experiences micromotion in response to physiological processes such as cardiac rhythms [127] and head movements [128]. This motion may cause the electrodes to rip the neural tissue as the stiffness of the brain and the electrodes differ. Formation of the glial scar needs to be minimized in order to extend the lifetime of the arrays. Two strategies that are currently being investigated include methods to minimize the immune response or the addition of proteins to encourage neural growth. Injection of dexamethasone postoperatively to attenuate inflammation has been shown to decrease the initial and long term response [129]. Local delivery of dexamethasone at the site of injury may prove to be a more effective method since delivery can be sustained indefinitely [130]. Anti-inflammatory agents have been used to coat the electrode [131]. This method has also been shown to be effective in reducing glial response.

In contrast to directly battling the immune response, some groups have proposed using neural growth factors to encourage neural growth around the electrode. Kennedy used a glass cone filled with growth factor releasing tissue and showed that using neural growth factors (NGF) improves recording over many months [132]. In addition, Moxon *et al.* recently showed that using nanostructured porous silicon (PSi) surface for implants improved biocompatibility [133]. They reported decreased astrocyte adhesion on nanoporous silicon without any interference in the electrode's ability to record the action potentials [109, 134-136]. We believe the use of porous silicon as the biocompatible layer offers grest promise and is also investigated in the current Thesis.

1.11 Summary

This chapter is based on the review paper published by our group entitled "NeuroMEMS: Neural Probe Microtechnologies" Sensors, vol. 8, pp. 6704-6726, 2008. The Chapter aimed to give an overview of the commonly used microfabrication technologies to develop neural probes for prosthesis and brain machine interfaces. Technological advancements in the areas of microelectronics along with surface and bulk micromachining have led to the development of a great number of passive and active probes. We described metal wire, silicon, and polymer based neural electrodes. Silicon based probes appear to be the most versatile and widely accepted technology for neural microelectrodes. We notice that there are three main considerations for the development of neural electrodes, namely, (i) probe material selection, (ii) microfabrication process, and (iii) biocompatibility interface. The combination of these three factors ultimately determines the functionality, usability, and long-term implantation reliability of the neural electrodes.

Implantable neural probes are generally preferred to have a minimum footprint as possible to minimize neural damage and to facilitate easy entry and movement through the brain tissue. The above requirement combined with the growing interest to undertake neuroscience studies from deeper regions of the brain has necessitated the need to develop ultra-long probes (lengths longer than 5mm) with thicknesses less than 50μm. Such high aspect ratio structures pose a great design challenge as the probes have to be able to withstand the insertion axial forces, retraction forces, and tension forces of the brain tissue. New techniques such as probe reinforcement as described in the next chapter have to be developed for these emerging applications. Also, the production of neural probes with standard commercial MEMS process is described. Using MEMS commercial process could lead to the development of new neural probes that are cost-effective and mass-produced with ultra-long probe shafts and on-site/on-probe signal processing circuitry.

1.12 Dissertation Goals and Organization

The goal of the work presented in this dissertation is to develop a novel elongated multi-modal reinforced implantable neural microelectrode arrays capable of simultaneously monitoring neuronal electrical action potentials and brain tissue oxygenation. We hypothesize that these multiple multi-modal signals will increase the amount of information we can decode and open up new avenues for novel theories of brain function.

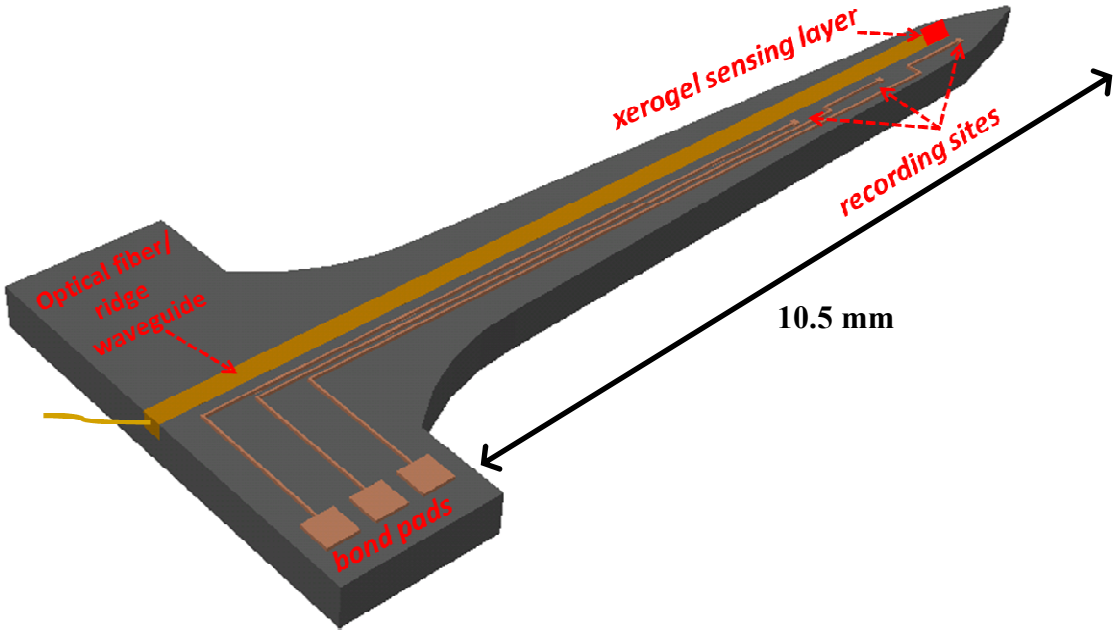

Figure 1-15: Design of the multimodal neural microelectrode combining neural electrical activity recording and optical sensor waveguiding structures.

Aiming for an elongated, reliable, multiple measurand, and biocompatible neural probe, different aspects of the proposed multimodal neural probe were investigated and researched in this thesis. Specifically, the concept of reinforcing neural microelectrodes, the development of optical biochemical waveguide sensors, the integration of the optical sensors with electrical sensors on the same probe electrode, and the biocompatible interfacing of these probes with brain neural tissues represent the core of the subsequent chapters of this thesis:

Chapter 2 presents a novel concept of reinforcing elongated silicon microelectrode arrays and describes the fabrication of these electrodes using standard commercial technology and a custom established fabrication process. The Chapter provides a detailed description describing the analytical and numerical models and the experimental mechanical testing results that depict the effect of the reinforcement in making the neural probes sturdier.

Chapter 3 focuses on the development of polymeric waveguide support platform for optical biochemical sensors. The Chapter describes the development of sol-gel derived xerogel based sensing or recognition elements by encapsulating the fluorophores or various biomolecules in their porous nano/microstructured matrices. Specifically, it demonstrates a ridge waveguide structure made with direct-dispense to support sol-gel derived xerogel recognition materials which are made responsive to oxygen concentration. The direct-dispense system is exploited toward miniaturization and hybrid integration of the optical sensors with the silicon neural electrodes as described in Chapter 4. For this purpose, a modified recipe of the xerogel sensor materials was employed to make these materials suitable for direct-dispense process.

Chapter 4 concentrates on the integration of optical biochemical sensors with neural microelectrodes. The Chapter describes the fabrication process of a tapered silicon electrode incorporating an etched rectangular cavity serving as recessed surface to embed the optical biochemical sensors. Given the difficulties and complications encountered in the setup of the ridge waveguide optical sensor implementation, an optical fiber was prepared, coated with optical biochemical sensors, and integrated with the neural electrode to monitor brain tissue oxygenation. Here, a more sensitive recipe of xerogel sensors is employed. The functionality of this multi-modal electrode investigated through in vivo experimentation in non-human primate (monkey) is also discussed in this chapter.

Chapter 5 is meant to introduce a novel technique to make the neural probes biocompatible and thus reducing the tissue response to the neural injury which effects

the long term functioning of the implanted neural probe. In this chapter, the use of xenon difluoride dry etching technique to form porous silicon surfaces, known as biocompatible material, is described in detail. In vitro study, consisting of plating mesenchymal stem cell derived from bone marrow of Pthrp mice on porous silicon platform. This is to demonstrate the biocompatible characteristic of porous silicon by its ability to promote stable environment for growth and proliferation of mesenchymal stem cell (MSC).

Finally, Chapter 6 provides a summary of this dissertation and concludes with some insights into future developments of these sensor systems

CHAPTER 2

REINFORCEMENT OF NEURAL PROBES

The interfacing and interpretation of human neural systems at peripheral, spinal, and supra-spinal levels, which requires the recording of the electrical activity generated by nerve cells, has been one of the core activities of neuroscience for many years [6, 10, 60]. The recording and processing of neural signals is required to understand how the brain processes information in response to controlling body functions. Such information could lead to successful development of closed-loop neural prostheses which can assist paralyzed patients by allowing them to operate computers or robots with their neural activity. Theses prostheses typically employ microelectrodes implanted in different areas of the brain or assembled into an array that can sample a larger portion of a single area to map the brain function and dynamics of complex networks of neurons [19-20]. Therefore, multi-recording site microelectrode arrays have become a key component of neural prosthesis development as they represent the machine to interface with the brain [6, 8]. Given the rapid advancements in silicon micromachining technologies, there is a great interest to develop silicon based neural microelectrodes with well defined electrodes and precise placement of multiple recording sites on each electrode [44, 46-47, 71]. Further, there is a need for improving the mass-production and cost-effectiveness of these technologies to increase their accessibility to large patient populations.

Cognitive control signals for neural prosthetics is a relatively new concept that deals with monitoring and understanding the messages of higher-order neurons involved in planning and motivation for movements such as reaching and grasping [119, 121]. These signals can be located in the posterior parietal reach region (PRR) located medial to the intraparietal sulcus and the dorsal premotor cortex. These regions are located much deeper in the brain compared to the motor cortex which provides the actual control signals for movements. PRR lies within a broader area of the posterior

parietal cortex (PPC). PPC is located functionally at a transition between sensory and motor areas and is involved in transforming sensory inputs into plans for action or so-called sensory–motor integration.

Many of the current available silicon microelectrodes cannot be effectively used to gather information from the deeper regions of the PRR because of their shorter lengths. Well known examples of such microelectrodes include the Utah and Michigan arrays. The Utah electrode arrays are built vertically pointing up, as opposed to all other silicon neural probes which are built lying down. Consequently, the electrode length is limited by the thickness of the silicon wafer and typical probe lengths are only 1.5mm [94]. In addition, only one electrode site can be made on every probe. The Michigan array electrodes are made of boron doped silicon substrates and most reported electrodes reach a lengths of 3mm long [81, 137]. More recently, Norlin et al. [103] have demonstrated 5mm long electrodes using Deep Reactive-Ion-Etching (DRIE) of Silicon-on-Insulator substrates. The probe length is considered as one of the key requirements for the acquisition of the cognitive signals located at deeper regions in the brain. These regions are typically located deeper than 6mm from the surface of the brain tissue in non-human mammals like monkeys and humans [138]. Considering the length requirement, the probes also need to be supported to withstand the insertion axial forces, retraction forces, and tension forces of the brain tissue during implantation without increasing the footprint of the electrode array. In this chapter, we propose the concept of reinforcing the regions of elongated microelectrodes that are more susceptible to breakage. We show that reinforcing specific regions of the probe with metallic layers pushes the region of maximum stress from the center to the base region of the probe which is typically sturdier. The reinforced probes are fabricated using both custom process using McGill clean-room facilities and the commercial MicraGem process from Micralyne, Inc.

The availability of silicon (for use as the substrate material) and gold (for use as recording site material) in the standard MicraGem process from Micralyne Inc. encouraged us to employ it for the fabrication of the described electrode array. The

electrodes are 6.5 mm long. The use of a commercial MEMS fabrication process for silicon neural microelectrodes development yields low-cost, mass-producible, and well-defined electrode structures. The limited allocated space for designs fabricated using standard MEMS fabrication process encouraged us to develop longer silicon electrodes at McGill Nanotools Microfabrication laboratory. The developed electrodes are 10.5mm long and 50µm thick.

2.1 Probe Design and Characteristics

A major criteria related to the neural microelectrode design is to have a minimum footprint as possible to minimize damage to the brain tissue and neuron networks. Typically, probe thicknesses less than 50µm for silicon based probes are preferred. The need for ultra-long electrode structures with lengths longer than 6mm to gather cognitive neural information adds further complications in the design and fabrication of the microelectrodes. These electrodes should have the ability to survive the different types of forces during the insertion and retraction phases of the surgical implantation. In this chapter, we introduce the novel concept of reinforcing the electrodes at their most susceptible regions for breakage to increase their durability. We designed probe structures with tapered chisel-shaped ends to facilitate easy entry into the brain tissue. The Micragem probe array consists of five electrodes varying from 2.5mm to 6.5mm in length while McGill array consists of four ultra-long electrodes having the same length of 10.5mm. Both arrays are constructed from silicon with gold as the recording site material. Figure 2.1 shows the design of the proposed arrays. Each electrode is divided into three regions (i) support base region (ii) measuring region and (iii) piercing region. The support base region measures 250µm in length with a width of 350µm at the base that rapidly reduces to width of 150µm thus minimizing tissue damage and displacement while providing sturdy support at the base of the probe. The measuring region starts with a width of 150µm at the base and ends up with 50µm at the other end. The electrodes have an average width of 100µm over majority of the length of the measuring region. The measuring region has 10µmx10µm metallic (gold) recording sites. The measuring region is

followed by the piercing region that forms the chisel-shaped tip of the probe with a length of 250µm and is designed to be 10µm width at the end of the probe which is the minimum feature size allowed by the Micragem technology. Thus, the final taper angle is 11^{o} which is same for the different electrodes. The tip of the McGill array is 5 micron wide.

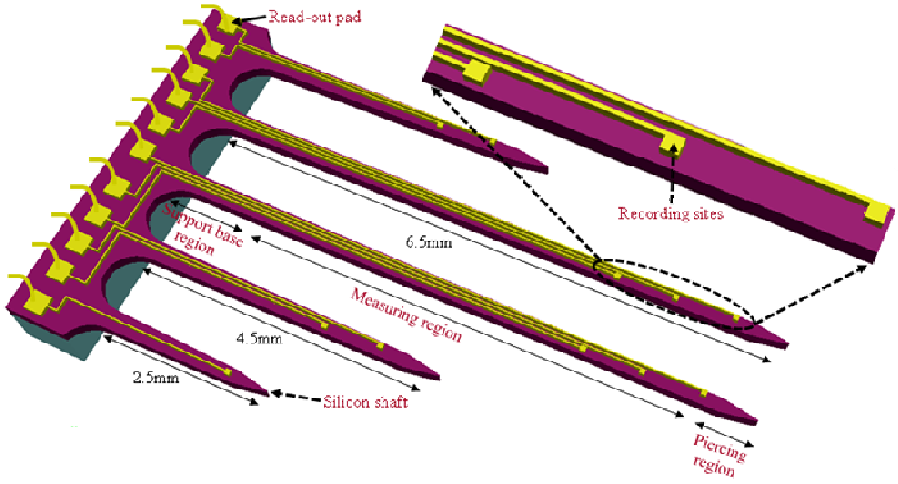

(a)

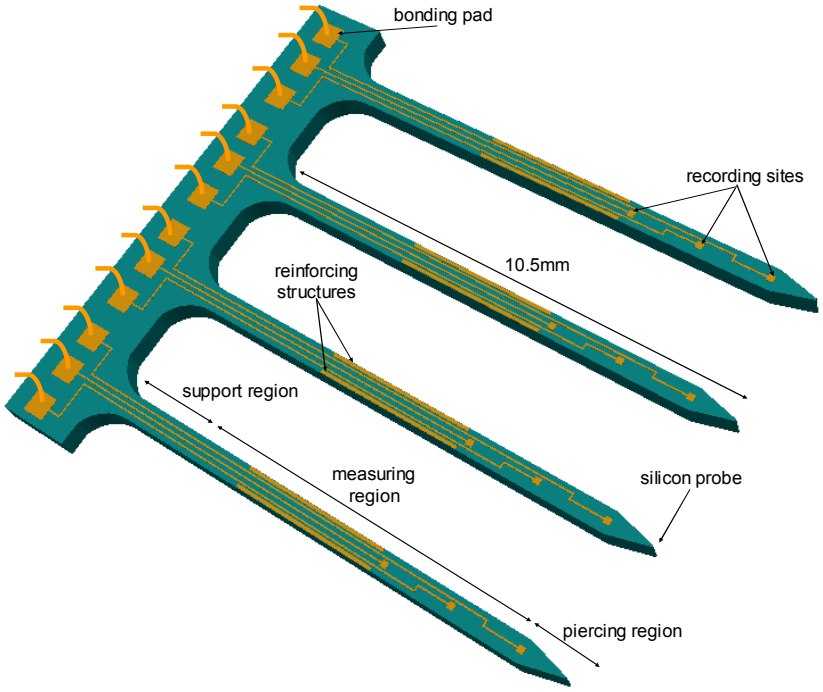

(b)

Figure 2-1: Design of the two developed neural microelectrode array showing the recording sites, interconnects, and bond pads a) MicraGem array; b) McGill array. The figure is not to scale.

The brain is covered by the *dura mater* and the *pia mater* layers as shown in Figure 2.2. During surgical implantation of the microelectrodes, the *dura* which is a dense fibrous tissue is removed. The microelectrodes are expected to pierce through the *pia* which is a thin delicate membrane typically one cell layer thick. This layer cannot be removed for implantation due to various neurophysiological factors and many microelectrodes crack or shatter at the *pia* .

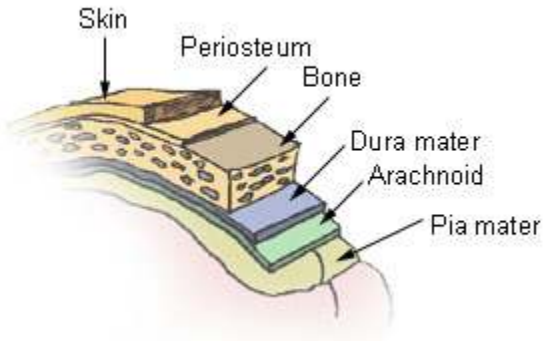

Figure 2-2: Meninges of the central nervous system. Taken from [139].

The presence of sharp tips at the end of the probe (such as less than 5μm) increases the possibility of shattering. The designed microelectrode array measures 10μm at the reinforced tip of each probe to increase the piercing strength. In the next Section of this Chapter, we describe the analytical analysis used to study and understand the mechanical behavior of the probe when it is subjected to different types of forces during insertion into the brain and ultimately understand the factors that would aid in the development of reliable, functional, and elongated neural microelectrodes.

2.2 Analytical Modeling of Neural Probe Mechanics

The main forces that act upon the electrode probe during handling and insertion into the brain tissue are (i) the bending force, as illustrated in Figure 2.3(b), which occurs under an out-of-plane loading causing parallel displacement to the tissue plane and (ii) the buckling force, as illustrated in Figure 2.3(c), which occurs under axial compression and mainly represented by the force which counteracts the normal force

exerted on the brain tissue by the probe and the shear force which prevents the tip of the probe from slipping on the surface of the brain tissue.

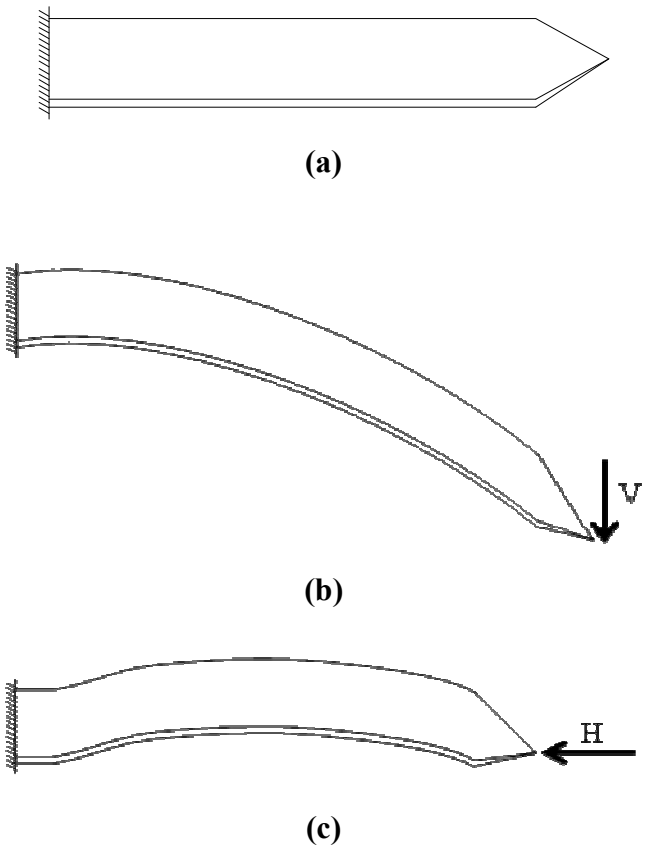

(a)

(b)

(c)

Figure 2-3: Illustration of neural probe deflections during the insertion phase (a) without deflection; (b) bending; (c) buckling.

Knowing the maximum bending force is important as it determines the maximum out-of-plane force at which breakage of the probes can occur. A case in which this transverse bending occurs is when moving the base region of the probe after its tip region is inserted into the brain tissue. Once a bending force is applied to the tip region, the electrode deflects in a quarter-circle way, as depicted in Figure 2.3(b), causing a maximum (above normal) stress at the fixed bottom of the probe connected to the base holding the bonding pad and an average (normal) stress at the middle region of the probe. These stresses are given by Equations (1) and (2) [140].

$$\sigma_{\max} = \frac{3Et\delta}{2L^2} \quad (1)$$

$$\sigma_{Avg} = \frac{3Et\delta}{4L^2} \quad (2)$$

where, L is the probe length, t is the thickness, E is the Young's modulus of silicon, and δ is the maximum deflection at the probe tip. The maximum bending force, which the probe can withstand at the tip region without breaking is derived from the basic differential equation for the deflection curve of a suspended beam fixed at one end and free to move at the other end [141] and it is given by Equation (3).

$$P_{\max} = \frac{\sigma_{\max} W t^2}{6L} \quad (3)$$

where, W is the width of the probe at the base and σ_{max} is the maximum stress of the electrode. The maximum bending force, P_{max}, is still valid to be applied for both uniform cross-sectioned and gradually tapered cantilevers as in both cases P_{max} depends only on the length and the cross-section dimensions at the base. The bending stiffness, however, depends on the shape of the cross-section throughout the tapered probe and can be expressed by a spring constant, K, which relates the lateral deflection of the tip, δ, relative to the transverse load, P, applied at the tip of the probe. The value for the spring constant, K, can be derived from the classical beam equation for the case in which the area moment of inertia, $I(x)$, of the cross-section varies linearly along the probe length as given by Equation (4).

$$EI(x)\left(\frac{d^2y}{dx^2}\right) = M(x) \quad (4)$$

where the bending moment is given by:

$$M(x) = P(x-a) \quad (5)$$

And

$$I(x) = IR(\frac{x}{a}) \qquad (6)$$

where R is the ratio of the width at the tip and the width at the base, and I is the moment of inertia at the base.

$$I = \frac{Wt^3}{12} \qquad (7)$$

Hence, the spring constant is given by Equation (8) [142]:

$$K = \frac{P}{\delta} = \frac{EW}{4}\left(\frac{t}{L}\right)^3 \left[\frac{\left(\frac{2}{3}\right)(1-R)^3}{(1-R)^2 - 2R(1-R) - 2R^2 \ln R} \right] \qquad (8)$$

In Equation 8, the expression before the square brackets is the spring constant for a probe with uniform cross-section throughout the length of the probe from the base to the tip. The expression within the square brackets represents the reduction in stiffness due to the tapering width.

The second type of force acting on the probe is the buckling force which occurs under axial compression. The buckling load is a critical parameter as it determines the force at which the probe tip penetrates the brain tissue. For the case of insertion of the probe in brain tissue, the applied force is assumed to be axial and the electrode probes are modeled as rigidly supported on one end (base region) and free to rotate at the other end (tip region). The axially loaded tapered probe loses its initial stable shape when it is subjected to an external force, P, greater than critical load, P_{cr}, required to buckle the single probe. For a probe with constant cross-section, the governing differential equation of an axially loaded probe along the longitudinal axis, (x), is given by Equation (9).

$$\frac{d^2\delta(x)}{dx^2} + \frac{P_b}{EI}\delta(x) = 0 \qquad (9)$$

where, δ is the transversal displacement; EI represents the flexural rigidity of the probe. The maximum load (force) required to buckle the probe (i.e.. Buckling or Euler‘s load) is obtained by solving Equation (9) for a probe with constant cross-section [143] throughout the length of the probe and it is given by Equation (10).

$$P_{cr} = \left(\frac{n\pi}{L}\right)^2 EI \qquad (10)$$

where *n* is the buckling mode, *L* is the length of the probe, and *EI* is the flexural rigidity of the probe. In order for the probe to be inserted successfully into the brain tissue without breaking, insertion should be done within the force range of the buckling strength. Inserting the probe with a force beyond the buckling strength will cause the probe to bend more, and then a mean minimal force perpendicular to the brain tissue will be exerted such that the probe will not penetrate the brain tissue.

In case of a tapered probe, a probe with varying cross-section along its length from the probe base toward its tip as depicted in Figure 2.4, Equation (10) depends on the variable in longitudinal direction stiffness factor *EI(y)*. Therefore, the law of distribution of the moment of inertia of a cross-section along the length of the probe may be presented by Equation (11).

$$I(d) = I_b\left\{1-(1-k^2)\frac{d}{L}\right\}^m \qquad (11)$$

here, *d* is a distance from the probe base section, with a cross-section area A_b and a moment of inertia I_b, to any considered section, with a cross-section area A_d and a moment of inertia I_d. The factor k^{2m} in Equation (11) is given by Equation (12).

$$k^{2m} = \frac{I_t}{I_b} \qquad (12)$$

where, m is a factor of the longitudinal distribution of the second moment of area which can be changed as m = 1,2,3 or 4 depending on the cross-sectional type. For instance, for m = 0 we obtain a probe of constant cross section; for m = 2 we obtain a pyramidal probe; for m = 3 we get a hollow cone, and for m = 4 a solid cone, etc. The differential equation of the tapered probe, as proposed by Dinnik [144], is represented in Equation (13).

$$EI\{1-(1-k^2)\frac{d}{l}\}^m y''+Py=0 \qquad (13)$$

where, l is a distance from the bigger end of the probe section up to a fictional point along the length probe where the second moment of cross-section area tends to zero. In such case, Equation (13) can be solved in terms of Bessel's functions [145] and may be presented as Equation (14).

$$P=S\frac{EI}{l^2} \qquad (14)$$

where, S is the coefficient of stability, depending on variability of the probe geometry and the mode of buckling. The values of S for different ratios of I_t/I_b were previously reported in [144].

Effective microelectrode design must be concerned with a tradeoff between the conflicting requirements of a small diameter to minimize tissue damage, and a large diameter to minimize buckling. To resolve these two factors, it is necessary to determine the critical buckling load which is a function of the electrode geometry and material properties and compared to the maximum anticipated forces applied to the electrode during their insertion into the brain. Jensen et al. tested *in vivo* electrode insertions into the cerebral cortex of rats and found that the maximal penetration force for an array of five *ACREO* electrodes to be (2.42 ±0.77 mN) [146]. Therefore, the designed reinforced electrodes must withstand this force when penetrating brain tissues.

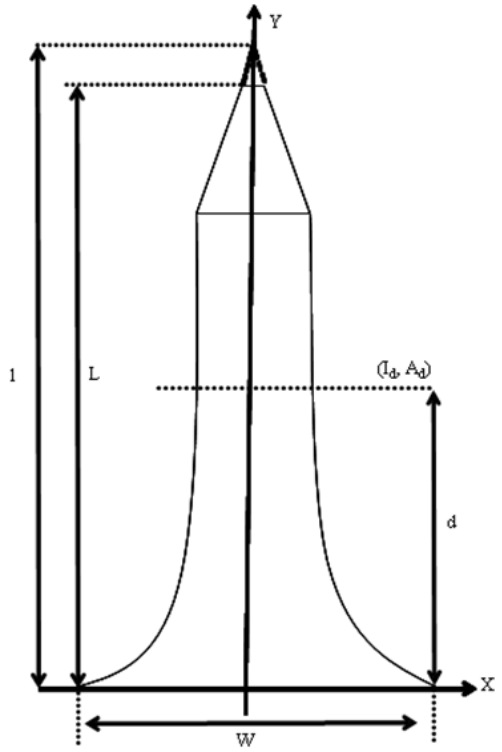

Figure 2-4: Geometric diagram of a single tapered probe electrode.

2.3 Numerical Modeling of Reinforced Electrodes

We detail studies to determine the reliability of the ultra-long neural probes as they are subjected to significant stresses due to imperfect insertion into the brain and/or due to movement of the brain relative to the skull. The main goals of the simulations are to predict the behavior of the probes when they are subjected to a downward bending force and an axial force as depicted in Figures 2.3(b) and 2.3(c) respectively. We show the simulated performance of proposed ultra-long probes, with and without structural reinforcement, (tip displacement, stiffness, critical load point, etc.) to fulfill the requirements for gathering cognitive neural information.

The simulations shown in Figure 2.5 and 2.6 were conducted using CoventorWare finite element analysis software, commonly used for developing MEMS devices, and using which a variety of MEMS devices can be modeled. The behavior of our probe electrode model was studied using the mechanical solver MemMech. The model was meshed into parabolic tetrahedrons with an element size of 4 microns which was

selected based on a convergence study to make sure that the numerical solution tends toward a unique value as the mesh density is increased. The convergence study was conducted by decreasing the mesh element size and running the same analysis. The element size of 4 microns was then selected when further mesh refinement produces negligible change in the electrode solution. The meshed model is presented to the mechanical solver where trajectories of two types of forces were applied, a vertical force (V) applied in the vertical direction at the face of the probe tip and an axial force (H) applied horizontally at the cross-section of the probe. The recording sites, interconnections, and the bonding pads were not considered for simulations.

These simulations are carried out to determine the maximum bending and buckling loads respectively. The loads were obtained at the point where the maximum stresses at weak regions of the probe reach 1GPa which is near the fracture stress limit for a thin silicon cantilever [147]. In the case of the bending force, the maximum value of stress in the probe is located at the bottom region and an average stress value is in the middle region (Figure 2.5) while in the case of an axial force, the maximum stress in the probe is in the middle region while an average stress value is present at the bottom region. The maximum average out-of-plane bending load, which causes the electrode to be broken, and the maximum average in-plane buckling force for different lengths of the Micragem and McGill arrays as determined by simulations using CoventorWare software tool, [148], are summarized in Table 2.1.

Table 2.1: Comparative buckling simulations results of the reinforced and non-reinforced electrodes of the Micragem and McGill arrays.

Electrode	Critical buckling load (without reinforcement)	Critical buckling load (with reinforcement)	Critical vertical loading (with reinforcement)
6.5mm	0.575 N	0.724 N	0.085 N
4.5mm	0.8505 N	0.971 N	0.1449 N
2.5mm	0.975 N	1.23 N	0.1653 N
10.5mm	0.307 N	0.371 N	-

As shown in Equations (3) and (14), the critical bending and buckling loads are, respectively, inversely proportional to the thickness and the thickness squared of the probe. Therefore, the stability of the probe always can be improved by increasing its thickness, but such a design will increase the damage of the brain tissues during implantation of the probe. A better solution is obtained by keeping the same thickness of the probe as small as possible and increasing the stability by introducing reinforcing structures. In the case of an axially compressed probe as shown in Figure 2.3(c), its stability can be made greater by adding a stiff longitudinal reinforcing structure of suitable cross-section. The volume of such a reinforcement structure will be much smaller than the additional volume introduced by an increasing the probe thickness.

In our present application, the horizontal force component is very important as it determines the force at which the probe tip penetrates the brain tissue. Therefore, it is important to reinforce the probe at the middle because for this kind of force load the maximum stress is in the middle of the probe where the probe is the most susceptible for breakage. The design of our new reinforced probe is structurally similar to the standard probe but with additional metal layers added to strengthen its weaker areas, that is, at the middle of the probe. Adding a strip of metal at the middle of the probes increased its tensile strength when compared to the standard probe by pushing back the maximum stress in the middle to the bottom region of the probe which is typically sturdier as shown in Figures 2.5 and 2.6. This enables the probe to be more resistant to the axial buckling force exerted by the brain tissue during the implantation phase. The reinforcing structures are made of the metal layer employed to form the recording sites which is 750nm thick. The length of the reinforcing structures was varied in the simulation to determine the optimal length that renders the neural probe survives the maximum force encountered during the implantation in the brain tissue.

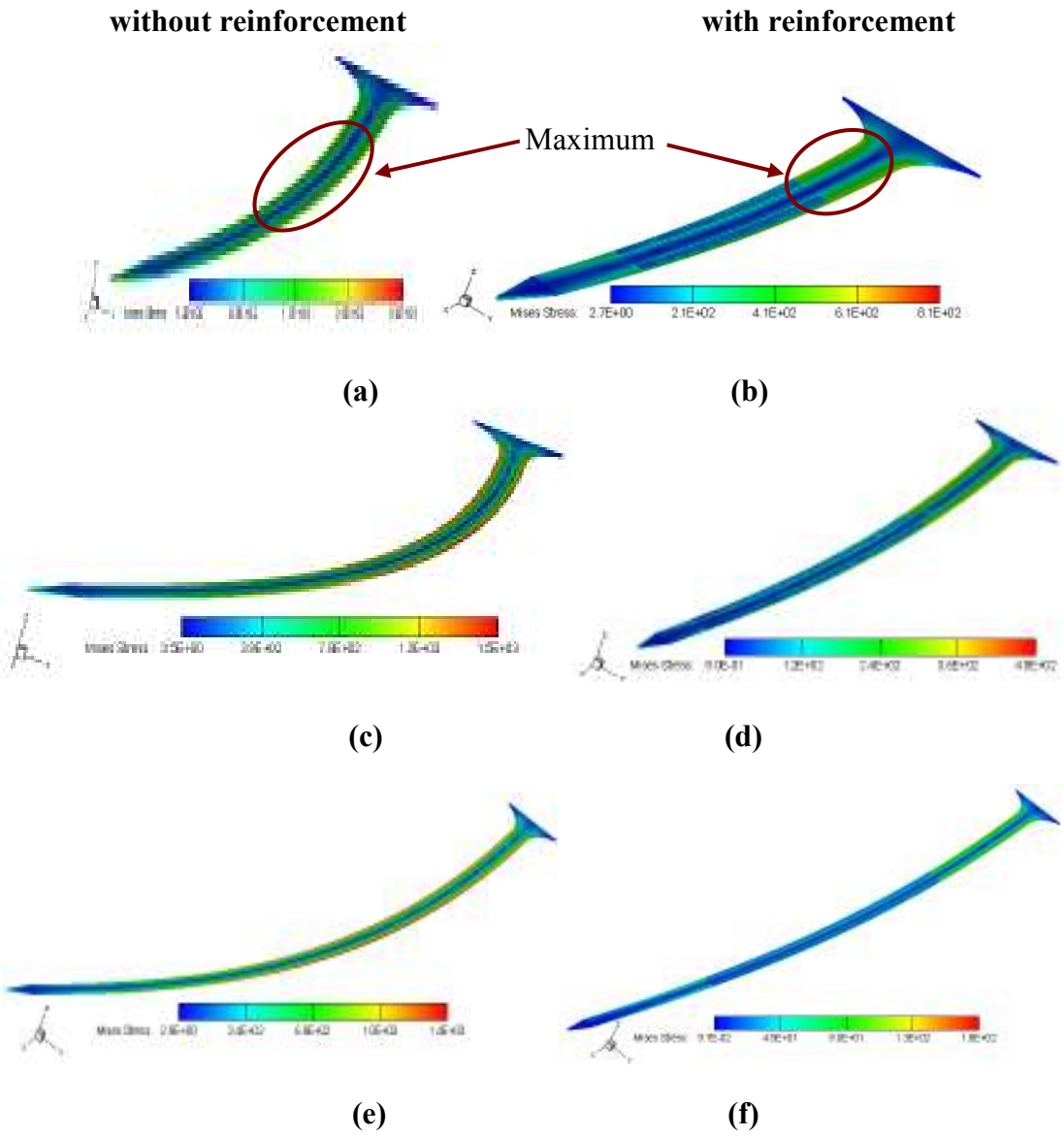

Figure 2-5: Behavior of the 2.5mm ((a),(b)); 4.5 mm ((c),(d)); and 6.5mm ((e),(f)) probes, without and with reinforcement respectively, when they are subjected to axial horizontal force.

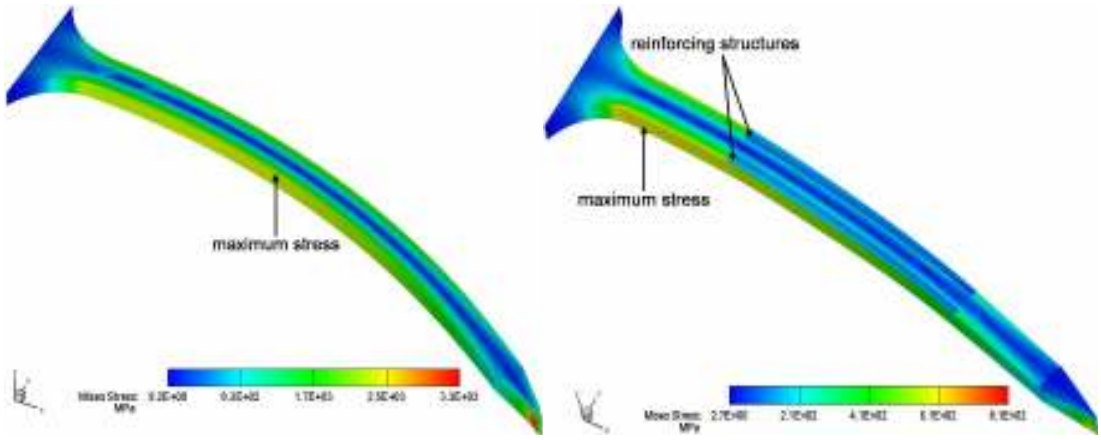

(a) **(b)**

Figure 2-6: Behavior of the 10.5mm long probe electrodes, (a) Without; (b) With reinforcement, when they are subjected to axial horizontal force.

2.4 Fabrication Process of the MicraGem Array

The developed neural electrode array consists of five probes fabricated using the standard MicraGem process from Microlyne Inc [149]. Figure 2.7 illustrates the steps of the MicraGem fabrication process. The process starts with a 500±25 μm thick glass (Pyrex) wafer which is patterned and isotropic wet etched, as depicted in Figure 2.7(a), to form a cavity which is used to suspend the probes. Then, a Silicon-on-Insulator (SOI) wafer is turned device layer down and anodic bonded to the patterned glass substrate as depicted in Figure 2.7(b). The silicon handle and buried oxide layers are then etched away completely using a wet etch process leaving behind the exposed single-crystal silicon layer (device layer) bonded to the glass as illustrated in Figure 2.7(c). The developed probes are made of this single-crystal silicon layer which is 10μm thick. Metal layers are then deposited over the single-crystal silicon surface consisting of 500Å thick Titanium-Tungsten, as an adhesion interfacing layer, and 2000Å thick gold layer. The metal layers are lithographically patterned and then wet etched to form the recording pads, trace lines (interconnects), bonding pads, and the reinforcing layer as depicted in Figure 2.7(d). Then, the single-crystal silicon layer is lithographically patterned and then etched completely using a DRIE process to form the electrode probes as illustrated in Figure 2.7(e). Finally, the electrode structures are

released from the Pyrex support with a post-fabrication process step by etching the intermediate silicon dioxide layer, formed during the anodic bonding of the SOI wafer to the Pyrex wafer, using buffered hydrofluoric acid as illustrated in Figure 2.7(f).

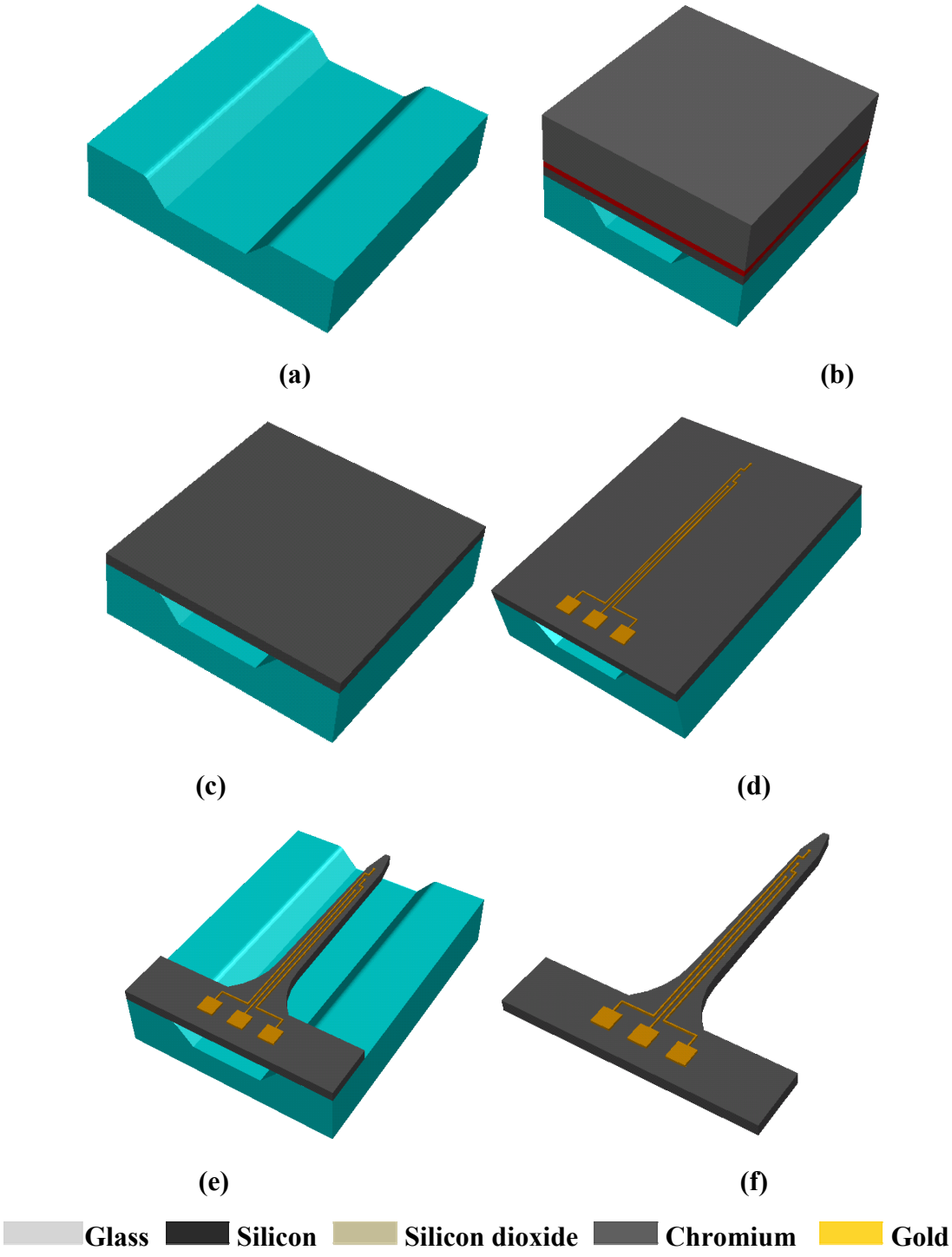

Figure 2-7: Schematic illustration of the standard MicraGem microfabrication process.

The microelectrode array were encapsulated using Parylene-C as a biocompatible layer for surgical implantation with only the recording sites exposed to the neurons [43]. The complete fabricated sample is shown in Figure 2.8(a). Figure 2.8(b) shows a magnified view of the reinforced probe tip and one of the recording sites. The Figures 2.8(c) and 2.8(d) show reinforced and non-reinforced electrodes respectively. The recording sites, interconnections are also shown in these figures. These structures are made of low stress metal deposited with low average residual stress that provides long term reliability. The silicon and metal structures shown in Figure 2.8 are well defined and uniform which is characteristic of the commercial MEMS process.

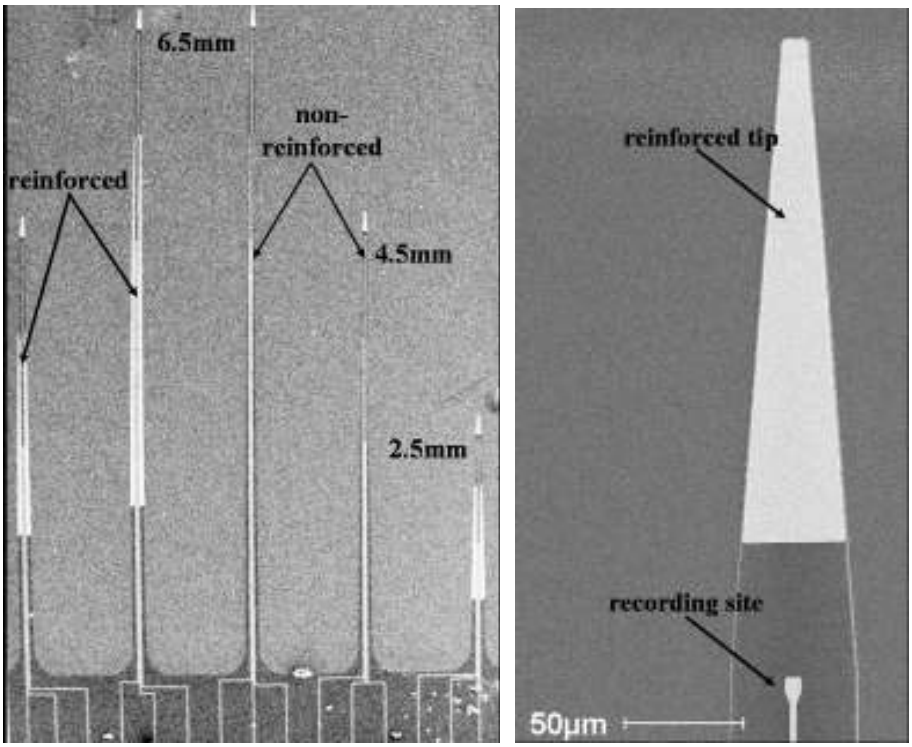

(a) **(b)**

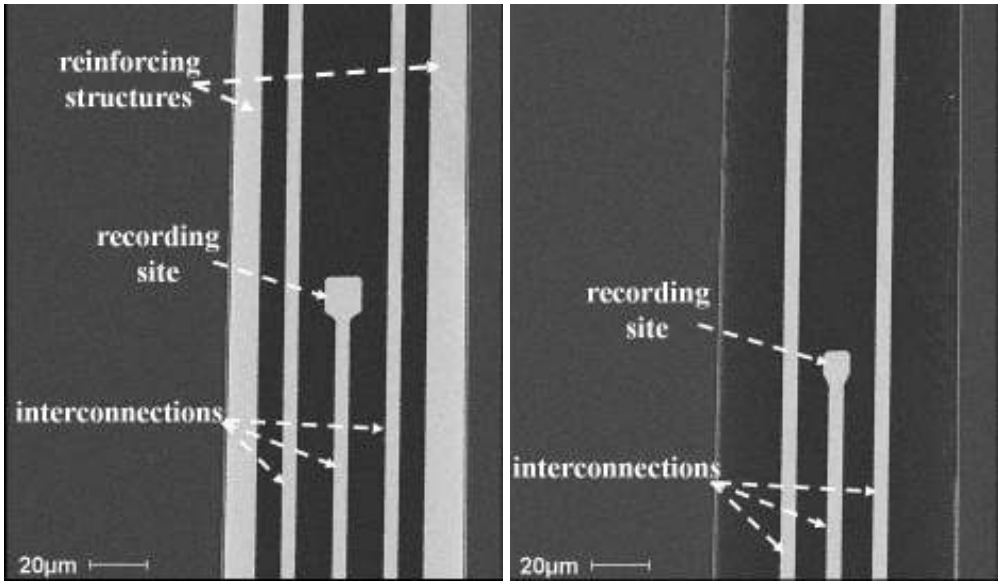

(c) **(d)**

Figure 2-8: SEM photos of the fabricated array using the standard MicraGem process (a) probe array; (b) tip of the electrode; (c) reinforced electrode at the middle region; (d) non-reinforced electrode.

2.5 Fabrication Process of the McGill Array

Figure 2.9 shows the cross-sectional view of the microfabrication process for the neural electrode array. The process starts with a 50µm thick, 4" diameter double side polished, silicon wafer as substrate material. First, metal layers of titanium (adhesion layer, 500nm thick) and gold (conducting layer, 750nm thick) were deposited on the silicon wafer as illustrated in Figure 2.9(a). Second, the gold and titanium layers were photo-lithographically patterned and etched, with (1:2: 10; I_2:KI:H_2O) and (20:1:1 H_2O: HF:H_2O_2) respectively, to define the recording pads, reinforcement layer, and interconnects between the recording sites and bonding pads (Figure 2.9(b)). Finally, the silicon substrate was patterned and etched using an isotropic Xenon Di-fluoride (XeF_2) etching system to form the electrode probes (Figure 2.9(c)). Dipping in 10 % hydrofluoric acid (HF) was carried out to produce neural probes with smooth structures.

The XeF_2 etching technique was selected as it provides unique advantages compared to wet and other dry etch techniques and specifically related to its high etch rate (1 to 3 μm/minute at room temperature), high aspect ratios, selectivity, and simplicity [18]. The high selectivity of the XeF_2 etching to silicon can be used to make high-aspect structures with little or no degradation of the etch-stop or masking layer. Standard hard-baked photoresist can serve as an effective mask for deep and extended etches to obtain high aspect ratios. The use of a photoresist as masking layer simplifies the fabrication process by obviating the need for deposition, patterning, and etching of silicon dioxide or silicon nitride masking layers commonly used for other silicon dry or wet etch techniques.

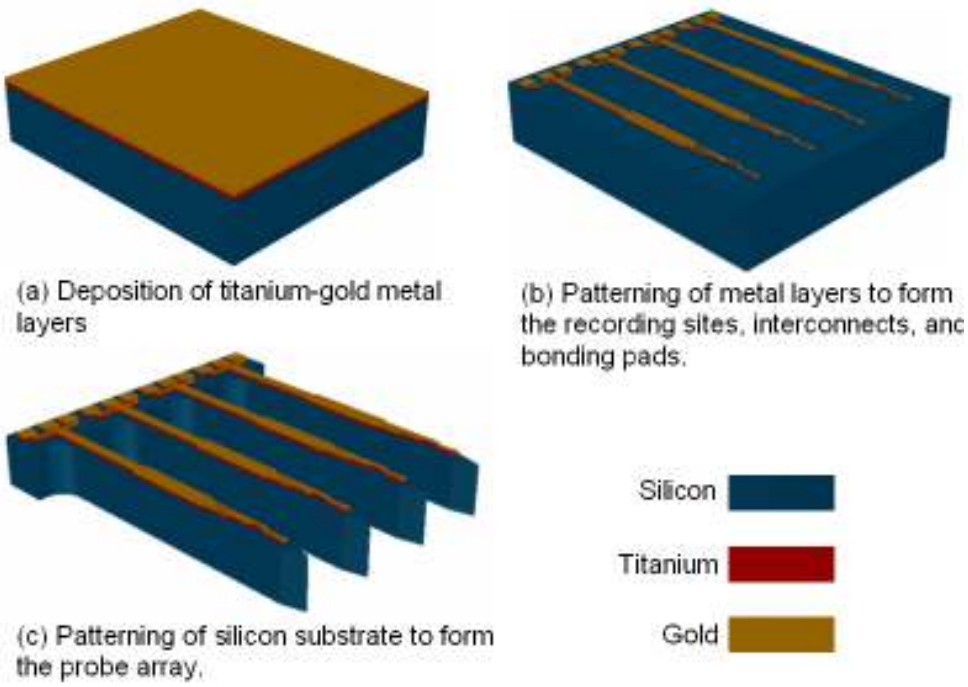

Figure 2-9: Schematic illustration of the steps involved in the fabrication process of the McGill neural probe array. The figure is not to scale.

Figure 2.10(a) is a photomicrograph for the fabricated electrode array. Figure 2.10(b) is a scanning electron microscope (SEM) picture of the piercing and recording regions of a single electrode. It shows a well-defined, tapered, and sharp tip of the electrode. It also shows the 20μmx20μm recording sites. The reinforcing structures located in the

middle of the probes are shown in Figure 2.10(c). The interconnect lines shown are 10μm wide. Figure 2.10(d) shows the tapered base of probe electrode. Figure 2.10(e) shows the cross-section view of the probe electrode. The microelectrode array was encapsulated using Parylene-C as a biocompatible layer for surgical implantation with only the recording sites exposed to the neurons [19].

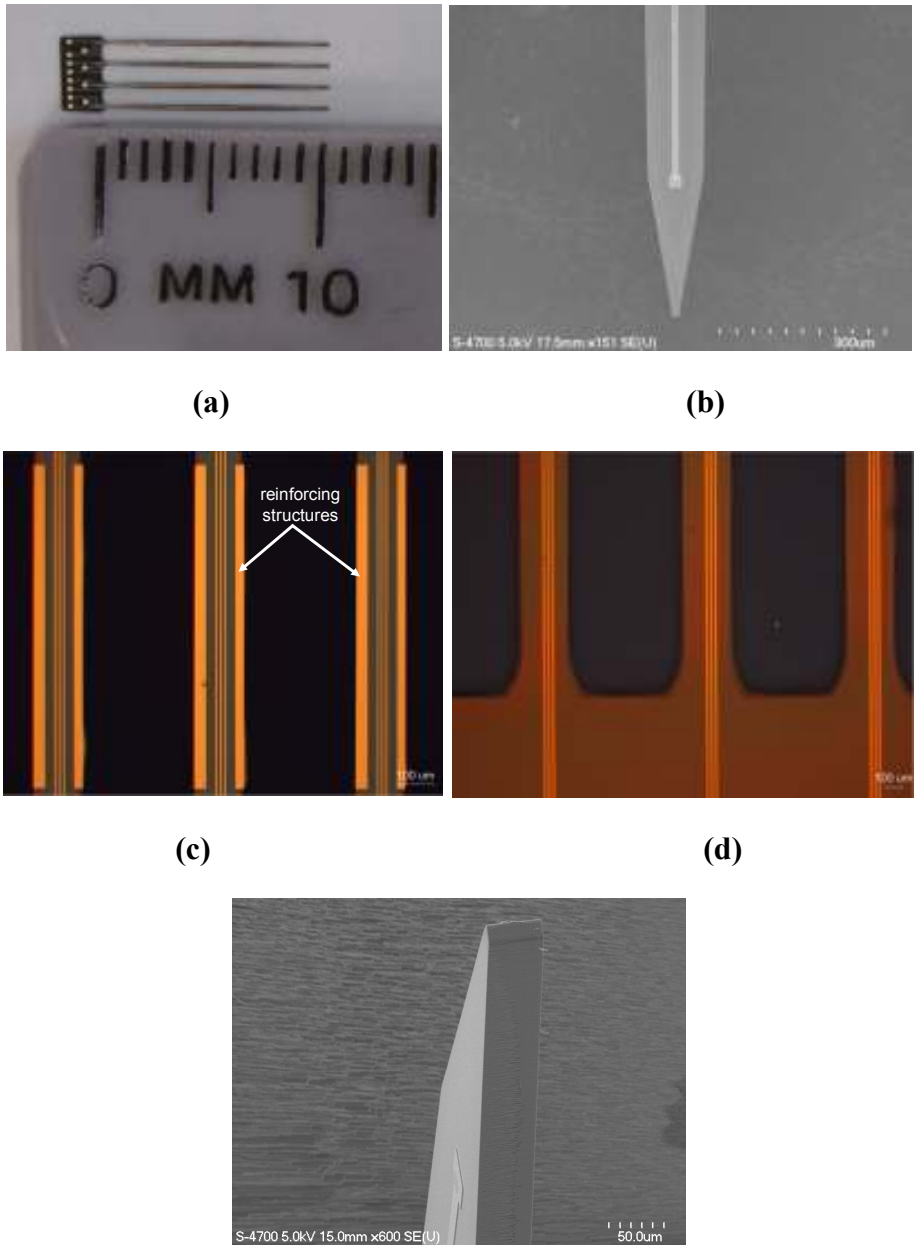

(a) **(b)**

(c) **(d)**

(e)

Figure 2-10: Microphotographs of the fabricated electrode array. (a) Picture of the fabricated electrode array; (b) Close-up view of the probe tip and the three

10µmx10µm recording sites; (c) Picture of the reinforcing structures; (d) View of the tapered base of the electrodes; (e) Cross-sectional view of the probe electrode.

2.6 Electrode Impedance and *In-Vivo* Tests

The electrode impedance is critical in the design of neural probes. The equivalent circuit of a microelectrode is shown in Figure 2.11. The physical origins of the components are as follows: *Z*a is the input impedance of the amplifier, *Cs* is all the shunt capacitance to ground from the electrode to the input of the amplifier, *Rm* is the resistance of the metallic portion of the microelectrode, *Ce* is the capacitance of the electric double layer at the interface of the electrode opening and the electrolyte solution, *Re* is the leakage resistance due to charge carriers crossing the electric double layer, *Rs* is the resistance of the saline bath between the metallic interface of the electrode and infinity (ground electrode) (This is sometimes called the spreading resistance.), and e_n is the potential created in the volume conductor with respect to a point at infinity by the extracellular currents flowing about a neuron during an action potential.

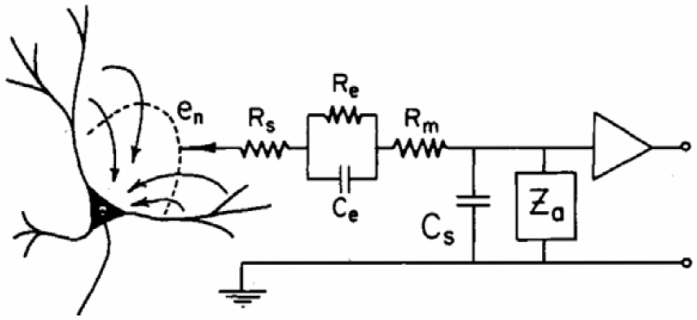

Figure 2-11: The equivalent circuit of a microelectrode

From rough calculation, we can find that the dominant part of the electrode impedance at 1 KHz is *Ce*, which is the capacitance of the electric double layer. Therefore the electrode impedance is dominated by the size of the electrode opening, as characterized by the electrode impedance dependence on the size of the plasma-etch-

opened metal electrodes. The testing data allow us to determine the optimum material and size of the electrodes for different applications.

The impedance for all the recording sites of an array consisting of 4 electrodes was measured at 1kHz in isotonic saline solution and is shown in Figure 2.11. The impedance for all the recording sites is around 500KΩ, suitable impedance to record single neuron activity and local field potentials (LFPs).

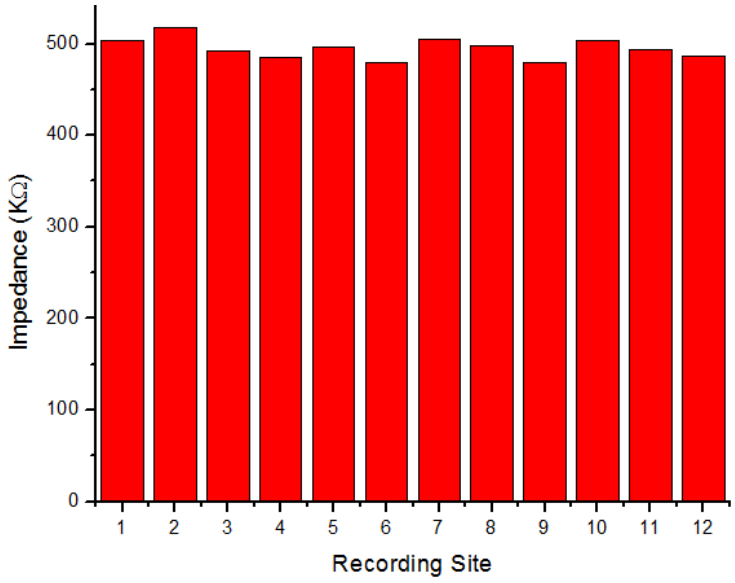

Figure 2-12: Impedance of the recording sites at 1 KHz.

The devices were inserted through the pia and cortex of live rats to test their penetration ability. Results show a full insertion of the probe was successful without any bending, buckling, or breakage. Spiking activity and local field potentials (LFP) were recorded simultaneously from the 4 electrodes using a multi-channel acquisition processor as shown in Figure 2.11 (a) and (b).

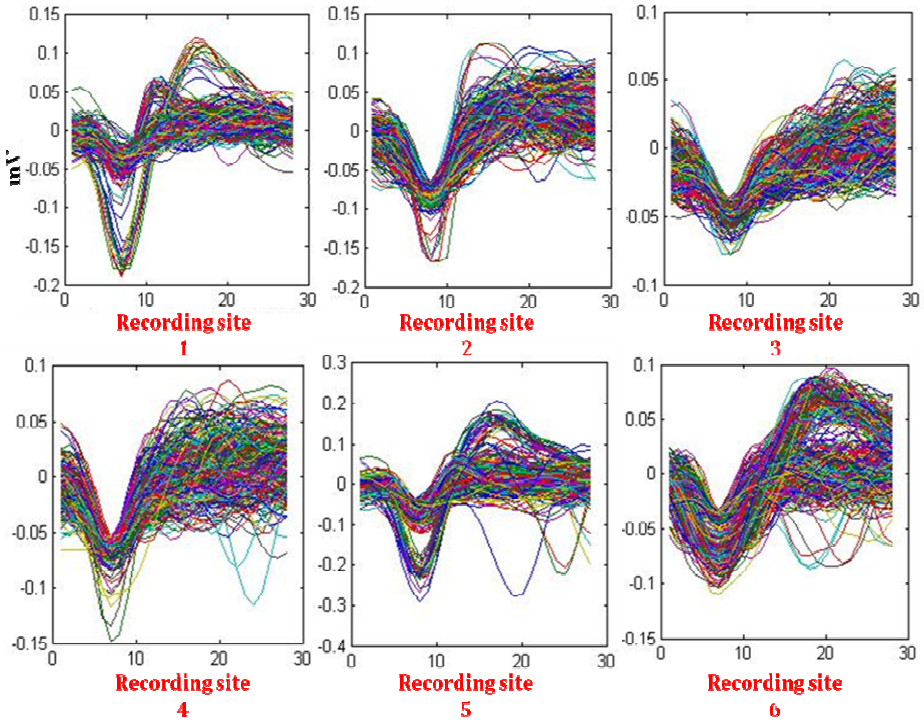

(a)

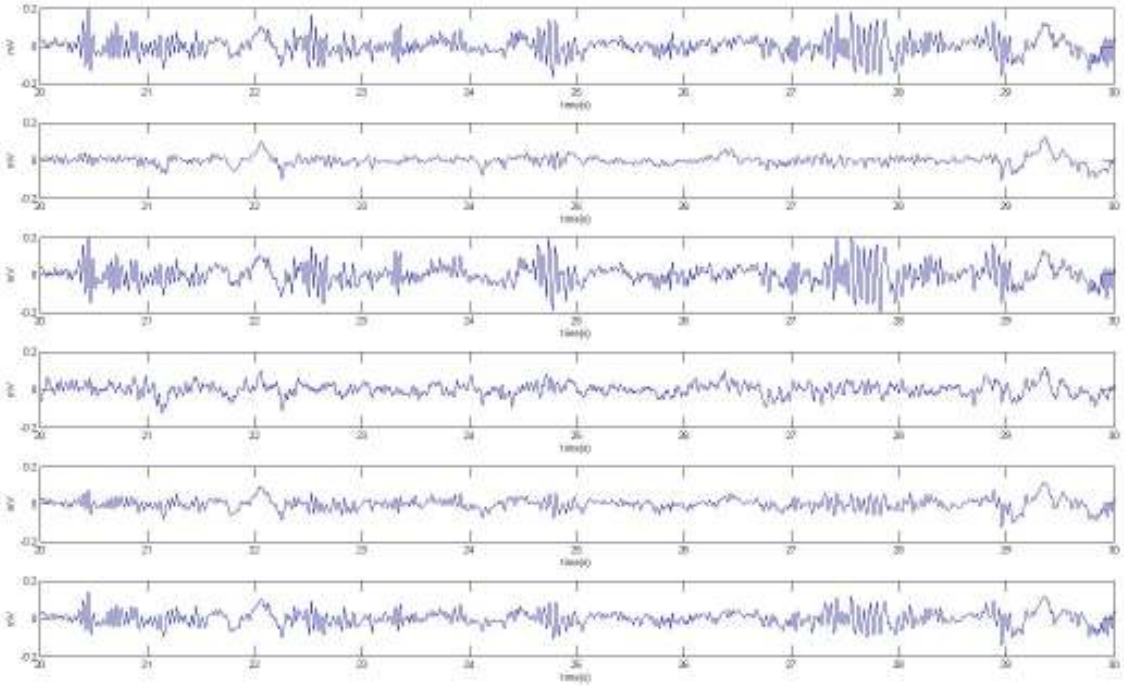

(b)

Figure 2-13: Spikes and Local Field Potentials (LFPs) recorded from the rat barrel cortex.

2.7 Mechanical Testing of the Electrodes

A successful penetration of the neural probes electrodes into brain tissue occurs with no breakage or excessive dimpling. Hence, it is important to analyze and define the operational limits of the silicon-based neural microelectrodes. The pre-defined limit to which the electrodes can be stressed is often referred to as the buckling load which represents the maximum allowable compressive loads that the probe electrodes are capable of withstanding without failure. We performed experimental evaluation to determine the mechanical stability of the neural electrodes by determining the critical buckling load. The fabricated neural electrode array has 5 probes with 1 probe of 2.5mm length, 2 probes of 4.5mm length, and 2 probes of 6.5mm length (Figure 2.8(a)). In order to compare the critical loads of the reinforced and non-reinforced probe electrodes, the fabricated sample includes one 4.5mm and one 6.5mm long electrodes that are reinforced and the other two of the same lengths left non-reinforced. The McGill array consists of four 10.5mm long electrodes, two electrodes are reinforced and the other two are non-reinforced.

In our application, the probe electrodes can be treated as cantilever beams that are fixed at the base end and free to move at the tip end. When a critical load is applied, buckling occurs in the plane perpendicular to the corresponding principal axis of inertia. The critical loads are calculated by buckling the probe electrodes, as illustrated in Figure 2.11, until the electrodes break and by measuring the maximum deflection, d_{max}.

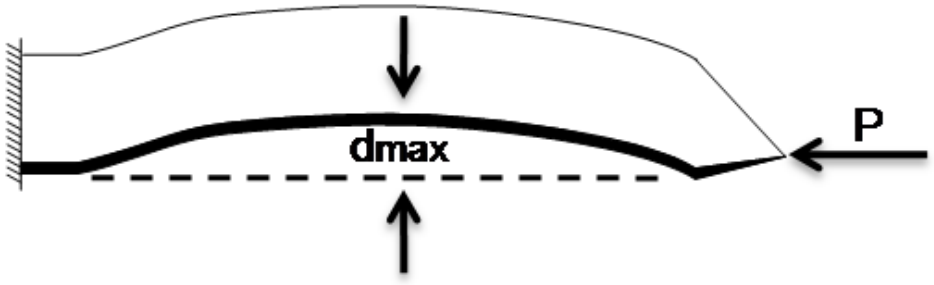

Figure 2-14: Diagram of single probe electrode under buckling deflection condition.

Equations (15) and (16) were used to calculate the critical stress σ_{cr} [72]. The critical stress is then used to find the critical load, P_{cr}, of the beam being loaded.

$$d_{\max} = \frac{\sigma_{cr} L^2}{6Et} \qquad (15)$$

$$P_{cr} = \sigma_{cr} A \qquad (16)$$

where, E is the elastic modulus for silicon and is assumed to be 190 GPa [150], t is the probe electrode thickness, L is effective length which is equal to one half the actual length of the probe electrode as it is determined by the method of support [72].

In this experiment, a horizontal loading setup was used for the buckling studies. The test platform consists of the electrode array mounted and glued on a custom-designed printed circuit board using an epoxy material to allow easy handling of the array during the test procedure as shown in Figure 2.12. The PCB board is then mounted on a motion controller to allow slow advancement of the probe electrodes in small and accurate steps. Figure 2.13(a) shows the MicraGem electrodes in initial load phase as pressed against a hard plastic surface. As the electrodes moved forward and pressed against the hard surface, the deflection of the electrodes increased. Figures 2.13(b), (c), (d), and (e) provide a visual explanation of the buckling experiment where the non-reinforced electrodes of all 6.5 mm, 4.5mm, and 10.5mm lengths deflect and buckle more than the reinforced electrodes of the same length.

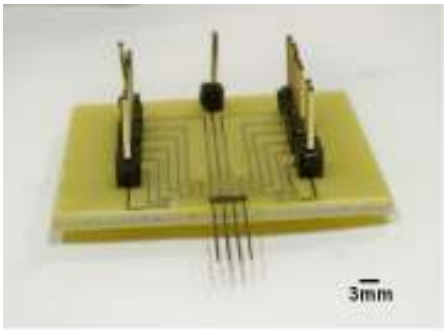

Figure 2-15: Neural probe mounted on Printed Circuit Board (PCB).

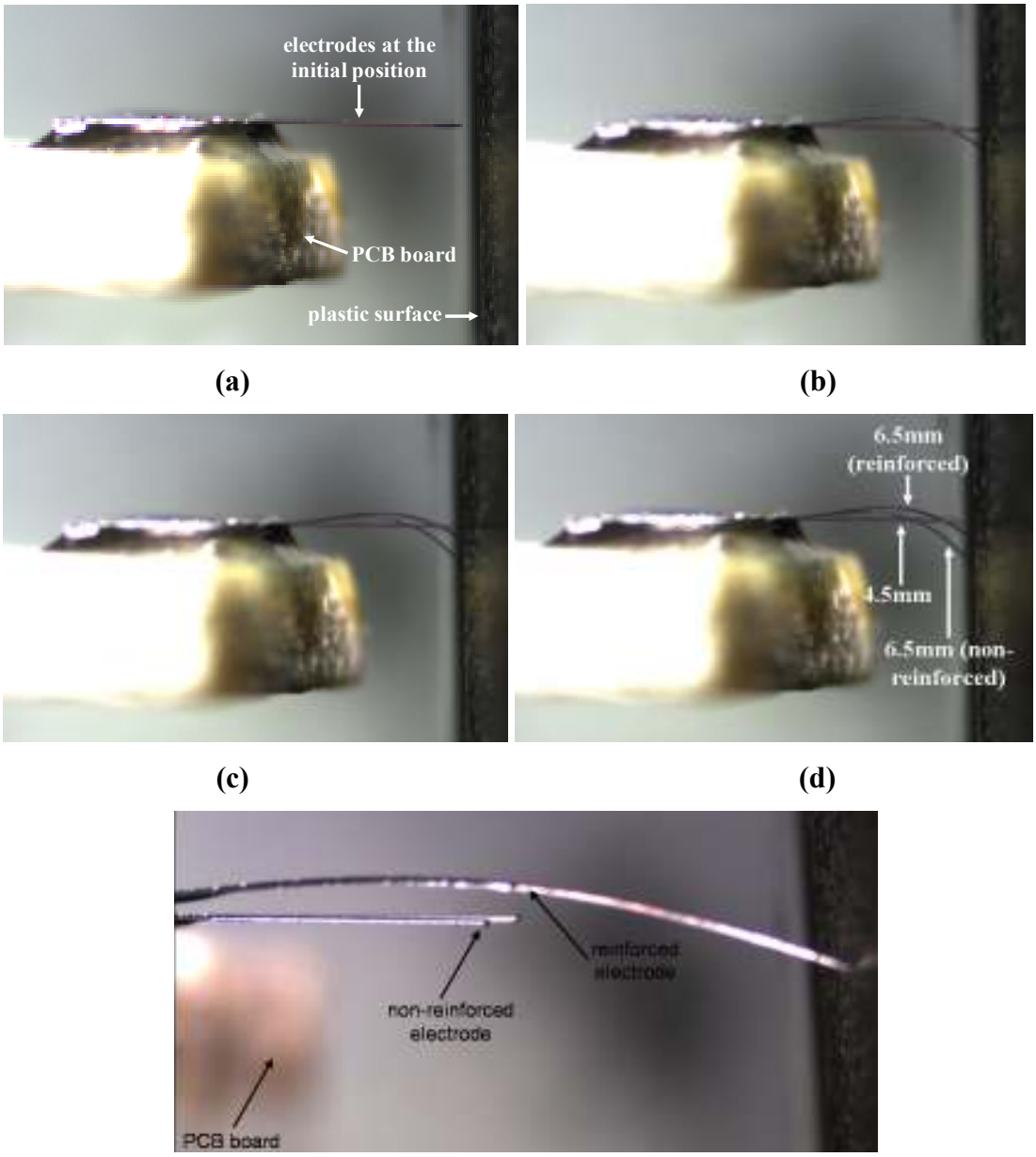

Figure 2-16: Buckling testing of MicraGem and McGill arrays when pressed against hard plastic surface.

The values of maximum deflections d_{max} of the reinforced and non-reinforced electrodes were measured at the last point before fracture using a microscope and a micrometer grid. Based on the stress deflection Equations (15) and (16) described previously, the critical stress of the reinforced and non-reinforced probe electrodes as they are pressed against the hard surface were calculated as summarized in Table 2.2.

Table 2.2: Comparative buckling test results of different lengths of the reinforced and non-reinforced electrodes.

Electrode	Measured critical buckling load (without reinforcement)	Measured critical buckling load (with reinforcement)
6.5mm	0.561 N	0.717 N
4.5mm	0.847 N	0.976 N
2.5mm	0.96 N	-
10.5mm	0.313 N	0.364 N

The buckling experiment was repeated three times for three different arrays and there was no statistically significant difference. The measured critical buckling loads are in good agreement with the simulation results. As shown in equations (10) and (14), the buckling load is inversely proportional to the probe length squared. This explains the reduction of the reinforcement effect for the longer electrodes.

2.8 Summary

This Chapter is based on the following two papers published by our group: "Reinforced Silicon Neural Microelectrode Array Fabricated Using a Commercial MEMS process",SPIE Journal of Micro/Nanolithography, MEMS, and MOEMS, vol. 8(3), 2009., and "Microfabrication of Ultra-long Reinforced Silicon Neural Electrodes", Micro & Nano Letters, vol. 4, pp. 53-58, 2009.

In this Chapter, we demonstrated a silicon microelectrode array for brain machine interfaces fabricated in a commercial MEMS process available from Micralyne Inc. The use of standard fabrication processes yields mass-producible and well-defined probe structures. We presented the design, analytical, and numerical models to study the stress and deflection of neural microelectrodes during various scenarios of surgical implantation and usage. We demonstrated elongated silicon microelectrodes that are up to 6.5mm in length with only 10μm thickness that are suitable to gather cognitive neural information from deeper regions of brain. We described a new concept of

reinforcing the regions of the microelectrodes that are more susceptible to breakage to enhance their stiffness, durability, and functionality in order to serve as optimal implantable microstructures for integrated brain machine interfaces.

We also report the first demonstrated neural microelectrode array fabricated using standard ultra-thin silicon wafers as substrates and XeF_2 etching system. The microfabrication process provides a rapid, cost-effective, and high-yield platform to manufacture neural electrodes required to gather cognitive neural information. We also introduce a novel concept of structural reinforcement for neural electrodes to improve their tensile strength for deep implantation studies. The reinforcement increases the stability of the electrodes by augmenting the critical buckling load by approximately 50mN. The resulting neural electrodes reach comparatively elongated lengths of 10.5mm having only 50μm thickness. The developed electrodes possess well-defined structural features with smooth surfaces.

CHAPTER 3

OXYGEN SENSORY PLATFORM

Multi-sensor systems and sensor microarrays are undergoing rapid development because they can multiplex and de-multiplex biological or chemical information from multi-component samples [151-152]. Use of optical methods for sensing in the field of biochemistry and analytical or clinical chemistry offers multiple benefits including non-destructive testing, rapid signal generation and reading, capability for remote and multiple sensing, flexibility and ease of miniaturization [153]. Physical basis for the optical sensing lies in the information provided by the light's changes as it travels through the sensing medium, including changes in absorption, fluorescence, luminescence, scatter or refractive index [154]. This gave rise to several optical detection methods, such as total internal reflection spectroscopy, surface plasmon resonance, fluorescence or absorption spectroscopy and others. To gain more insight into different optical sensing techniques, the reader is referred to [155]. Among these, fluorescence detection is the most common tool in modern chemical and biochemical analysis. For achieving the highest possible detection sensitivity, optical detection based on fluorescence spectroscopy is currently considered state of the art [156]. Optical sensing based on fluorescence spectroscopy is a well established technique for highly selective and sensitive biochemical sensing [157-158]. In comparison to competing approaches, optical sensors may be less susceptible to contamination while providing fast multiplexed response and high efficiency. To date, a number of platforms have been demonstrated for optical biochemical sensor arrays. Some platforms use optical fibers [159], planar waveguides [160], some of which have been coupled with micro-LED arrays [161], and arrays on a LED [162].

The objective of this chapter is to develop polymeric waveguide support platform for optical multi-sensor systems based on fluorescence detection. Specifically, we demonstrated a waveguide array structure made with direct-dispense to support sol-gel

derived xerogel recognition materials which are made responsive to oxygen concentration. These waveguide sensors are embedded in the elongated silicon mciroelectrodes described in Chapter 2 to form the desired multiple measurand neural probe. The proposed waveguide based sensors offer a degree of robustness and that can be integrated relatively easily into microfluidic structures for lab-on-chip applications [163]. The waveguide structures act as a support platform for immobilizing biochemical recognition elements. We describe a direct-dispense fabrication process to implement the waveguide based sensor arrays. Direct-dispense and direct-write techniques are commonly used for advanced microelectronic packaging, microfabrication, and microelectrodes development [164-165]. With direct-dispense, select materials can be precisely deposited with features on the order of several micrometers through a microscale nozzle. A longer term objective is to evaluate the potential of direct-dispense techniques for low-cost printable optical sensor arrays. Recently, a number of research groups including ours have employed the direct-dispense technique to create microfluidic channels and other microstructures [166-167]. In literature, we find several fabrication techniques that have been grouped as direct-write techniques which include laser (optical) lithography, ink-jet printing and screen printing [168]. The fabrication technique described here is one example of the several direct-write techniques and involves mechanical robotic deposition to pattern fugitive organic inks on a substrate. Optically transparent epoxy or polymeric materials are then deposited with direct-dispense system using the previously deposited fugitive ink structures as guide or sacrificial layers in a way that is reminiscent of the use of positive photoresists. Subsequently, the fugitive ink is thermally removed leaving behind micropatterned epoxy or polymeric structures. This process can be repeated to create complex polymeric microstructures that can be used as high-performance, multi-functional sensor platforms which can support microfluidics and optical signal collection and transmission.

3.1 Fluorescence Sensing

When molecules absorb photons at a given wavelength, they undergo either electronic or both electronic and vibrational excitation. The absorbed energy is normally dissipated in the form of heat; however, some molecules have the ability to re-emit part of this energy as longer wavelength photons, by means of fluorescence. Electronic and vibrational level transitions involved in fluorescence phenomena can be understood with the aid of a Jablonski energy level diagram shown in Figure 3.1[169].

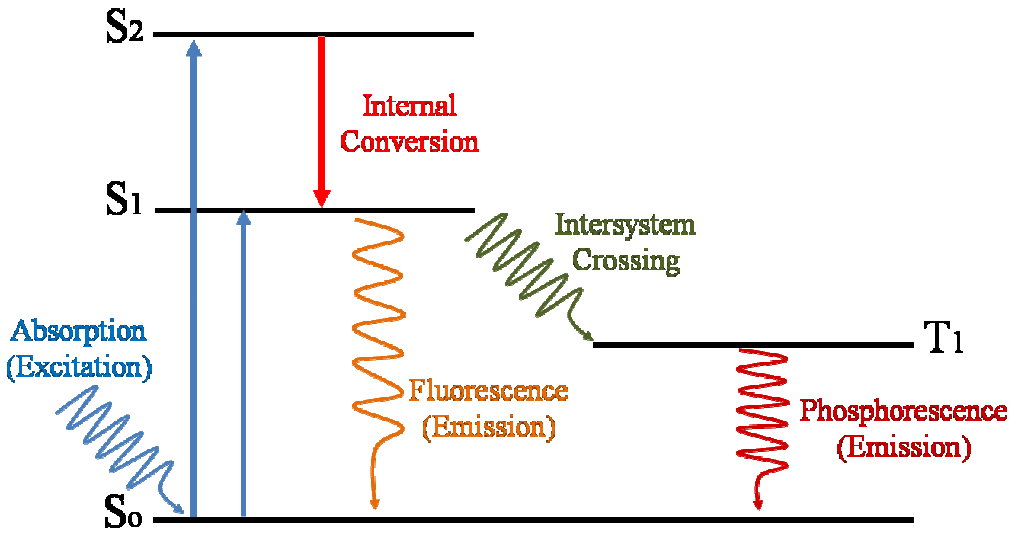

Figure 3-1: Representation using Jablonski diagram. Taken from [169].

From Figure 3.1, upon absorption of a photon, an electron gains enough energy to move from a ground state, S_0 towards an excited state, S_1. The electron will then lose part of its energy by vibrational relaxation to reach the lowest energy level of the excited state S_1. This is followed by fluorescence, where the electron returns to the ground state, S_0, by releasing the remaining energy in the form of a photon. Due to the loss of energy during the internal conversion in the excited state, the total energy of the emitted photon is lower than that of the excitation photon, resulting in the difference between the excitation and emission wavelengths, termed Stokes' shift. Through the use of suitable filters, this small shift in wavelength enables the detection of a small number of emitted photons in presence of large excess of excitation

photons. Many chemical structures are known to be fluorescent. The spectral characteristics of the fluorescing base structures are sensitive to their chemical environment, thus allowing the fluorescent labelling of different analytes and their successive detection. A large variety of chemicals can be characterized using analyte-specific fluorescence dyes including sodium, oxygen, calcium, chlorine, potassium, carbon dioxide, several halides, some toxic chemicals like sulphur dioxide, a number of gases and other chemical reagents [170]. Fluorescence can also be used to characterize proteins, membranes and DNA labelled by fluorescent probes. Moreover, use of fluorescence enables the determination of multiple analytes in parallel [156]. Fluorescence detection can thus be employed for biomedical applications such as reaction process monitoring, or hazardous agent detection. Other target applications include point-of-care diagnostics, high-throughput screening, forensic tools, personal safety, food quality control, and any environmental monitoring [158].

3.2 Fluorescence Detection from Xerogel-Based Sensors

Sol-gel derived materials have a good potential for creating sensor arrays in combination with direct-dispense techniques. Several reports describe the use of sol-gel-processed xerogels as encapsulation media for various biochemical recognition elements [171-173]. Xerogels offer a number of advantages, including low temperature processing, optical transparency, relative long time stability, and straightforward doping procedures to encapsulate guest sensing elements. Xerogel sensor materials have been deposited using pin-printing [171], dip-coating [159], spin-coating [174], and photo- (ultraviolet) patterning [175]. This flexibility makes xerogels attractive to combine with the direct- dispense method. In this Chapter, we show how modified xerogels can be deposited selectively and integrated with a patterned polymeric support platform using direct-dispensing. Ru(II) diimine complexes have relatively long lived triplet metal-to-ligand charge transfer states that make them useful for quenchometric sensing. We use *tris*(2,2'-bipyridyl)dichlororuthenium(II) hexahydrate ([Ru(bpy)3]2+·6H2O) as the guest luminophore in the xerogel, because it is one of the more widely studied complexes

for oxygen sensing by luminescence quenching. For the prototype discussed in this Chapter, we use an optically transparent epoxy Epo-Tek 301-1 (Epoxy Technologies Inc.) to fabricate polymer ridge waveguides. Figure 3.2 shows a simplified block diagram of the prototype optical sensor platform implementing the polymeric waveguide support platform and xerogel sensor materials. Other configurations common to existing optical chemical sensors are also possible where the excitation source and the photodetector are on the either side of the xerogel sensor array or both the excitation source and the photodetector are on the same side (top or bottom) of the sensor array [163, 176-177].

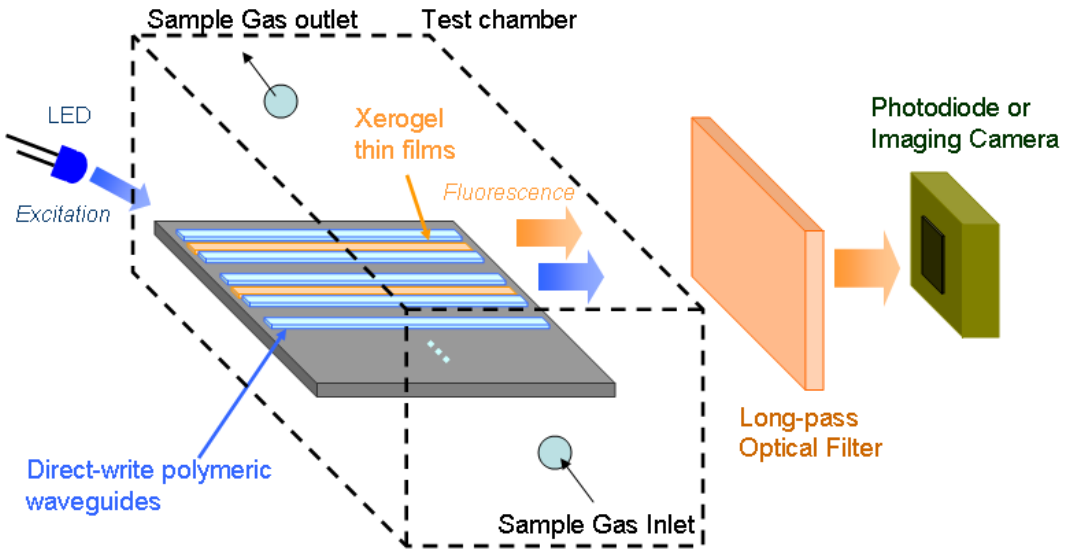

Figure 3-2: Simplified block diagram of the optical sensor system implementing the polymeric waveguide support platform and xerogel recognition materials.

Following Figure 3.2, the sensor partly uses direct LED excitation and partly guided evanescent-wave excitation due to the exponentially decaying evanescent field from the multimode waveguides [159, 178]. Subsequently, fluorescence is generated from Ru(II) complexes trapped in the xerogel claddings with an intensity proportional to the target analyte concentration. A part of this generated fluorescence is captured by the waveguides and channeled to a photodetector. In the following sections of this Chapter, we describe the direct-dispense technique to create the waveguide structures,

preparation of the modified xerogel sensor materials that are suitable for direct-dispense process, and finally, the integration of a xerogel sensor film with the waveguide structures.

3.3 Direct-Dispense Fabrication of Waveguide Structures

A robotic deposition tool (Model I&J 2200, FISNAR Inc.) was used for the direct-dispense process, in which a fugitive ink, typically consisting of a composite of 75% of petroleum jelly and 25% of microcrystalline wax, was extruded through a micro-nozzle (Model 2400, EFD Inc.) and deposited onto a substrate. Typical substrates may be selected from plastic, generic microscope borosilicate glass slides, or fragments of silicon wafers [166-167]. The automated direct-dispense tool is as shown in Figure 3.3. The pattern to be written is first mapped out as a trajectory by programming it into the robot, which in turn commands and controls the dispensing system to emit the fugitive ink from the nozzle. In the simplest case (Figure 3.3), straight lines of the fugitive ink are deposited. Next, uncured liquid polymer resin is deposited at room temperature with the direct-dispense apparatus. The fugitive ink pattern acts as a periodic reservoir to hold the fluid resin, which is subsequently cured. The ink is then melted at 65^{o}C and extracted, leaving behind patterned polymeric microstructures. Figures 3.4(a), (b), and (c) depict the fabrication steps for the direct-dispense process. The fugitive ink layer must have appropriate flow viscosity, solidify and adhere well to the substrate and melt at a sufficiently low temperature to yield uniform quality and reproducible structures from polymer resins. As an example, Figure 3.5 shows functionality of the direct-dispense system to fabricate different microchannels.

Accordingly, the direct-dispense system is programmed to make multimode ridge waveguides 100μm in width, 100μm thick and several millimeters in length. First, 100μm lines of ink spaced 75μm apart were deposited on a borosilicate glass slide. A layer of low viscosity, optically transparent epoxy Epo-Tek 301-1 was then deposited in the periodic reservoirs between the lines to form the incipient waveguides. The Epo-Tek 301-1 polymerized after standing and curing at room temperature for 24 hours. Cured Epo-Tek 301-1 adheres tenaciously to a wide range of substrates and

exhibits low shrinkage, so that the ink effectively acts as a mold. Epo-Tek 301-1 has an optical transparency of > 96% between 400nm and 1,600nm wavelengths. The last step in the fabrication of the epoxy waveguides is the removal of ink lines located between the epoxy guides. The stripping step was performed by placing samples in an oven or on a hot plate maintained at 65^{o}C. In effect, the fugitive ink is a positive resist. Figure 3.6(a) shows the top-view of the fabricated 100μm wide ridge waveguides spaced 75μm apart with a pencil tip as reference. Figure 3.6(b) shows a magnified top-view of a selected portion of the waveguides. Figure 3.6(c) shows multimode epoxy waveguides which conduct light from a blue (λpeak = 470nm) LED. Figure 3.6(d) shows cross-sectional view of the waveguides. In Figure 3.6(d) we notice a semi-circular structure to the side-walls for the waveguides. This structure is due to the cylindrical structure of the fugitive-ink lines. Figure 3.6(e) shows a magnified top-view of the waveguides that are transparent under intense optical illumination. This image will help in understanding the straightness and fabrication reproducibility of the waveguides. Figure 3.6(f) also shows the deposited xerogel between waveguides after aging for 5 days. Typically, the microstructures produced using the proposed direct-dispense technique are about 5-10% inaccurate depending on the dimensions of the targeted structures. This inaccuracy increases as the dimensions of the structures reduce to the system limit of 10μm. The structural variations are mainly due to ambient vibrations that affect the nano-manipulation system controlling the robotic deposition arm of the direct-dispense system.

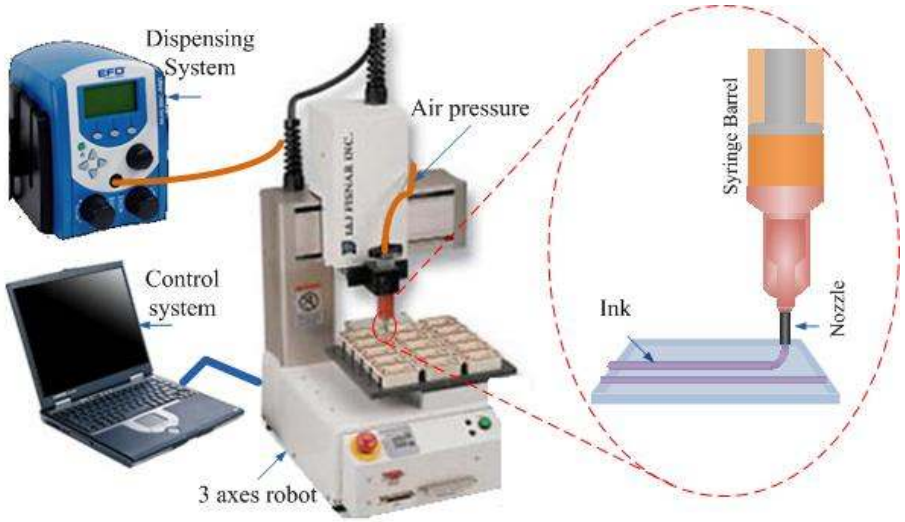

Figure 3-3: Direct-dispense microfabrication system.

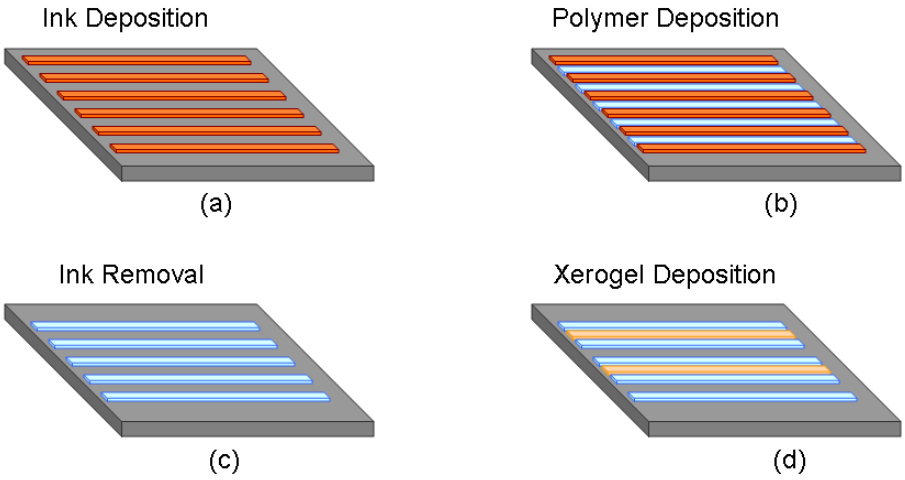

Figure 3-4: Fabrication process flow for the development of polymeric waveguide support platform using direct-dispense process and the immobilization of xerogel materials.

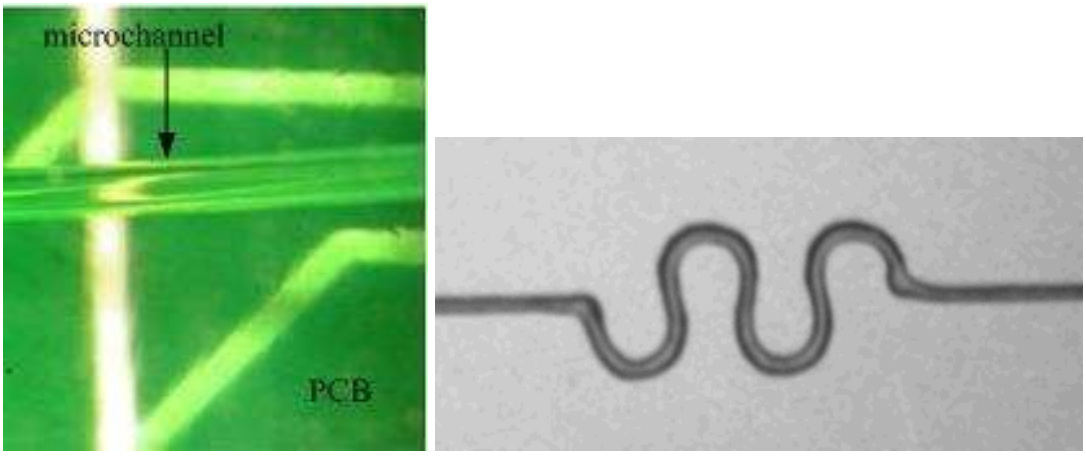

(a) **(b)**

Figure 3-5: Microstructures fabricated using direct-dispense technique. (a) Microscopic image of a fabricated 500 µm diameter microchannel on a Printed Circuit Board (PCB); (b) Serpentine microchannel with an inner diameter of 150 µm and 200 µm outer diameter.

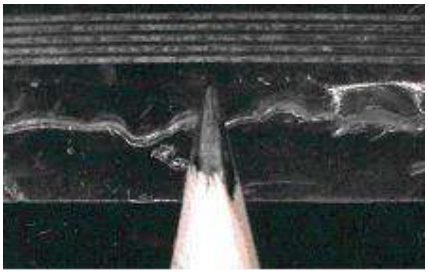

(a)

(b)

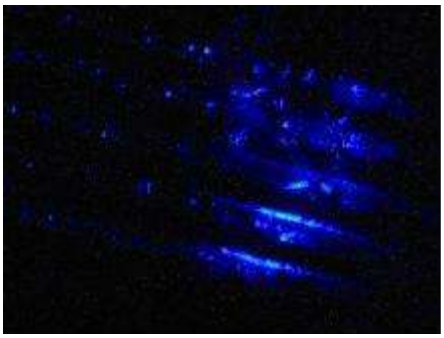

(c)

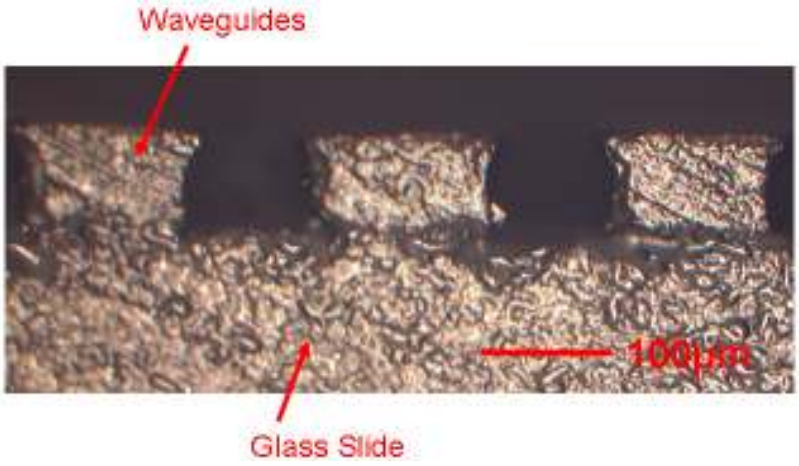
Waveguides
100µm
Glass Slide

(d)

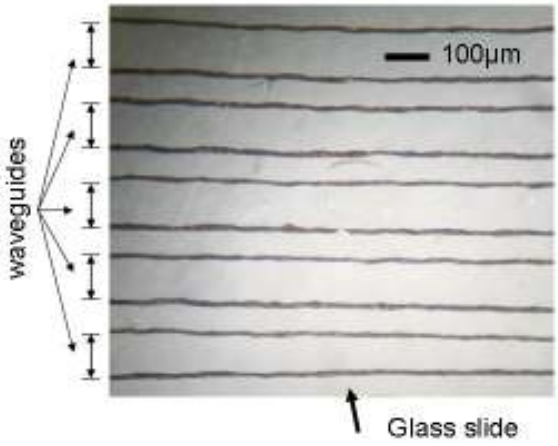
waveguides
100µm
Glass slide

(e)

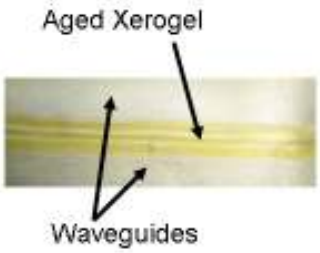
Aged Xerogel
Waveguides

(f)

Figure 3-6: Fabricated epoxy waveguides using the direct-dispense deposition technique. (a) Shows the top-view of the fabricated 100 µm wide ridge waveguides spaced 75 µm apart with a pencil tip as reference; (b) Magnified top-view of a selected portion of the waveguides; (c) Multimode epoxy waveguides which conduct light from a blue (λpeak = 470 nm) LED; (d) Cross-sectional view of the waveguides; (e) Magnified top-view of the transparent waveguides under intense optical illumination which shows the straightness and reproducibility of the structures; (f) Deposited xerogel after aging.

3.4 Xerogels Based Biochemical Sensor Arrays

In addition to the waveguide element for delivery and receiving optical signals, the xerogel sensing film is an important element of the array. Xerogels are micro-/nano-structured porous glasses that have been extensively researched for the development of sensors for various biochemical analytes including oxygen, glucose, pH, and lactate [161, 171, 173, 179]. The appeal of xerogels for biochemical recognition elements derives from their thermal stability, tunable pore dimensions and distributions, adjustable pH and dipolarity, a broad optical transparency window, and evidence that they can be used to sequester a wide variety of active agents like luminophores in their porous networks. In the area of xerogel based biochemical sensor arrays, Cho *et al*. [171] have explored pin-printing to create xerogel sensor arrays. Aubonnet *et al*. [175] introduced photopatterned waveguides for sensing, but the performance of the sensors was limited to the detection of gaseous samples because waveguide transmission losses were too large in sol-gel samples that readily hydrated. More recently, Burke *et al*. [176, 180] developed embossing techniques to create sol-gel waveguides. They used pin-printing to integrate xerogel materials with the waveguides. The direct-dispense microfabrication technique described here is comparable to sol-gel processing techniques for the waveguides development in terms of ease of fabrication and potential low cost. The use of direct-dispense technique for the waveguide microstructures can further improve the integration and functionality of sensor microsystems by combining the properties of gaseous/fluidic sample manipulation and sensing.

In addition to being an important neural biomarker, real-time monitoring of O_2 is important for blood gas analysis, water treatment, and food quality analysis. More than often, optical oxygen sensor systems are based on the measurement of luminescence intensity. Here, we prototype an O_2 sensor developed from the fugitive ink direct- dispense process. The detection scheme invokes fluorescence quenching of physically doped triplet $[Ru(bpy)_3]^{2+}$ [158, 170], whose quenching by oxygen has been quite well-studied [161, 171, 179]. Luminophore quenching in xerogel media is governed by many factors, and in the simplest scenario of a homogeneous distribution of luminophore molecules with a single exponential decay, luminescence quenching is described by the standard Stern-Volmer expression of Equation (1). In this expression, I_0 and τ_0 are the luminescence intensity and lifetime in the absence of analyte respectively, I is the luminescence intensity in the presence of analyte, K_{SV} is the Stern-Volmer constant, k_q is the bimolecular quenching constant and A is the fractional analyte concentration [170].

$$\frac{I_0}{I} = \frac{\tau_0}{\tau} = 1 + K_{SV}[A] = 1 + K_q \tau_0 [A] \quad (1)$$

It is recognized that physical doping and even covalent binding of the luminescent probe can give rise to heterogeneities in the local environment of the guest to cause nonlinear SV plots [181]. Two-site models, systematic changes in the host xerogel composition and more complex covalent attachment schemes have all been used to linearize and improve the SV response [182]. These strategies, desirable as they are, lie outside the scope of our current work which is not that of sensor optimization; instead our focus is to demonstrate functionality of a printable sensor array created by the fugitive ink direct- dispense technique.

3.4.1 Preparation of the Xerogel Oxygen (O2) Sensors

We prepared what is commonly referred to as a Class II hybrid xerogel. This material abandons the classic combinations of tetraethoxyorthosilicates (TEOS) and

tetramethoxyorthosilicates (TMOS) in favor of a silicon alkoxide component that is organically modified with a nonhydrolyzable covalent C-Si bond. Moreover, and anticipating future studies, the organic substituent can be a latently reactive moiety like a polymerizable monomer that can be further used to alter the properties of the host matrix (through crosslink density). Thus, the *sol* was prepared by acid catalyzed hydrolysis and polycondensation of 3-methacryloxypropyltrimethoxysilane (MAPTMS) in combination with methacrylic acid and ZrO2. Accordingly, MAPTMS (10.14 g, 0.040 mol) was combined with 0.05M hydrochloric acid (HCl, 0.54 g). The solution was stirred and aged for 1 hour at room temperature. During this time, a separate solution was prepared from 70% zirconium (IV) propoxide (6 g) in 1-propanol (0.013 mol) and methacrylic acid (1.1 g, 0.013 mol). These were combined and aged for 40 minutes. The methacrylic acid is incorporated to chelate Zr4+ in order to suppress the otherwise rapid hydrolysis that would deposit large particles of light scattering zirconia when the zirconium alkoxide is combined with the aqueous MAPTMS. After 1 hour, the MAPTMS solution is added drop-wise to the zirconium solution. The resulting *sol* is further hydrolyzed by the addition of distilled water (0.98 g) and stirred while being aged for at least 16 hours. The final ratio of water to silicon (r-value) is 1.5. The fluorescence sensor was prepared from a 1:4 mixture of 10 mmol/L *tris*(2,2'-bipyridyl) dichlororuthenium(II) hexahydrate in water and MAPTMS *sol*. 400 µL aliquots of [Ru(bpy)3]2+·6H2O were added to MAPTMS *sol* (1,400µL). Rapid *gel* formation was avoided by adding methanol (1 mL) containing water (200µL) to the final *sol*.

Prior to xerogel deposition, the waveguide samples were diced using a semiconductor-dicer to a length of 1 centimeter. The exposed glass substrate and epoxy waveguides were cleaned with isopropanol. The epoxy surface was first coated with the adhesion promoter, 3-aminopropyltriethoxy- silane (APTS). The APTS was dried at 50^{o}C for 2 hours. Once dry, the epoxy surface was again cleaned with isopropanol. Sol-gel sensing layer was subsequently deposited by direct-dispense in the spaces left by the stripped ink between two epoxy waveguide structures. The resulting structure of the sensor is shown in Figure 3.4(d). The hybrid glass was then dried for 1 hour at 50^{o}C

before a second layer was applied using the same procedure. The sensor waveguide structures were dried at 50^{o}C for five days.

3.5 Experimental Results and Discussion

The experimental setup for testing the proposed planar ridge waveguides is similar to the system shown in Figure 3.1. The setup consists of a blue LED (Digikey, λ peak: 470 nm) for exciting the xerogel coated waveguide structures on the glass slide. The LED is sinusoidally modulated at 400 Hz with peak-peak sinusoidal amplitude of 1 V and DC offset of 2.7 V. The resulting optical signal collected by the epoxy waveguides is passed through a long pass (Thorlabs: FGL590, λcut-off: 590 nm) optical filter to remove the excitation light and allow only the fluorescence emission to pass through. The fluorescence signal is detected by a standard silicon photodiode (Thorlabs: PDA100A) and the output of the photodiode is recorded by a lock-in amplifier (Stanford Research Systems, SRS830). Both the excitation LED and photodetector are placed as close as possible (less than 5 mm) to the waveguide structures to maximize the efficiency in the sensing process. The sensor response is measured as a function of gaseous O^2 concentration at room temperature (25^{o}C). The O_2 concentration is varied by changing its relative percentage with respect to gaseous N_2 concentration. The gases are mixed within a custom built gas mixing manifold, consisting of a matched pair of flow controllers (Cole-Parmer: EW-03229) connected to O_2 and N_2 gas cylinders.

As a prototype using the direct-dispense process, we fabricated a linear array of five polymer waveguides which housed two xerogel waveguides. As explained earlier, this configuration was used mainly for two reasons (i) xerogels are in aqueous form and hence two waveguide structures are used to contain the solution between them during deposition and (ii) the waveguide spacing between consecutive sensors is maintained in order to clearly distinguish the response from each sensor in the array. The sensor platform is scalable and can be used to implement large scale arrays for multi-sensor systems. As introduced earlier, the sensors operate on the basis of evanescent wave

sensing [8, 25]. In the prototype system we used a photodiode as the detector which can only measure the cumulative fluorescence response from the sensor array. Alternatively, using a Charge Coupled Device (CCD) camera as the detector would enable us to distinguish the response from each sensor in the array.

Figure 3.7 shows the response of the sensor as continually recorded by the lock-in-amplifier from the photodiode output by varying the oxygen concentration with respect to nitrogen gas. From the graph, we notice that the sensor system has repeatable performance with a response time on the order of 1 second. Measuring the exact response of the xerogel sensor material is difficult and the measured time is the experimental system response time which includes the time taken by the gas concentration to flow from the tanks through the controllers and tubing and fill the test chamber.

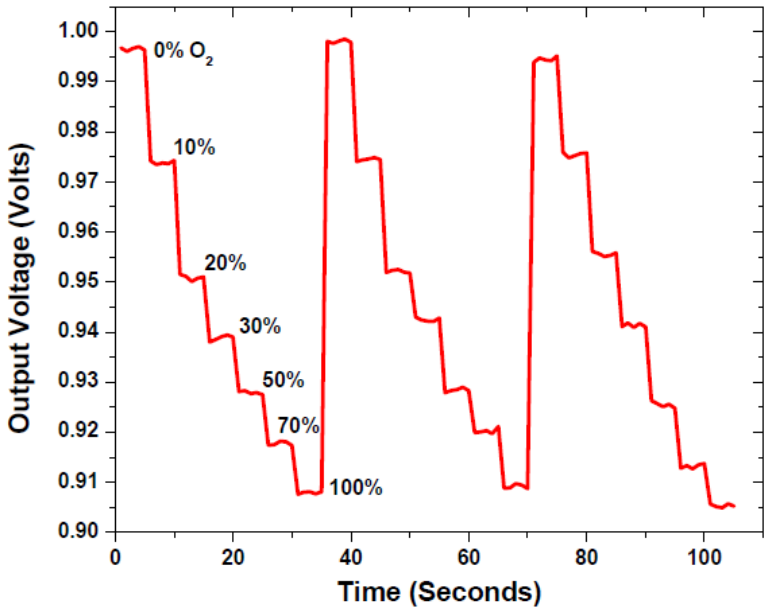

Figure 3-7: Response of the O2 responsive xerogel sensor materials.

Figure 3.8 shows the Stern-Volmer plot for the xerogel sensors. Each datum is the mean of results from five measurements. While the Stern-Volmer plot is nonlinear [28] for reasons discussed previously in Section 3, the data in Figures 3.7 and 3.8 show that the basic concept of the sensor array has been demonstrated. We notice that

the sensitivity of the sensor film is comparable to optical sensors that are based on printable technologies developed by other research groups [21, 22, 27]. However, the sensitivity is lower than sol-gel sensor materials that specifically aim for increased sensitivity [18, 30]. The xerogel formulation has been modified from traditional recipes (which are typically immobilized with dip coating or spin coating) to avoid rapid *gel* formation from *sol* state. This modification is a novel step that renders the xerogel immobilization compatible with direct-dispense fabrication process.

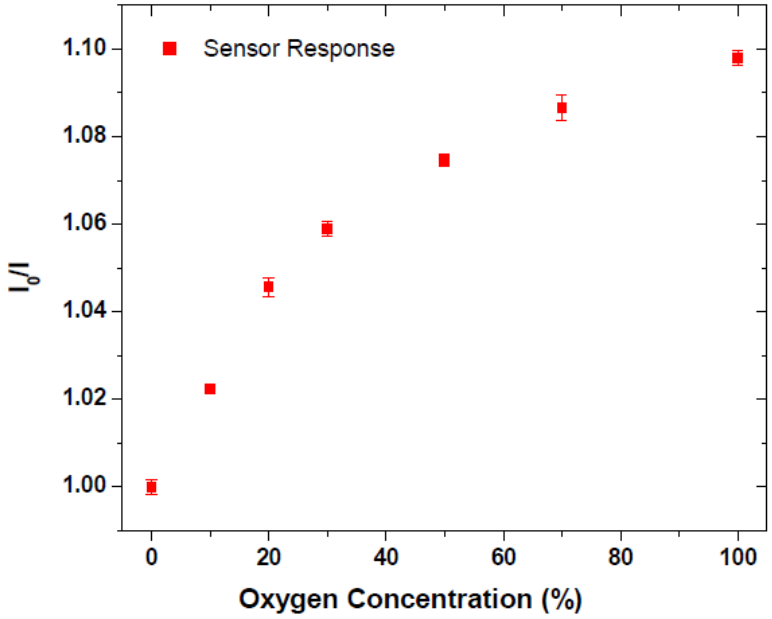

Figure 3-8: Stern-Volmer response of the xerogel O2 sensors.

3.6 Summary

This Chapter is based on the paper published by our group entitled "Direct-Dispense Polymeric Waveguide Platform for Optical Chemical Sensors" Sensors,vol. 8, pp. 7636-7648, 2008. The xerogel used in this paper was prepared by Timothy Gonzalez and Hagop Djeghelian. Ebrahim Ghafar-Zadeh helped in setting up the direct dispense robotic system. We have described the implementation of direct-dispense patterning to develop polymeric waveguide support platform for optical multi-sensor systems. Specifically, we demonstrated a waveguide array structure made with direct-dispense

to support sol-gel derived xerogel recognition materials which are made responsive to oxygen concentration. The direct-dispense fabrication process suggests a scalable, versatile, cost-effective technology towards printable optical sensor arrays.

The direct-dispense process may in the future lead to a high-performance, multi-functional sensor platform that can support gaseous/fluidic sample handling and optical signal collection and transmission. Advantages of this technique as compared to other soft-microfabrication techniques, are that one needs only a single direct-dispense setup (no requirement for combining multiple fabrication strategies or the creation of micro-contact printing masters), and ability to develop structures on–the-fly. The developed xerogel sensors performed for the full-scale range (0%-100%) of gaseous oxygen concentration with a response time of less than 1 second. The sensors show comparable sensitivity to other competent optical chemical sensors based on printable and patternable technologies. These findings suggest a bright outlook for miniaturized multi-sensor platforms by direct-dispense.

In this thesis, we employ this robotic dispensing technique to write optical biochemical sensors on silicon neural electrodes to locally monitor brain tissue oxygenation. A rectangular cavity is etched in the silicon microelectrode. Fugitive ink is employed as sacrificial layer in the area dedicated to the xerogel sensor materials. The polymeric ridge waveguide sensors are then written in the remaining part of the cavity. Finally, the fugitive ink is removed to deposit the xerogel sensor materials which are in direct contact with the endface of the ridge waveguide.

CHAPTER 4

HYBRID NEURAL PROBES

Recording the electrical activity of the brain has dominated neuroscience for several decades [10, 60]. However, it is widely accepted that brain contains many other signal sources that can elucidate the nature of information flow and function [60]. For example, functional Magnetic Resonance Imaging (fMRI) relies on the de-oxygenation of hemoglobin to infer the activity (or its absence) in a cortical area. In contrast to oxygenated hemoglobin, deoxygenated hemoglobin disrupts the magnetic field which would lead to an enhancement of the MRI. Thus, this technique infers activation by measuring the changing oxygen concentration in a region. Although the causal relationship between neural activity and deoxygenation measurements is still under debate [183], the use of fMRI has gained wide acceptance and experiments using this method have contributed to many novel theories of brain function.

Several researches have reported that oxygen (O_2) concentration ascribed to immediate oxygen consumption can be observed 100 milliseconds after activity onset [184-185]. Thus, hemodynamic events are tightly coupled to cortical electrical activity immediately following activation. O_2 pressure changes have also been shown to be highly specific for local increases in neuronal activity and are correlated with the degree of activity [186]. Local (invasive) O_2 measurements have been used to predict the nature of visual stimuli suggesting the presence of decoding power in the O_2 responses, a finding that has proven useful for prosthetic applications [187]. Thus, to benefit from the link between hemodynamics and neural activity, the development of an integrated platform to hold O_2 and other biomarkers' sensors along with electropotential recording sites to measure the neural electrical activity has become indispensable.

There have been previous implementations of amperometric-based sensors, which employs electrical recording sites, that targeted simultaneous measurement of brain tissue oxygenation and neural activity [188]. These probes were only 6mm long and their fabrication process is quite complicated which would limit development of ultra-long probes [188]. It is also possible that other electroactive species present in the brain and in the media surrounding the electrodes could affect the amperometric oxygen sensor response. Biofouling due to brains immunological response on the cathode may limit the life of the sensor. Finally, the requirement for large external reference electrode limits the size of the electrode array design for implantable devices.

To address these technological challenges, we present in the current chapter the integration of optical oxygen sensor with the elongated electrodes as described in chapter 2. The O_2 sensors are made using sol-gel derived xerogel thin films that encapsulate O_2 responsive luminophores in their nanostructured pores. As a prototype, we demonstrate embedding optical fiber coated with oxygen-responsive xerogel on the neural microelectrodes. The O_2 responsive sensors are based on encapsulating the luminophore, tris(4,7'-diphenyl-1-10'-phenathroline) ruthenium(II) chloride pentahydrate ($[Ru(dpp)_3]Cl_2.5H_2O$) in the xerogel nano-/micro-porous matrices.
We hypothesize that additional signals recorded by the multimodal probes will increase the information yield when compared to standard probes than those that record only electropotentials. The recording of neural biomarkers along with electrical activity could help the development of intelligent and more user-friendly neural prosthesis/brain machine interfaces as well as aid in providing answers to complex brain diseases and disorders.

4.1 Design and Fabrication of the Hybrid Neural Microelectrodes

Neural probes are microdevices that form the connection between the biological neural tissue with external devices and electronic systems. Typically, a neural probe consists of a single or multiple long protruding structures or electrodes that have

preferably thin thickness. Ideally, electrodes with minimum thickness are preferred to reduce damage to the tissue when the probe is inserted into the brain. In contrast, the electrode has to be wide enough to hold many recording sites precisely placed to measure neural electrical activity at different desired depths.

In addition, the probes should incorporate sufficient mechanical strength to survive the compression and tensile forces during the insertion and retraction phases respectively while implantation into the brain. NeuroMEMS, or silicon-based neural probes allow the fabrication of long, miniaturized and well defined probes carrying accurately distributed and spaced recording sites thus fulfilling the requirements mentioned above [189]. Here, we employ silicon micromachining techniques to fabricate a novel multimodal neural probe capable of simultaneously monitoring neural electropotentials and biomarkers. Figure 4.1 shows the schematic representation of the proposed probe. The electrical signal recording part of a silicon probe array consists of a single or multiple long protruding tapered silicon electrodes. Each neural probe can contain multiple metallic recording sites to record brain electrical activity, interconnect traces, and back carrier area carrying the bonding pads to connect the probes to external electronics. The optical biological and chemical sensing part of the probe consists of nanostructured material doped with analyte-specific recognition elements. As explained earlier, we focus on oxygen sensors as a prototype system due to its extensive correlation with brain functioning and neural information. The oxygen sensors are based on quenchometric sensing and use sol-gel derived xerogel thin-films as host media to reliably encapsulate the luminophore $[Ru(dpp)_3]^{2+}$ molecules during the sensor operation. Xerogels are nano-/micro- porous glasses and their appeal for biorecognition elements derives from their thermal stability, tunable pore dimensions and distributions, biocompatibility, and a broad optical transparency window [179]. We employ a novel strategy to immobilize the xerogel sensors inside the neural electrode array. These sensor materials are coated at the end of an optical waveguide structure or at the tip of an exposed core of an optical fiber embedded inside the silicon microelectrode array. The optical waveguides allow sending and receiving optical signals from the xerogel biochemical sensors.

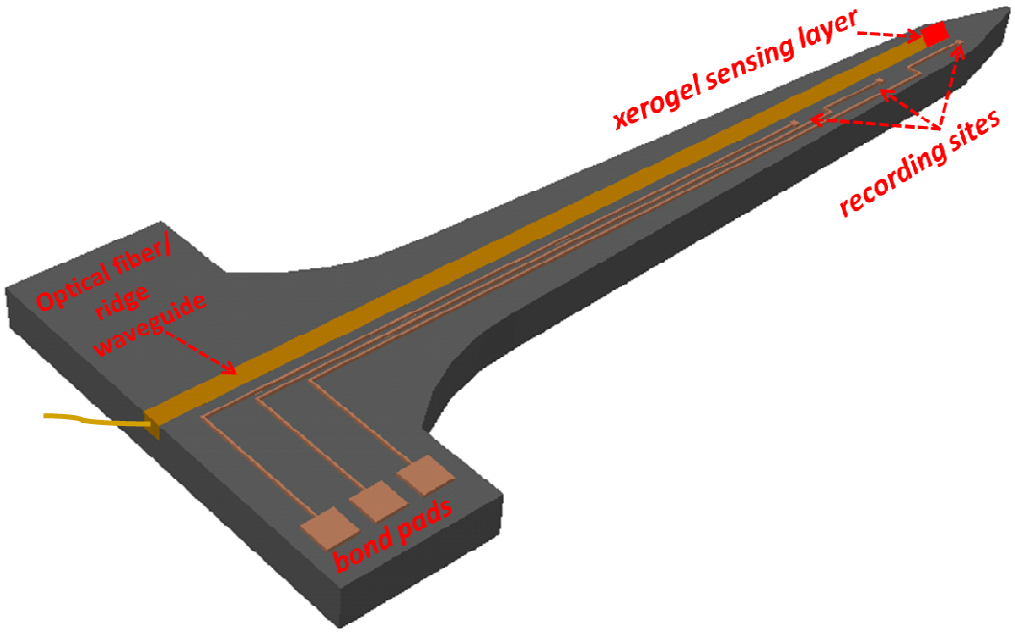

Figure 4-1: Design of the multimodal neural microelectrode with integrated electro-potential recording and optical sensor waveguiding structures.

Each electrode is 10.5 mm long and 75 µm thick and is divided into three regions which are a 250 µm long tapered support base region, a 10 mm long measuring region, and finally a 250µm long piercing region. The tapered 250 µm wide base is designed to provide sufficient strength for each probe to survive during surgical implantation. The measuring region, which continuously reduces in width along the length of the electrode to minimize brain tissue damage, can hold many 10µmx10µm gold recording sites in order to measure neural activities at different depths. The piercing region forms the chisel-shaped tip of the electrode which penetrates the brain tissue and facilitates the insertion of the rest of the electrode. The distance between the two neighboring shafts is 350 µm.

The microfabrication process of the electrode array starts with a 75-µm-thick 4" diameter double side polished silicon wafer (boron doped, resistivity of 20 ohm-cm and <100> oriented) which is diced into small square pieces by using a dicing saw as shown in Figure 4.2(a). Then, metal layers of titanium (adhesion layer, 500 nm thick) and gold (conducting layer, 750nm thick) were deposited by sputtering on the silicon wafer. The gold and titanium layers were photolithographically patterned and wet

etched, with solutions of 1:2:10 I_2:KI:H_2O and 20:1:1 H_2O:HF:H_2O_2, respectively, to define the recording pads, interconnects between the recording sites, and bonding pads as depicted in Figure 4.2(b). A 25μm deep rectangular cavity is then etched in the silicon electrode as illustrated in Figure 4.2(c). The cavity and the recording site are 100μm spaced apart.

The whole sample is then coated with parylene-C, a biocompatible material widely used for coating a wide variety of implantable biomedical devices such as pacemakers and metal-wire neural probes. A 2μm thick layer of parylene-C is conformably deposited at room temperature using a chemical vapor deposition (CVD) system. Openings to expose the recording sites, to measure the neural electrical activities, and the bonding pads, to be wire-bonded to a printed circuit board (PCB), were defined with photolithography as depicted in Figure 4.2(d). The exposed parylene-C is etched with oxygen plasma ashing system (Model: 200, PVA TePla Inc.), in which reactive species combine with the parylene-C to form ash which is removed under vacuum.

The silicon substrate was then photolithography patterned and etched using isotropic xenon difluoride (XeF_2) dry etching system to form the electrodes as illustrated in Figure 4.2(e). The optical biochemical sensors were prepared by etching the cladding of an optical fiber and exposing the core. This latter was etched down to 25μm. The core was then cleaned with acetone and coated with the oxygen sensor and was aged for 5 days at ambient room conditions before experimental testing. Finally, the optical fiber was then embedded inside the etched cavity. In this configuration, the core is used to transit optical excitation and fluorescence signals. This configuration allows maintaining the same electrode thickness, thus, minimizing the damage to brain tissues and at the same time protect the brittle xerogel thin-film sensor materials from rupturing during implantation into the brain tissue.

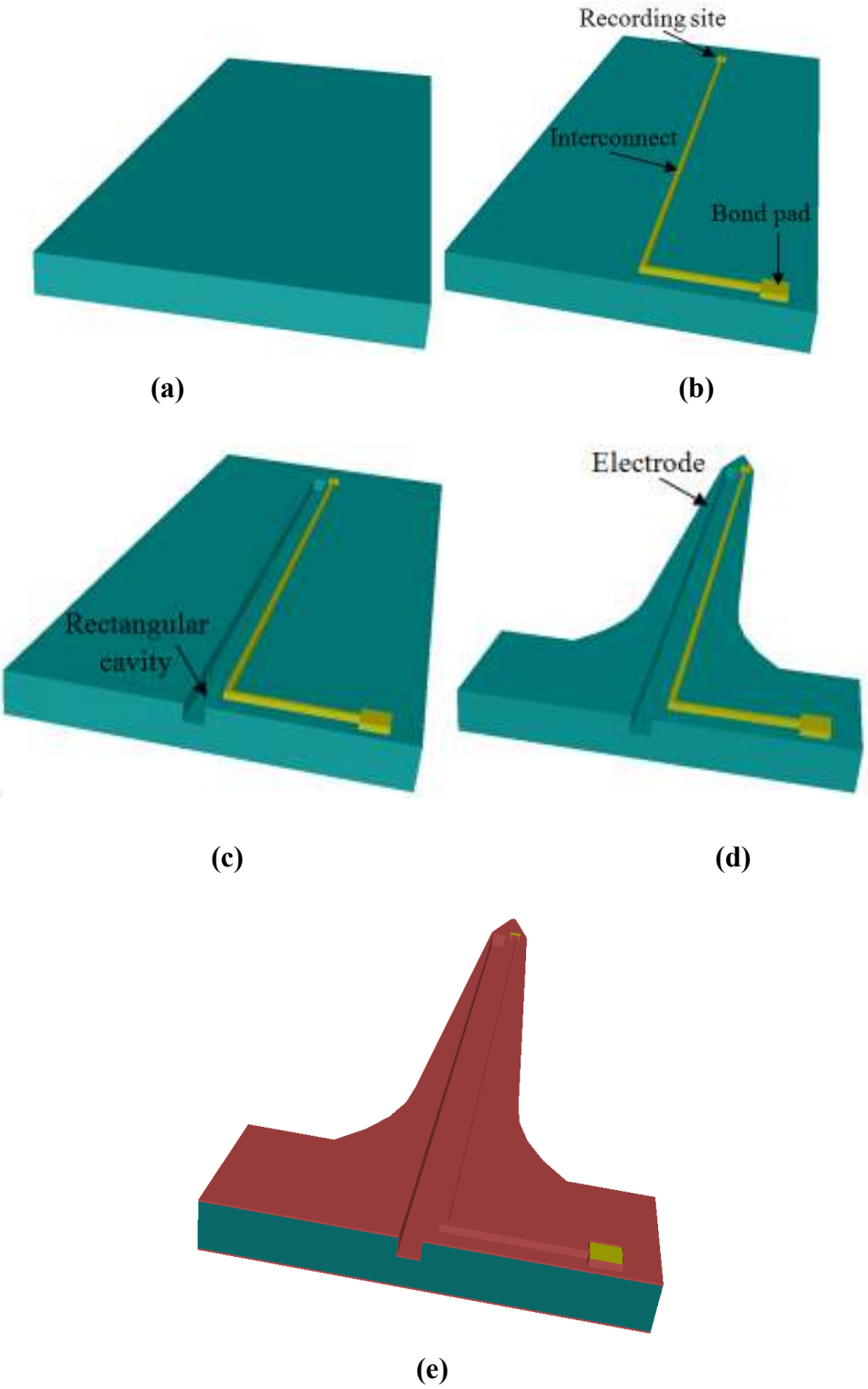

Figure 4-2: Fabrication process of the hybrid neural probe. (a) Dicing of silicon substrate; (b) Patterning of the metal layer to form the recording sites; (c) Etching of a rectangular cavity; (d) Patterning of the silicon substrate to form the neural electrode; (e) Deposition, patterning, and etching of Parylene C to expose the recording site and the bonding pad.

Figure 4.3(a) is a photomicrograph for the complete fabricated multimodal array which consists of two hybrid electrodes. Figure 4.3(b) is close-up view of the probe electrodes with etched rectangular cavities hosting the exposed cores of optical fibres. Figure 4.3(c) is a microscope image for one of the probe electrodes that clearly shows the tip combining the titanium-gold recording site and the etched cavity with well-defined structures of the silicon electrodes. A hybrid neural probe electrode can integrate many optical fibers to monitor brain tissue oxygenation at different depths in the brain. The scanning electron microscopy (SEM) image in Figure 4.3(d) shows two cavities with endfaces spaced 1mm apart and neighboring two recording sites. Figure 4.3(e) is a magnified view of one recording site neighboring an etched cavity. The bonding pads used to connect the recording sites to external circuitry are shown in Figure 4.3(f).

The recording site impedance is critical in the design of neural probes and is dominated by the size of the site opening. Impedance values are obtained by recording the current while submersing the probe electrodes in saline solution and passing current through them. The impedance was measured at 1 KHz and was found to be 540 KΩ, a suitable impedance to record single neuron activity and local field potentials (LFPs).

(a)

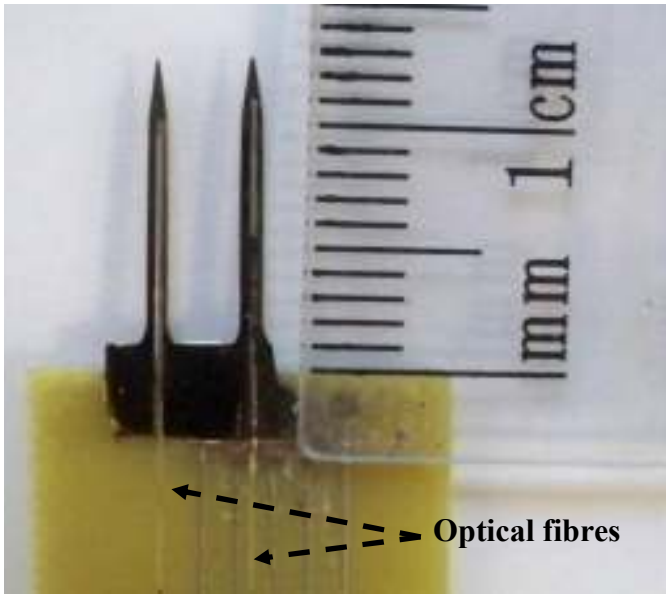
mm 1 cm
Optical fibres

(b)

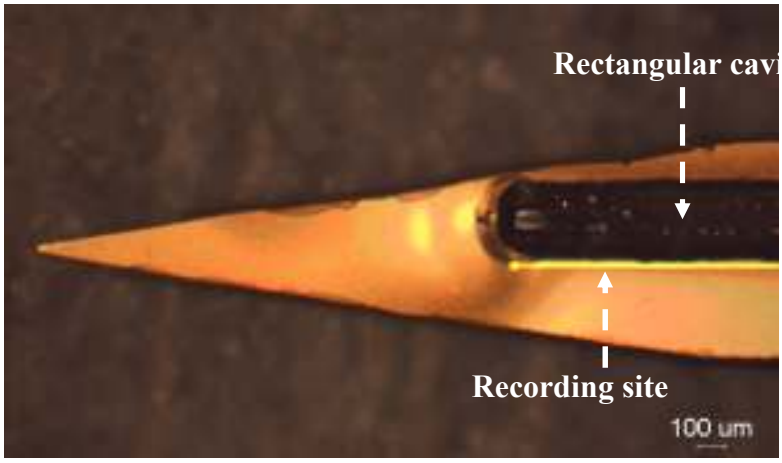
Rectangular cavi
Recording site
100 um

(c)

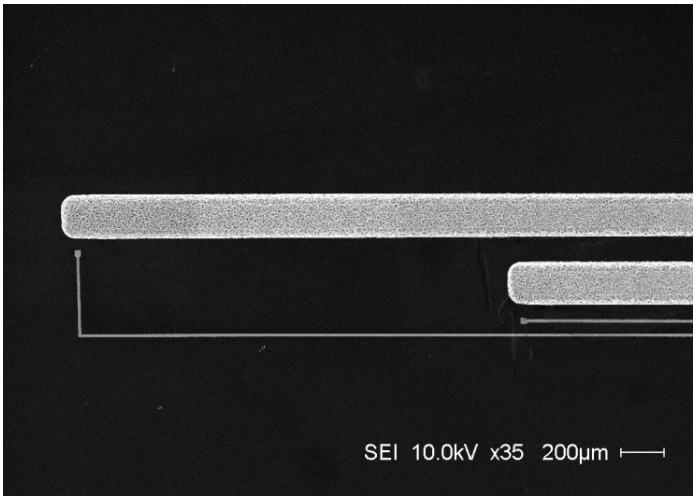
SEI 10.0kV x35 200µm

(d)

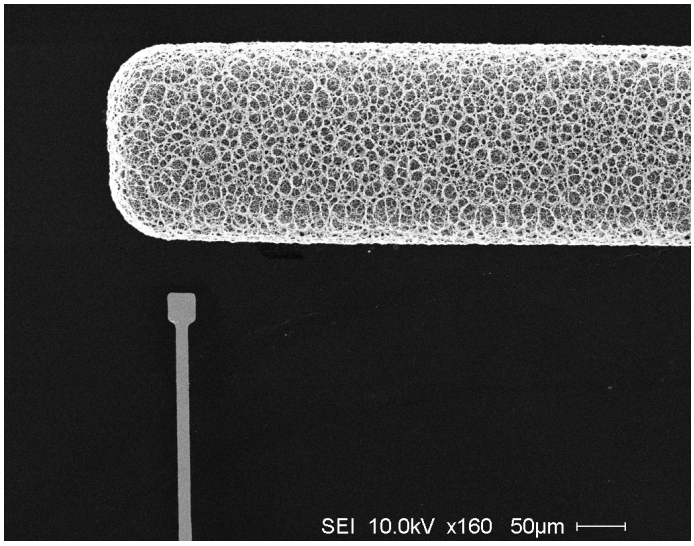

(e)

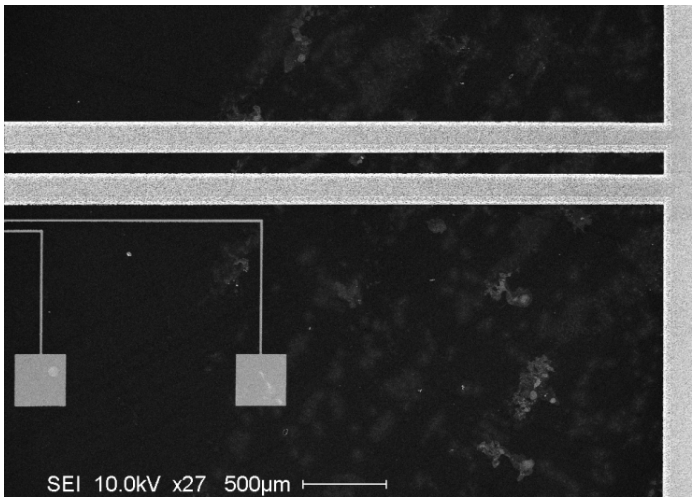

(f)

Figure 4-3: Microscope images of the fabricated hybrid multimodal neural probe (a) The 2-electrode hybrid neural array; (b) Close-up image of the probe electrodes; (c) Magnified view of the electro-potential recording site and the cavity hosting the optical sensors; (d) SEM image showing two cavities with enfaces spaced 1mm apart and neighboring two recording sites on the same neural electrode; (e) Magnified view of one recording site and an etched cavity; (f) SEM image showing two etched cavities and two bonding pads.

The current elongated neural electrodes can be made sturdier and more resistant to cracking and shattering by significant reinforcement of the electrodes at the middle to withstand the insertion axial forces, retraction forces, and tension forces of the brain

tissue that act upon the electrode probe during implantation. The reinforcement can be obtained, for example, by taking benefit of the metal layers used to form the recording sites, interconnect traces, and bonding pads to add reinforcing structures the middle of the electrodes [190-191].

4.2 Preparation of Xerogel Based Oxygen Sensor

Luminescence based sensors are widely used in medical and biomedical applications [157-158]. The monitoring of oxygen is based on the well-established quenching of the luminophore $[Ru(dpp)_3]^{2+}$ which is widely used in the development of optical oxygen sensors [192-193]. The sensor operates on the basis of evanescent wave sensing which is a well established principle for optical fiber and waveguide based sensors [178]. In these types of sensors, the excitation light leaks through the waveguide structures in the form of an exponentially decaying evanescent field and activates the fluorophores entrapped in the xerogel coatings. Subsequently, the luminophores fluoresce with intensity proportional to the target analyte concentration. A part of this generated fluorescence is guided back into the waveguide and is detected by a photodetector.

The following reagents were used to prepare the xerogel based oxygen (O_2) sensors: tris(4,7'-diphenyl-1-10'-phenathroline) ruthenium(II) chloride pentahydrate ($[Ru(dpp)_3]Cl_2.5H_2O$) (GFS Chemicals); tetraethoxysilane (TEOS), and -octyltriethoxysilane (C8-TEOS); HCl (Fisher Scientific); and ethanol (EtOH) (Quantum Chemical). $[Ru(dpp)_3]^{2+}$ is purified as described in the literature [30]. All other reagents are used as received. All aqueous solutions are prepared with deionized water that has been treated with a Barnstead NANOpure II system to a specific resistivity of 17.7M . cm.

The sol stock solution is prepared by physically mixing 0.513 mL of C8-TEOS, 0.362 mL of TEOS, 0.625 mL of EtOH, and 0.200 mL of 0.1-M HCl in deionized water. The stock solution is sonicated for 1 h under ambient conditions. To fabricate the -responsive sensor films an 80μL aliquot of the stock solution is physically mixed with

a 20 µL aliquot of 12.5 mM $[Ru(dpp)_3]^{2+}$/EtOH. The optical fiber was then dipped in 80 µL aliquot of this doped sol mixture for coating. The resulting sensor film is allowed to age in the dark at room temperature for ten days before testing.

4.3 *In-Vivo* Recording

The sensor was tested in area 5 in the parietal cortex of a nonhuman primate. The sensor was housed in a spinal needle and lowered until it was 1mm beneath the *dura*. All procedures were approved by the McGill University Animal Care Committee and were also in compliance with the guidelines of the Canadian Council on Animal Care.

Figure 4.4 shows the mean of 20 traces of the O_2 response (mean ± SE) recorded with our sensor. The red trace is the percent O_2 change recorded while the monkey was engaged in a reaching task while the blue trace represents the percent change when the animal was resting. The percent change was calculated by extracting 4 seconds of O_2 response starting at the beginning of a reach trial (red) or at a time in the O_2 response where the animal rested for at least 4 seconds. The mean of the preceding 2 seconds of data for each trial was subtracted from the corresponding 4 second time interval and the resultant trials averaged (n=20). This mean was then normalized by the mean of all trials [186] and smoothed using a Savitzky-Golay filter of order 2 and length 50. The reach trials started when the monkey reached for and maintained contact with a central target on an acoustic touch screen. After 500ms, a light was flashed somewhere on the touch screen for 300ms. This flash indicated the location of the impending reach. The monkey had to then wait for an instruction to reach towards the flash. After an average time of 1300ms, the central target was extinguished instructing the monkey to reach towards the remembered location of the flash. Monkeys initiated the reach shortly thereafter (mean ± standard deviation: reaction time = 324 ± 110 ms, movement time = 100 ± 9ms). Monkeys were rewarded if they reached accurately towards the target and held contact with the screen for 700 ms. As can be seen from the red trace, consumption of O_2 occurred during the time that the monkeys were

moving and the target was being flashed. The opposite trend is observed when they were waiting for the instruction to reach.

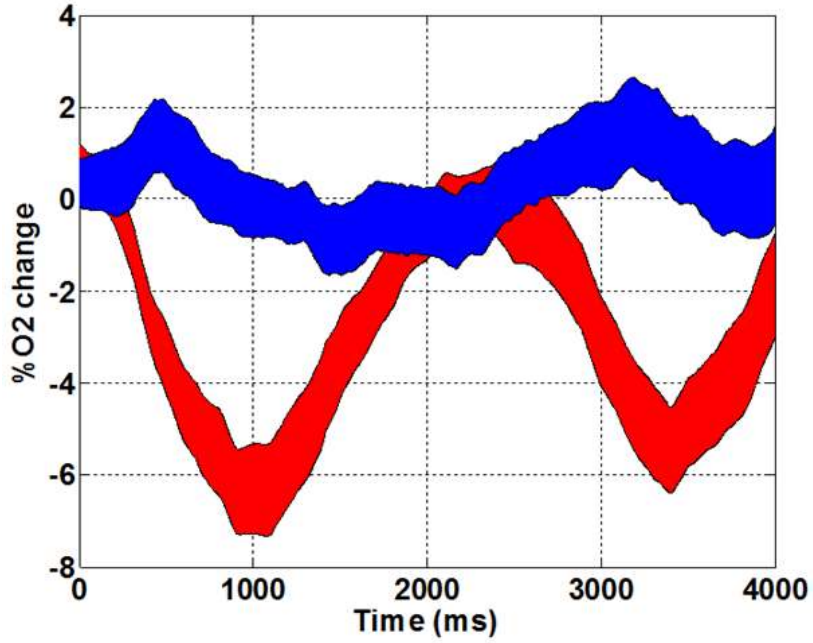

Figure 4-4: Measurement of the O_2 variation in area 5 in the parietal cortex of a nonhuman primate using O_2 responsive xerogel sensor.

4.4 Summary

We described a novel methodology of integrating optical chemical sensors with neural electro-potential recording microelectrodes. We employed xerogel doped with ruthenium complex which is responsive to O_2 concentration to monitor brain tissue oxygenation. We described the fabrication of elongated multi-modal multi-site neural microelectrodes that can reach lengths up to 10mm while having only 75µm thickness. Xerogel based oxygen sensors are deposited on the core of an optical fiber to serve as integrated sensor waveguides. Experimental evaluation of these multi-modal neural electrodes was performed in area 5 in the parietal cortex of a non-human primate.

CHAPTER 5

BIOCOMPATIBLE INTERFACE: POROUS SILICON

Interfacing between biological systems and electronic system poses the major challenge for scientists in this area. A biocompatible interface possesses the ability to contact with a biological system without provoking a natural response. The human body typically responds to contact with synthetic materials by depositing proteins and cells from body fluids at the surface of the materials. This can cause infection and biological rejection of devices built from non-compatible materials.

Biomedical devices built from bulk silicon have been available for in vitro biosensing applications for several years. However, this form of silicon is not biocompatible and so far this has prevented its use in vivo. Bulk silicon-based devices need coating or packaging in a biocompatible material, if they are to be used in and linked to living tissues. The majority of today's medical devices are coated with materials such as Polyvinylchloride (PVC), polypropylene, polycarbonate, fluorinated plastics and stainless steel. These materials are tolerated by the human body and are described as bioinert. An effective biomaterial, however, must bond to living tissue and is known to bioactive.

Nanostructured porous silicon (PS) has properties that make it a very promising bioactive biomaterial, in particular for sensing devices that need to be linked to the biological system such as the neural probes.

The particular texture of porous silicon which can be described as a network of pores interconnected by solid nanocrystalline silicon, grants bulk single crystalline silicon additional electronic and optical properties [194-195]. Porous silicon was introduced in optical applications when red-light photoluminescence was reported from the

material [196-197]. Porous silicon layers have a very high surface to volume ratio and typically are a few microns thick [198]. Multilayer stacks of porous silicon can be designed to match the desired optical behavior, since changes in the reflection and transmission spectra would depend on variations induced in the effective index of refraction by the silicon porosity [199-200]. Porous silicon material is useful and attractive for a wide variety of applications to develop humidity, pressure, and vapor sensors [201], chemical sensors [202-204], biological sensors [205-207], biomedical devices [208-209], and photonic devices [206, 210-211].

An essential requirement for fabricating porous silicon in different applications is to have the ability to vary the size and configuration of the pores by choosing the appropriate fabrication parameters and conditions. For instance, for photonic bandgap filters, the pores are designed to the on the order of the wavelength of the light to retain and tune the optical reflectivity of the porous silicon [212-213]. For biological sample filters, the pore size has to be large enough to allow the desired biomolecules to be filtered and cross through the pores freely [214].

The applications of porous silicon in different areas have significantly increased the interest in researches focused on this specific biomaterial. In this chapter, in-vitro study was carried out wherein mesenchymal stem cell derived from bone marrow of Pthrp mice are plated on porous silicon samples fabricated using Xenon Difluoride (XeF_2) dry etching technique. This is to demonstrate the biocompatible characteristic of porous silicon by its ability to promote stable environment for growth and proliferation of mesenchymal stem cell (MSC).

The mice chosen are wild type for the parathyroid hormone related protein gene, and therefore they have a normal chondrocyte metabolism and cartilage development. Indeed, to initially observe the proliferation and growth of MSC on porous silicon, wild type mice would be the best model. Moreover, a few experiments have been preformed plating Pthrp mesenchymal stem cell on titanium disks, which demonstrated that it provides a suitable platform for the growth of cells. In this study,

apart from plating cells onto the porous silicon, the titanium disks were also used as controls apart from the tissue culture plastic.

Here, we investigate the growth and proliferation of bone marrow derived mesenchymal stem cell on un-etched silicon and on porous silicon samples etched to different depths of 20μm and 30μm. We hypothesize that porous silicon is an ideal biomaterial for the growth of the MSC. On Alamar Blue assay, we expect to see higher metabolism rate as the time points increases due to an increase in cell numbers. On SEM we are expecting to observe cells adhered inside the pores of the porous silicon.

5.1 Fabrication of Porous Silicon

Many previous reports have shown that porous silicon can be prepared through a galvanostatic, chemical, and photochemical etching procedures in the presence of hydrofluoric (HF) acid solutions or through stain etching [198, 215-216]. Other methods such as pulsed anodic etching [217] and by magnetic-field assisted anodization [218] were also employed for porous silicon preparation. In these techniques, the pore characteristics such as diameter, geometric shape and direction of the pores not only depend on the composition of the etching solution, but they also depend on temperature, current density, crystal orientation, dopant and doping density of the silicon substrate [195, 198, 216]. In this chapter, we present a novel and simple fabrication technique which employs Xenon Difluoride (XeF2) based dry isotropic etching to selectively form porous silicon in bulk single crystal silicon wafers.

XeF_2 is plasma-less etching technique and is based on the reaction of the fluorine ions, which represents the main etchant, with the solid silicon to produce the volatile gas SiF_4 at room temperature.In XeF_2 based etching process a standard hard baked layer of photoresist can serve as a masking layer. In addition to its etching process simplicity, XeF_2 has high etch selectivity to silicon. It reacts readily with silicon, but

is relatively inert to photoresist, silicon dioxide, silicon nitride and aluminum, which allows this technique to be used in the presence of CMOS integrated circuits as a post processing step. This is not the case when HF based etching is used, as this latter will etch or damage the circuitry without a very hard mask followed by complex post-processing to remove the mask.

In the current chapter, we present the fabrication process of the porous silicon and discuss the parameters that affect the texture of the porous silicon. Detailed characteristics such as the pore size, the thickness, and the porosity of the fabricated porous silicon are studied using top and cross-sectional images from scanning electron microscopy and optical reflectance measurements.

5.2 Fabrication of Porous Silicon Using XEF_2

XeF_2 is widely known as a dry isotropic etching mechanism for silicon micromachining [219-221]. The XeF_2 etching system (Model: Xetch E1, Xactic Inc.) consists of a source bottle of XeF_2 which is a dense white crystalline solid with a room temperature vapor pressure of roughly 4 Torr reached by a vacuum pump, an expansion chamber, and an etching chamber as shown in Figure 5.1. The etching chamber is provided with XeF_2 during a sequence of short time periods separated by evacuations. Diced silicon wafer pieces or a full wafer is loaded in the etching chamber and placed horizontally with the side to be textured by XeF_2 facing up. The etching chamber is then placed under vacuum. Once the pressure reaches 3×10^{-2} mbar, the etching process begins. The etching process is based on cycles. Each cycle includes the flow of XeF_2 from the source bottle into the expansion chamber, and then from the expansion chamber to the etching chamber. The etched thickness depends on the number of cycles. Once the etching process is completed, the etching chamber is vented and there is no need for drying which is a critical step in the wet electrochemical fabrication process of porous silicon. Without post-fabrication drying with a wet etch solution, the risk of damaging the newly formed porous silicon is greatly reduced.

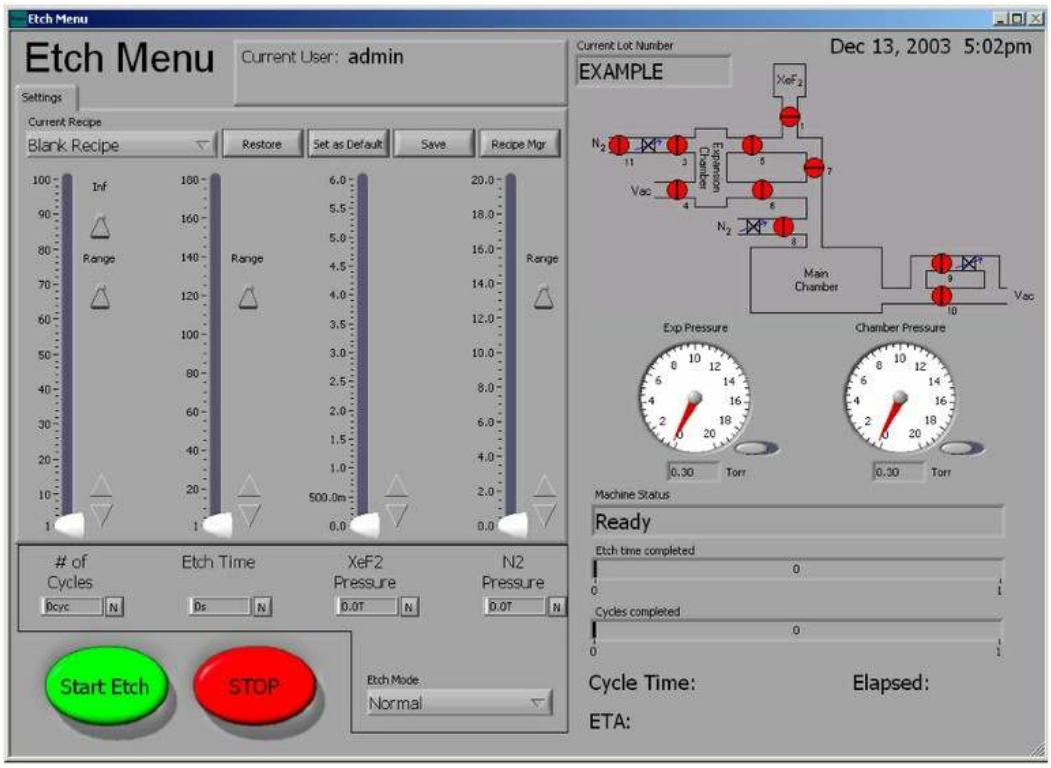

Figure 5-1: Etch menu features

The etching mechanism of silicon with XeF_2 follows through a sequence of steps [219, 222-223]. First, undissociated gaseous XeF_2 is absorbed on the exposed areas of solid silicon. Second, the adsorbed gas is dissociated to xenon and fluorine. Third, the fluorine ions react with silicon to produce an adsorbed layer of SiF_4, which finally disassociates into a gas phase. The chemical reaction for the etching of Si by XeF_2 is given below,

$$Si + 2XeF_2 \rightarrow SiF_4 + 2Xe \qquad (1)$$

The silicon wafers used in the following experiments to form porous silicon were 3 inch 381±20µm thick <100> boron-doped (5–10 ohm-cm) silicon wafers. The wafer was cut into 2cm x 2cm squared pieces using a dicing saw machine. A 1.4µm thick layer of photoresist was spin coated and photolithographically patterned to expose a squared window (1cm x 1cm) in each silicon wafer piece. Because of the high selectivity of the XeF_2 etch technique, the silicon samples were dipped in a diluted

H_2O: HF solution with a ratio of 10:1 for 3 seconds to remove the native oxide which would prevent the XeF_2 from etching the silicon underneath. The samples were then dried with flow of nitrogen and immediately loaded in the transparent etching chamber of the XeF_2 system. One sample was etched at a time. Before and after each etching, the complete vacuum system was purged with nitrogen many times to remove any residual gases. The samples undergo a time-based etching of the exposed silicon leaving behind a porous silicon layer in the exposed silicon region. Finally, the hardbaked photoresist layer was removed using an oxygen plasma ashing system (Model: 200, PVA TePla Inc.), in which reactive species combine with the photoresist to form ash which is removed under vacuum.

The morphology of the pore network was imaged using a Scanning Electron Microscope (SEM). Figures 5.2(a), (b), and (c) are SEM images for three porous silicon samples that were etched to different depths of 10 µm (sample A), 20 µm (sample B), and 30µm (sample C) into the silicon wafer respectively. The samples have the same 1.3cm x 1.3cm exposed area and were etched under the same conditions with different number of cycles. The etch depths were measured using an Ambios surface profilometer employing a diamond-tipped stylus. Data was recorded at a frequency of 50 Hz with a scan rate of 10 μm-s^{-1} which corresponds to a scan resolution of 0.5 μm. The reported etch depth is the average depth measured across the entire width of the trench.

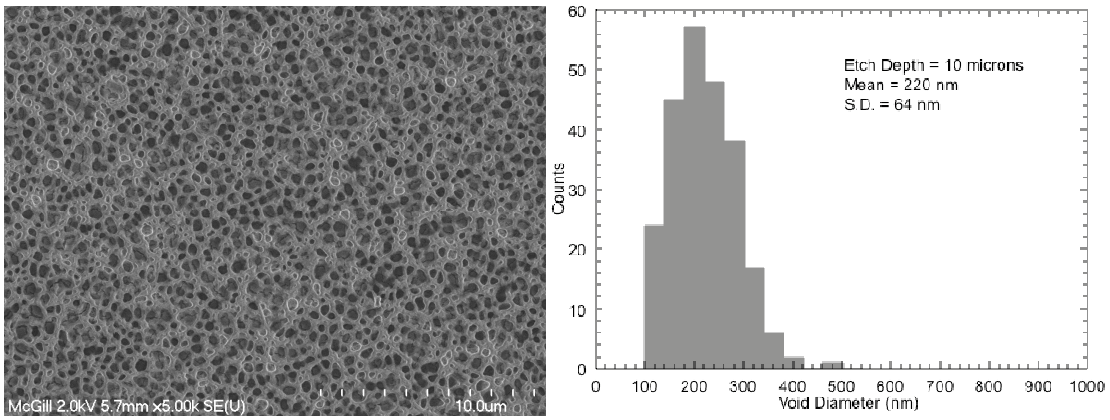

(a) **(b)**

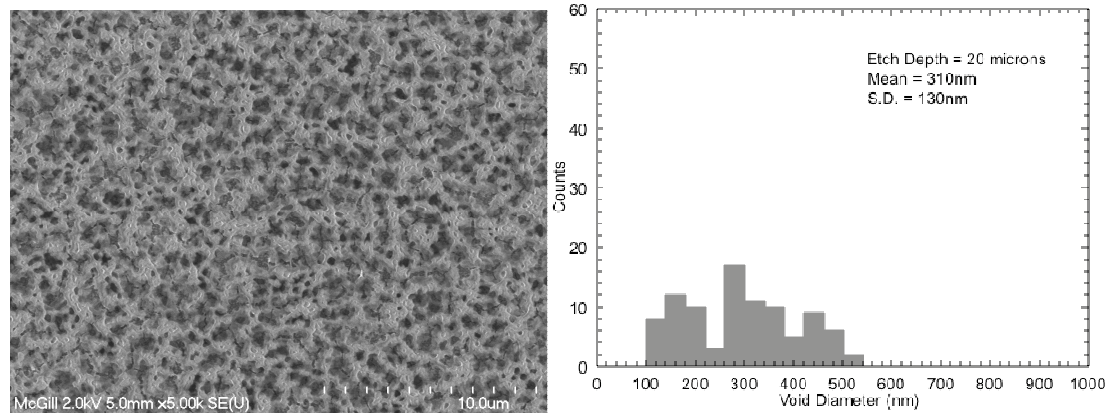

(c) **(d)**

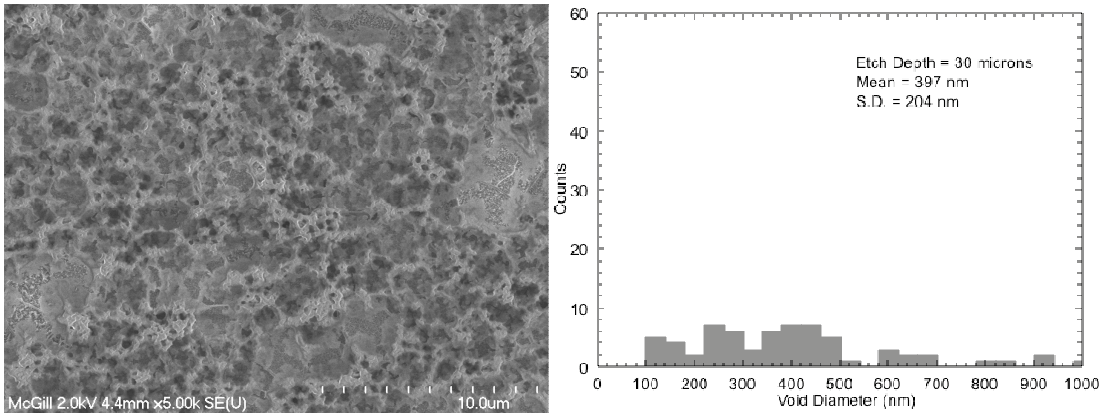

(e) **(f)**

Figure 5-2: SEM images of the fabricated porous silicon samples with various pore sizes using XeF_2 dry etching process. (a) Sample A; (b) Sample B; (c) Sample C.

The etching of the samples to these depths has resulted in porous surfaces with an average pore diameters of 220 nm, 310nm, and 397nm as shown in Figures 5.2(d), (e), and (f) respectively. It is clear from these pore distributions that longer time and deeper etching result in wider pores. To measure the physical thickness directly, we cleaved the 20µm etched sample at the middle of the porous area and imaged its cross-section with a high resolution SEM. Figure 5.2 is a cross section view of the 20µm etched sample which shows that the thickness of the pores are approximately 690nm deep.

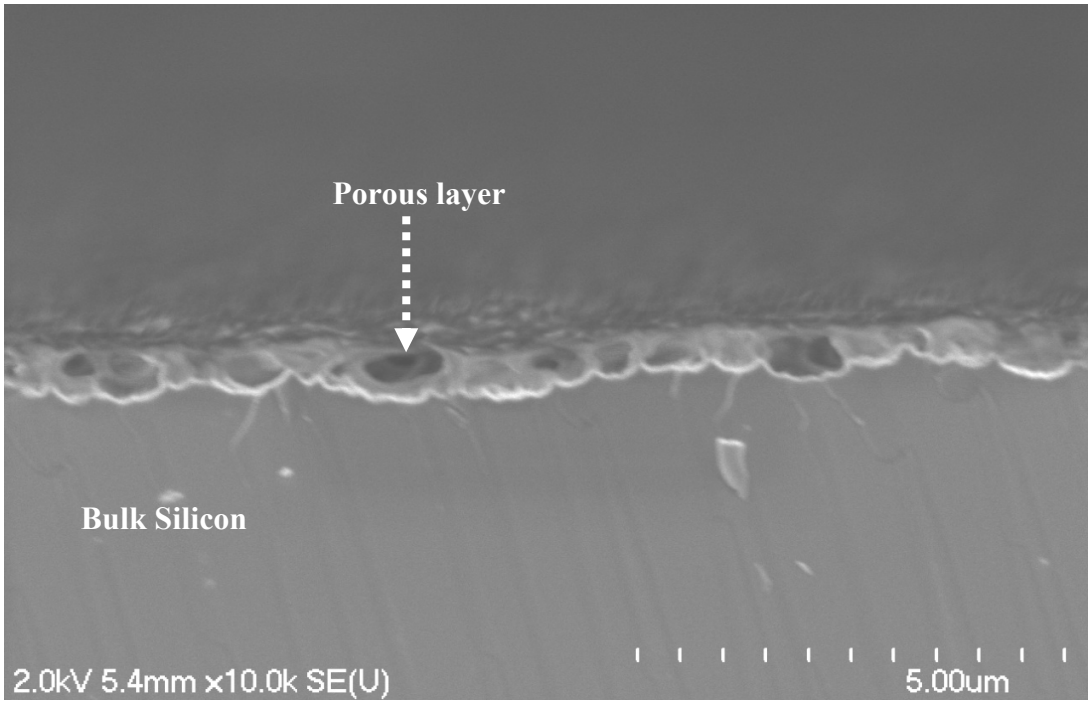

Figure 5-3: Cross-sectional SEM image of the porous silicon material (Sample B).

5.3 Morphology of the Porous Silicon Samples

To investigate the surface morphology of the porous silicon samples, we have taken high resolution SEM images that clearly show the structures that form the pores for each of 10, 20, and 30µm etched samples. Interestingly, as shown in Figures 5.4(a), (b), and (c) the porous structures consist of a top surface represented by the web of nanocrystals and the bottom surface which underlie the web of nanocrystals. The bottom surface of the pores for the 10µm etched sample is flat and has few cracks. These cracks will open up if further etching was performed. For the 20µm etched sample, cracks on the bottom surface are wider and new pores are formed. For the 30µm etched sample, the pores became wider.

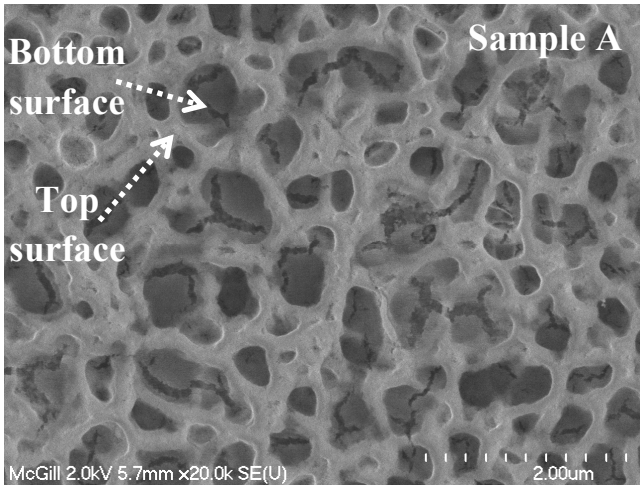

(a)

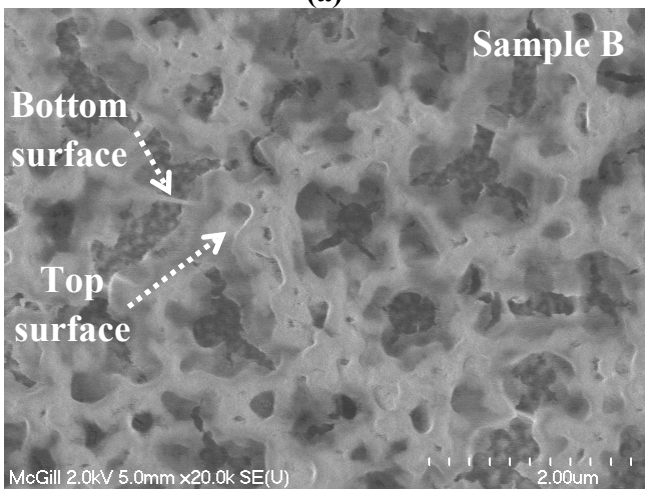

(b)

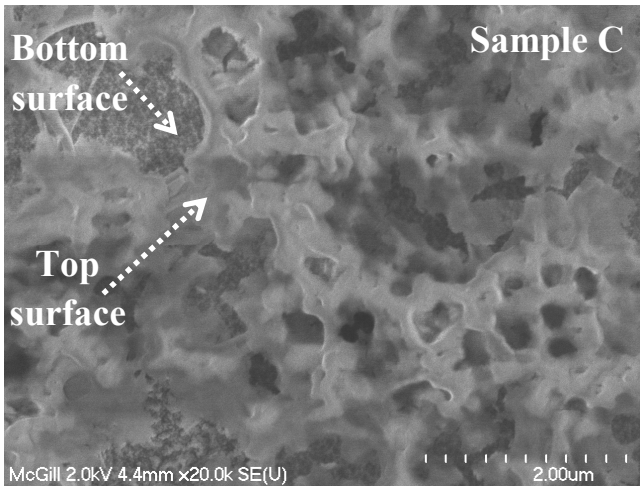

(c)

Figure 5-4: High resolution SEM images showing the top and bottom surface of the pore structures for the porous silicon samples. (a) Sample A; (b) Sample B; (c) Sample C.

5.4 Cell Culture

5.4.1 Materials and Methods

The un-etched silicon and porous silicon were sterilized in 70% ethanol and kept under ultraviolet radiation for one hour. The titanium disks underwent a washing procedure of 72 hours, and autoclaved.

The mice used in this study are 9-10 months of age and of C3H strain. They are sacrificed and the femur is being taken out. Upon centrifuging for 7 seconds at 4000 rpm, the cells are separated from the bone. Since the assay was not going to begin immediately, the cells were subjected to freezing using two solutions, one which consists of 80% amem, 20% Phosphate buffered saline (FBS), and 1% p/s, and the second solution which includes 60% amem, 20% FBS, 20% Dimethyl sulfoxide (DMSO), and 1% p/s. After being kept in a -80^{o}C freezer for about 10 days, the cells are thawed, and plated in 100mm culture dish. Once they have reached 80% confluent, they were ready to be used for the assay. For the first few experiments cells were seeded at an initial density of 50,000/100 µl/sample, however for the last experiments the seeding density was reduce to 30,000/100 µl/sample.

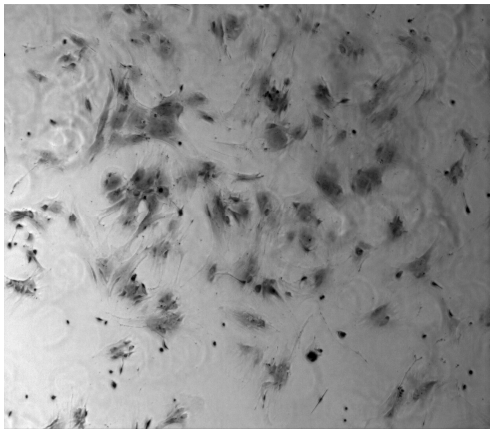

Figure 5-5: Toluidine stain of mesenchymal stem cell on tissue culture plastic day 3, 4X.

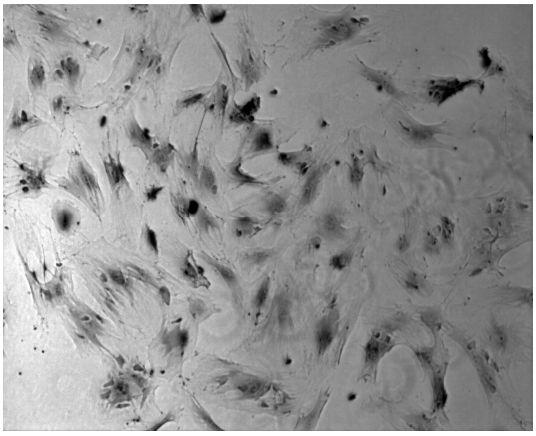

Figure 5-6: Toluidine stained mesenchymal stem cell of tissue control plastic, day 6 4X.

The cells were plated in the center of the disks meaning that their concentration was higher in the center than in the peripheral of the wafers. Cells were cultured in growth non-osteogenic medium consisting of 89% minimum essential medium (amem), 10% FBS and 1% p/s for 9 days. The medium was changed every two days in order to maintain a fresh medium for the growing cells.

Different tests were performed on the assay in order to scan the growth of proliferation of the MSC. Alamar blue reagent, scanning electron microscopy, staining with Toluidine Blue, and counting cells in different time points using bright line hemacytometer were among the tests performed.

5.4.2 Results

Five experiments have been preformed. The first four experiments the cells were investigated for six and more time points. Cells were plated on five different templates etched down to 10µm, 20µm, 30µm, 50µm, and 70µm. The culture results showed that the 20µm and 30µm samples possess better ability to promote stable environment for growth and proliferation of mesenchymal stem cell.

The last experiment had only three time points, day 3, 6, and 9. In experiment 4, two plates each containing twelve wells were used, one of the plates contained triplicates of 0µm, 20µm, 30µm etched samples and tissue culture plastic used as the control, the second plate consists of the same types of porous silicon as plate one except that instead of the tissue culture plastic, smooth titanium disks were used. In this experiment, Alamar blue assay was preformed. Indeed Alamar blue is a reagent, shown in Figure 5.7, that reduces upon cell metabolism activity, and the amount reduced is being measured at 560 and 595nm wavelength light by a plate reader.

By looking at the Alamar blue calculations and graph, it is obvious that the cell activity increases until day 9, and then it starts to decrease. The mesenchymal stem cell seems to grow better in the porous silicon wafer of 30µm. The data demonstrate that the cells grow better on the porous silicon wafers as compare to the tissue culture plastic which was used as control.

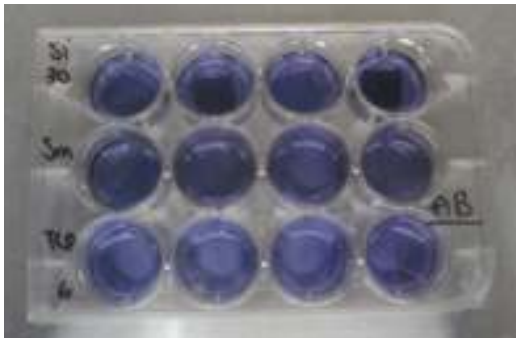

Figure 5-7: Samples immersed in Alamar blue reagent

In experiment 5, porous silicon samples of 20µm and 30µm were used only to be compared with cell activity on smooth titanium disks and tissue culture plastic, aside from Alamar blue test, cell count, scanning electron microscopy and light microscopy pictures were taken from this assay. The Alamar blue calculations show that the cell are growing and proliferating well in the silicon wafers, as compare to the titanium disks and the tissue culture plastic. On the other hand, the cell count demonstrates that the numbers of cells are highest in the tissue culture plastic.

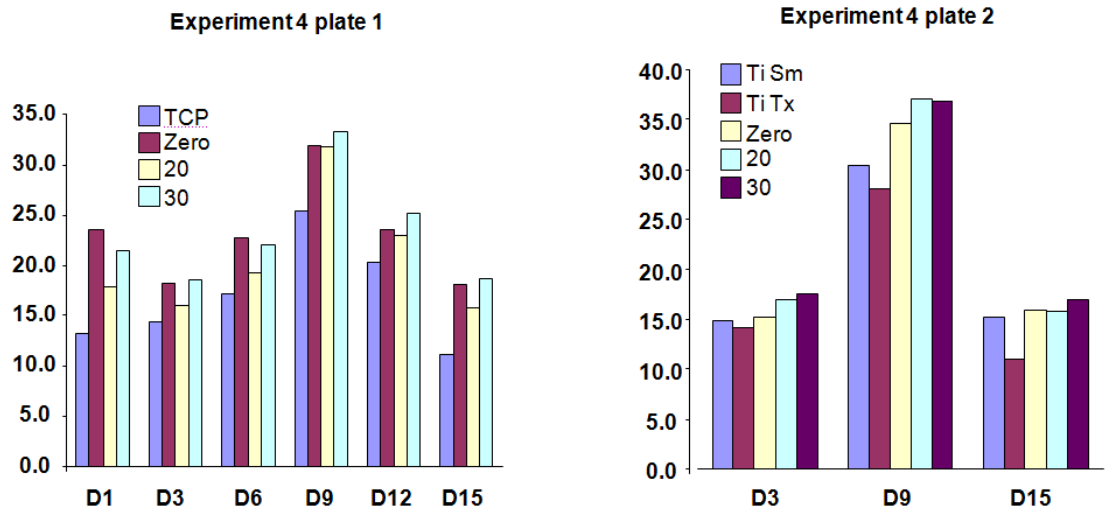

(a) **(b)**

Figure 5-8: (a) This graph demonstrates the Alamar blue calculations for the plate 1 of the experiment four which consisted of triplicates of 0µm, 20µm, 30µm and tissue culture plastic. The right hand side graph; (b) This graph is the calculation taken for measuring the reduction of Alamar blue on a plate that consisted of same types of porous silicon as plate one except that instead of the tissue culture plastic, smooth titanium disks were used. There is a trend of increase in cell activity in both plates up until day 9. The cells grow better on the porous silicon wafers of 30µm pore size compare to the 20µm, 0µm and TCP.

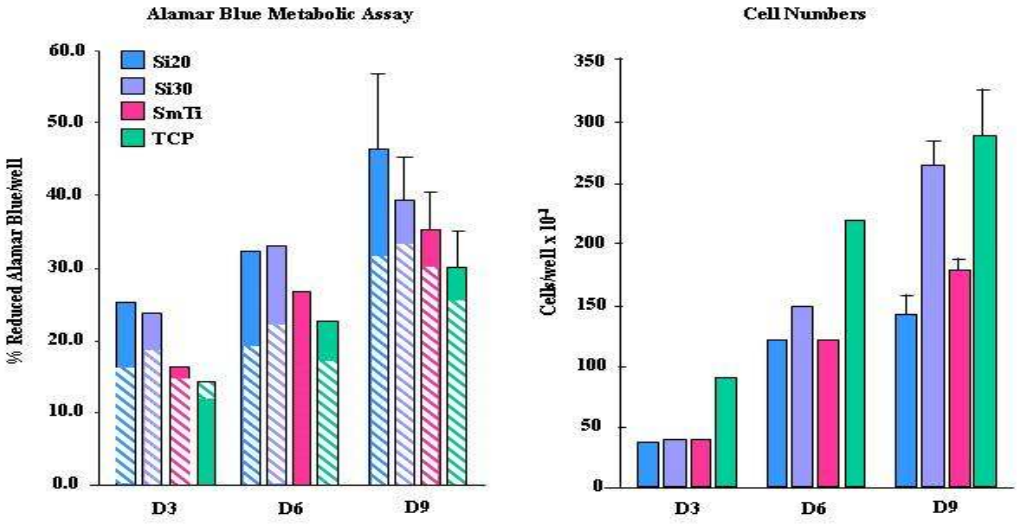

(a) **(b)**

Figure 5-9: (a) This graph demonstrates the Alamar blue calculations done on experiment five which was focused on comparing cell growth on porous silicon wafer with the pore size of 30µm and 20µm with the smooth surfaced titanium

disks and the tissue culture plastic. The results indicate a growing trend of cells until day 9; the cells growth is more efficient on porous silicon of 20µm pore size. The graph on the right side; (b) This graph demonstrates the number of cells counted at three different time intervals. The numbers of cells are increasing up until day 9 and there are more cells located on the tissue culture plastic.

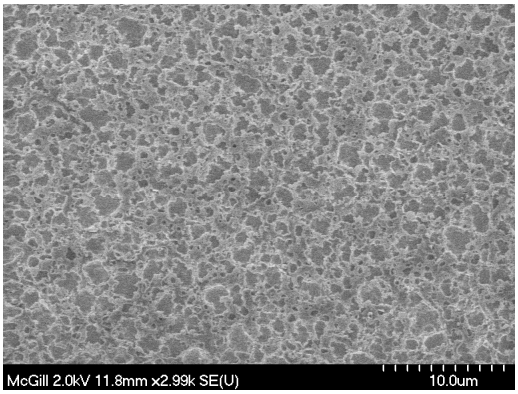

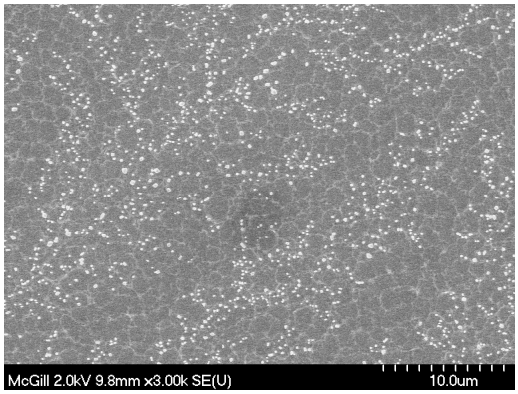

(a) **(b)**

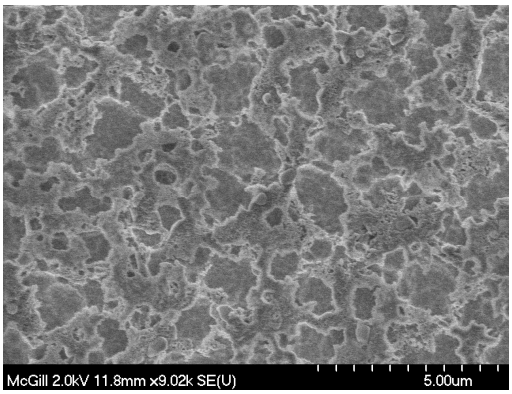

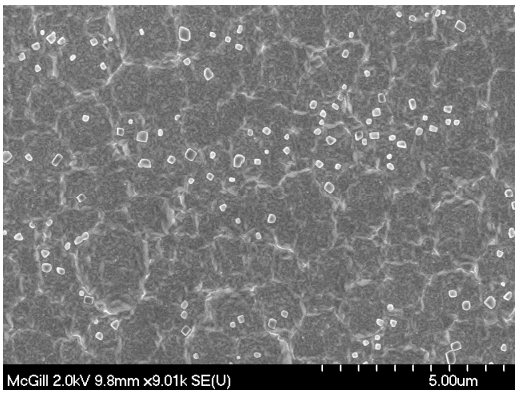

(c) **(d)**

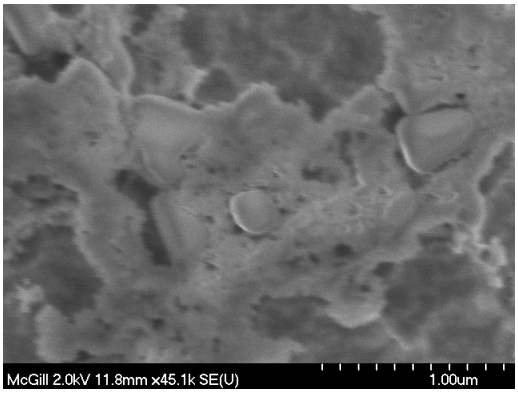

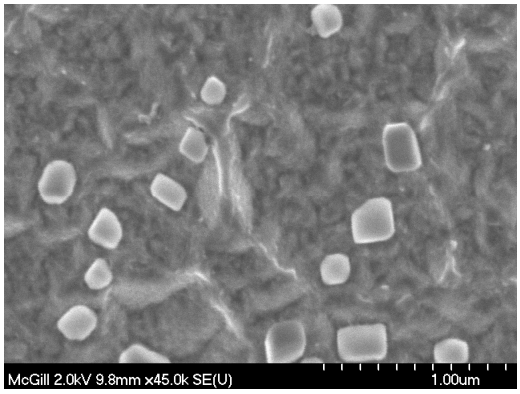

(e) **(f)**

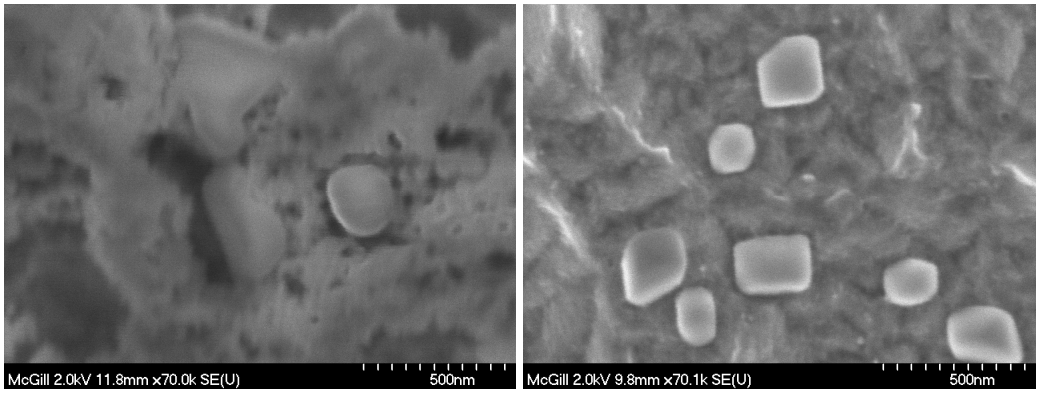

(g) **(h)**

Figure 5-10: High resolution SEM images for stem cells growing on the 20 micron etched porous silicon sample

The scanning electron micrographs in Figure 5.10 depict cell proliferation of pre-osteoblasts within scaffolds of the 20 micron etched sample on days 6 and 9. Figures 5.10(g) and (h), which are taken with high magnification, show that cells are entrapped and growing inside the pores.

5.4.3 Discussion

Although the results of these experiments vary lightly, the reason can be explained clearly. In fact, in experiment 4, cells are showing a trend of increase in proliferation and growth on the porous silicon up until day 9, where they begin to die due to insufficient place on the wafers.

In experiment 5, the Alamar blue results also indicated an increasing trend of cells; however the results from the cell count using bright line hemacytometer disagreed. Indeed, in order to be able to count the cells, the disks should be trypsinized so that the bonds between the cells and the disks break down. For the titanium disks, and the tissue culture plastic, it is simple to break the bond due to the fact that no pores are located on the latter disks. On the other hand, the porous silicon wafers have different pore sizes, in which cells have grown, making it a difficult task to remove the cells

located deep down in the pores. This explains the controversy of the cell count results versus the Alamar blue assay. In this case the Alamar blue assay is the most reliable assay, and it shows that the cells are growing and proliferating well on the porous silicon wafers.

5.5 Summary

This Chapter is based on the paper published by our group entitled "Dry Etch Fabrication of Porous Silicon using Xenon Difluoride", Micro & Nano Letters, January 2010. Maurice Cheung helped to optically characterize the porous silicon samples. The stem cell culture was performed by Maedeh Khayyat Kholghi.

A novel and simple approach to fabricate porous silicon is presented in this chapter. The Xenon Diflouride approach described here is a dry etching based which represents a significant advantage over the previous electrochemical etching processes to form porous silicon. XeF_2 etching technique offers straightforward fabrication process for porous silicon and could benefit other areas such as allowing simple monolithic integration of porous silicon devices with microelectronic circuitry following the current trend of integrated microsystems. The technique is flexible and different control parameters can be employed to tune the pore size and consequently produce porous silicon with attractive biocompatible features. In this Chapter, XeF_2 is employed to produce porous silicon templates behaving as biocompatible material. The different experiments preformed on samples with different porosity and pore sizes demonstrate that the dry etched porous silicon samples are suitable host for the growth and proliferation of the bone marrow derived mesenchymal stem cell of a pthrp mice.

Using XeF_2 the silicon neural probe electrodes can be made porous by simply loading them in the etching chamber and performing the etching process for a well determined time to get the desired porosity. The high etch selectivity of XeF_2 to silicon over photoresist allows us to selectively form porous silicon on a specific area of the neural probes by simply employing a patterned standard hard-baked photoresist layer as a masking layer. The findings reported in this Chapter will allow the development of biologically-friendly devices. The porous silicon material fabricated with XeF_2 could

serve as the bridge that allows signals and information to be transmitted effectively and efficiently between a semiconductor device and a biological system.

CHAPTER 6

CONCLUSION

We have successfully applied MicroElectroMechanical Systems MEMS technology to the development of neural probes to make a new generation of elongated and structurally reinforced neural electrodes that can reach regions located 10 mm deep into the brain. Major technical achievements in process development include employing ultra thin silicon wafers with XeF_2 etching process to fabricate silicon probes and development of a novel process to monolithically integrate optical sensors with the neural probes.

We introduced the concept of reinforcing the regions of the elongated electrodes that are more susceptible to breakage. We show that reinforcing specific regions of the probe with metallic layers pushes the region of maximum stress from the center to the base region of the probe which is typically sturdier. The reinforced probes are fabricated using both custom process using McGill clean-room facilities and the commercial MicraGem process from Micralyne, Inc. Probes with different geometries (different shank length, width, thickness, and tip angle) have been fabricated and mechanically tested in order to determine the best design to make the probes strong enough to penetrate the human pia, and as small as possible to reduce the damage to the brain. We tested the electrode impedance of the probes.

We presented a novel methodology of integrating optical chemical sensors with neural electro-potential recording microelectrodes. We employed xerogel doped with luminescent ruthenium complexes which are responsive to oxygen to monitor brain tissue oxygenation. Xerogel based oxygen sensors are deposited on the core of an optical fiber to serve as integrated sensor waveguides. Promising results from experimental evaluation of the hybrid multimodal neural probe in area 5 in the parietal cortex of a non-human primate proved its functionality

A special fabrication process has been developed to fabricate the multimodal hybrid probes. The use of ultra thin silicon wafers with XeF_2 dry etching technique simplifies the fabrication process and allows an easy integration of the optical biochemical sensors with the silicon neural electrodes. At the same time, XeF_2 offers a dry technique of forming porous silicon electrodes rendering them biocompatible.

The properties of long, reinforced, biocompatible, simple fabrication process, easy integration with optical sensors for neuromarkers monitoring, and elongated Neural electrodes would (1) allow neuroscientists to use hybrid-electrode technology in any part of the brain (2) significantly increase the amount of information available to decode and make a decision (3) open avenues for novel theories of brain function (3) help in providing answers to complex brain diseases and disorders (4) enhance deciphering the nature of the information flow and increase the amount of information available for neural prosthetic applications since both cognitive and motor signals and biomarkers can be simultaneously recorded. And, as a consequence, the number of probes that need to be implanted will be minimized. In near future, these arrays can also benefit other areas of neuroscience research such as in epileptic patients to early detection and prevention of seizures. Finally, microfluidic channels can also be mounted on the arrays to deliver chemotherapy agents to specific and localized tumors anywhere in the brain or elsewhere.

References

[1] Franklin, B., "An Account of the Effects of Electricity in Paralytic Cases. In a Letter to John Pringle, M. D. F. R. S. from Benjamin Franklin, Esq; F. R. S.," *Philosophical Transactions (1683-1775),* vol. 50, pp. 481-483, 1757 - 1758.

[2] McNeal, D. R., "2000 years of electrical stimulation," *Functional Electrical Stimulation. Applications in Neural Prostheses. Biomedical Engineering and Instrumentation Series,* vol. 3, pp. 3-35, 1977.

[3] Hodgkin, A. L. and Huxley, A. F., "Action potentials recorded from inside a nerve fibre," *Nature,* vol. 144, pp. 710-711, Jul-Dec 1939.

[4] Hodgkin, A. L. and Huxley, A. F., "A Quantitative Description of Membrane Current and Its Application to Conduction and Excitation in Nerve," *Journal of Physiology-London,* vol. 117, pp. 500-544, 1952.

[5] Huxley, A. F., "Hodgkin and the action potential 1935-1952," *Journal of Physiology-London,* vol. 538, pp. 2-2, Jan 1 2002.

[6] Gesteland, R. C., Howland, B., Lettvin, J. Y., and Pitts, W. H., "Comments on Microelectrodes," *Proceedings of the Institute of Radio Engineers,* vol. 47, pp. 1856-1862, 1959.

[7] Polikov, V. S., Tresco, P. A., and Reichert, W. M., "Response of brain tissue to chronically implanted neural electrodes," *Journal of Neuroscience Methods,* vol. 148, pp. 1-18, Oct 15 2005.

[8] K. Frank, M. C. B., "Microelectrodes for Recording and Stimulation," *Physical Techniques in Biological Research,* vol. 5, 1964.

[9] Geddes, L. A., "Electrodes and the measurement of bioelectric events," *Wiley-Interscience,* 1972.

[10] Nicolelis, M. A. L., "Brain-machine interfaces to restore motor function and probe neural circuits," *Nature Reviews Neuroscience,* vol. 4, pp. 417-422, May 2003.

[11] Rutten, W. L. C., "Selective electrical interfaces with the nervous system," *Annual Review of Biomedical Engineering,* vol. 4, pp. 407-452, 2002.

[12] Najafi, K., "Solid-State Microsensors for Cortical Nerve Recordings," *IEEE Engineering in Medicine and Biology Magazine,* vol. 13, pp. 375-387, Jun-Jul 1994.

[13] Najafi, K., "Micromachined systems for neurophysiological applications," in *Hand book of microlithography, micromachining, and microfabrication,*. vol. 2, ed: SPIE-International Society for Optical Engine, 1997, pp. 517-569.

[14] Heiduschka, P. and Thanos, S., "Implantable bioelectronic interfaces for lost nerve functions," *Progress in Neurobiology,* vol. 55, pp. 433-461, Aug 1998.

[15] Stieglitz, T. and Meyer, J. U., "Microtechnical interfaces to neurons," *Microsystem Technology in Chemistry and Life Science,* vol. 194, pp. 131-162, 1998.

[16] D. H. Hubel and T. N. Wiesel, "Ferrier Lecture: Functional Architecture of Macaque Monkey Visual Cortex," in *Proceedings of the Royal Society of London*, Biological Sciences, 1977, pp. 1-59.

[17] McLaughlin, D., Shapley, R., Shelley, M., and Wielaard, D. J., "A neuronal network model of macaque primary visual cortex (V1): Orientation selectivity and dynamics in the input layer 4C alpha," *Proceedings of the National Academy of Sciences of the United States of America,* vol. 97, pp. 8087-8092, Jul 5 2000.

[18] Gilbert, C. D., "Adult cortical dynamics," *Physiological Reviews,* vol. 78, pp. 467-485, Apr 1998.

[19] Deadwyler, S. A. and Hampson, R. E., "The significance of neural ensemble codes during behavior and cognition," *Annual Review of Neuroscience,* vol. 20, pp. 217-244, 1997.

[20] Nicolelis, M. A. L., *Methods for Neural Ensemble Recordings*: CRC-Press, 1998.

[21] Normann, R. A., Warren, D. J., Ammermuller, J., Fernandez, E., and Guillory, S., "High-resolution spatio-temporal mapping of visual pathways using multi-electrode arrays," *Vision Research,* vol. 41, pp. 1261-1275, 2001.

[22] Nicolelis, M. A. L. and Ribeiro, S., "Multiellectrode recordings: the next steps," *Current Opinion in Neurobiology,* vol. 12, pp. 602-606, Oct 2002.

[23] Hoffman, K. L. and McNaughton, B. L., "Coordinated reactivation of distributed memory traces in primate neocortex," *Science,* vol. 297, pp. 2070-2073, Sep 20 2002.

[24] Nirenberg, S. and Latham, P. E., "Population coding in the retina," *Current Opinion in Neurobiology,* vol. 8, pp. 488-493, Aug 1998.

[25] Vos, B. P., Wijnants, M., Taeymans, S., and De Schutter, E., "Miniature carrier with six independently moveable electrodes for recording of multiple single-units in the cerebellar cortex of awake rats," *Journal of Neuroscience Methods,* vol. 94, pp. 19-26, Dec 15 1999.

[26] Grumet, A. E., Wyatt, J. L., and Rizzo, J. F., "Multi-electrode stimulation and recording in the isolated retina," *Journal of Neuroscience Methods,* vol. 101, pp. 31-42, Aug 15 2000.

[27] Wilson, M. A., McNaughton, B. L., "Dynamics of the hippocampal ensemble code for space," *Science,* vol. 261, pp. 1055-1058, 1993.

[28] Petersson, P., Holmer, M., Breslin, T., Granmo, M., and Schouenborg, J., "An imaging system for monitoring receptive field dynamics," *Journal of Neuroscience Methods,* vol. 104, pp. 123-131, Jan 15 2001.

[29] Rousche, P. J., Petersen, R. S., Battiston, S., Giannotta, S., and Diamond, M. E., "Examination of the spatial and temporal distribution of sensory cortical activity using a 100-electrode array," *Journal of Neuroscience Methods,* vol. 90, pp. 57-66, Aug 1 1999.

[30] Petersen, R. S. and Diamond, M. E., "Spatial-temporal distribution of whisker-evoked activity in rat somatosensory cortex and the coding of stimulus location," *Journal of Neuroscience,* vol. 20, pp. 6135-6143, Aug 15 2000.

[31] Ghazanfar, A. A., Stambaugh, C. R., and Nicolelis, M. A. L., "Encoding of tactile stimulus location by somatosensory thalamocortical ensembles (vol 20, pg 3761, 2000)," *Journal of Neuroscience,* vol. 20, pp. U6-U6, Jun 15 2000.

[32] Neuenschwander, S., Castelo-Branco, M., and Singer, W., "Synchronous oscillations in the cat retina," *Vision Research,* vol. 39, pp. 2485-2497, Jul 1999.

[33] Prechtl, J. C., "Visual-Motion Induces Synchronous Oscillations in Turtle Visual-Cortex," *Proceedings of the National Academy of Sciences of the United States of America,* vol. 91, pp. 12467-12471, Dec 20 1994.

[34] Prechtl, J. C., Cohen, L. B., Pesaran, B., Mitra, P. P., and Kleinfeld, D., "Visual stimuli induce waves of electrical activity in turtle cortex," *Proceedings of the National Academy of Sciences of the United States of America,* vol. 94, pp. 7621-7626, Jul 8 1997.

[35] Gagne, S. and Plamondon, R., "Open Tip Glass Microelectrodes - Conduction through the Wall at the Tip," *IEEE Transactions on Biomedical Engineering,* vol. 34, pp. 56-61, Jan 1987.

[36] Schanne, O. F., Lavallee, M., Laprade, R., and Gagne, S., "Electrical Properties of Glass Microelectrodes," *Proceedings of the Institute of Electrical and Electronics Engineers,* vol. 56, pp. 1072-&, 1968.

[37] Chowdhur.Tk, "Fabrication of Extremely Fine Glass Micropipette Electrodes," *Journal of Physics E-Scientific Instruments,* vol. 2, pp. 1087-&, 1969.

[38] Kennard, D. W., "Glass microcapillary electrodes used for measuring potential in living tissues," *Electronic Apparatus for Biological Research,* pp. 534–567, 1958.

[39] Robinson, D. A., "Electrical Properties of Metal Microelectrodes," *Proceedings of the Institute of Electrical and Electronics Engineers,* vol. 56, pp. 1065-&, 1968.

[40] Skrzypek, J. and Keller, E., "Manufacture of Metal Microelectrodes with Scanning Electron-Microscope," *IEEE Transactions on Biomedical Engineering,* vol. 22, pp. 435-437, 1975.

[41] Terzuolo, C. A. and Araki, T., "An Analysis of Intra-Versus Extracellular Potential Changes Associated with Activity of Single Spinal Motoneurons," *Annals of the New York Academy of Sciences,* vol. 94, pp. 547-&, 1961.

[42] Scherberger, H., Fineman, I., Musallam, S., Dubowitz, D. J., Bernheim, K. A., Pesaran, B., Corneil, B. D., Gilliken, B., and Andersen, R. A., "Magnetic resonance image-guided implantation of chronic recording electrodes in the macaque intraparietal sulcus," *Journal of Neuroscience Methods,* vol. 130, pp. 1-8, Nov 30 2003.

[43] Musallam, S., Bak, M. J., Troyk, P. R., and Andersen, R. A., "A floating metal microelectrode array for chronic implantation," *Journal of Neuroscience Methods,* vol. 160, pp. 122-127, Feb 15 2007.

[44] Wise, K. D., Angell, J. B., and Starr, A., "An Integrated-Circuit Approach to Extracellular Microelectrodes," *IEEE Transactions on Biomedical Engineering,* vol. Bm17, pp. 238-&, 1970.

[45] Wise, K. D. and Najafi, K., "Microfabrication Techniques for Integrated Sensors and Microsystems," *Science,* vol. 254, pp. 1335-1342, Nov 29 1991.

[46] Banks, D. E., D.J. Balachandran, W. Richards, P.R. , "Microengineered interfaces with the nervous system," *Medical Applications of Microengineering, IEE Colloquium on,* pp. 4/1-4/3, 1996.

[47] G.A. Urban, O. P., F. Olcaytug, "Early Biomems Multi-Sensor Neuroprobes " in *BioMEMS*. vol. 16, G. A. Urban, Ed., ed: Springer US, 2006.

[48] Banks, D., "Neurotechnology," *Engineering Science and Education,* vol. 7, pp. 135-144 1998.

[49] Pearce, T. M. and Williams, J. C., "Microtechnology: Meet neurobiology," *Lab on a Chip,* vol. 7, pp. 30-40, 2007.
[50] D Banks, D. E., "Microengineered Neural Signal Transducers for Peripheral Nerve: Current Work and Future Requirements," in *Medical and biological implant technology*, Nottingham (UK), 1996.
[51] Rousche, P. J., Pellinen, D. S., Pivin, D. P., Williams, J. C., Vetter, R. J., and Kipke, D. R., "Flexible polyimide-based intracortical electrode arrays with bioactive capability," *IEEE Transactions on Biomedical Engineering,* vol. 48, pp. 361-371, Mar 2001.
[52] Metz, S., Bertsch, A., Bertrand, D., and Renaud, P., "Flexible polyimide probes with microelectrodes and embedded microfluidic channels for simultaneous drug delivery and multi-channel monitoring of bioelectric activity," *Biosensors & Bioelectronics,* vol. 19, pp. 1309-1318, May 15 2004.
[53] Stieglitz, T., "Flexible biomedical microdevices with double-sided electrode arrangements for neural applications," *Sensors and Actuators a-Physical,* vol. 90, pp. 203-211, May 20 2001.
[54] Stieglitz, T. and Gross, M., "Flexible BIOMEMS with electrode arrangements on front and back side as key component in neural prostheses and biohybrid systems," *Sensors and Actuators B-Chemical,* vol. 83, pp. 8-14, Mar 15 2002.
[55] Stieglitz, T. B., H. Keller, R. Schuettler, M. Meyer, J.-U. , "Flexible, polyimide-based neural interfaces," in *Microelectronics for Neural, Fuzzy and Bio-Inspired Systems*, Granada, Spain, 1999, pp. 112-119.
[56] Thomas Stieglitz, H. r. B., Martin Schuettler and J.-Uwe Meyer, "Micromachined, Polyimide-Based Devices for Flexible Neural Interfaces " *Biomedical Microdevices,* vol. 2, pp. 283-294, 2000.
[57] Navarro, X., Calvet, S., Rodriguez, F. J., Stieglitz, T., Blau, C., Buti, M., Valderrama, E., and Meyer, J. U., "Stimulation and recording from regenerated peripheral nerves through polyimide sieve electrodes," *Journal of the Peripheral Nervous System,* vol. 3, pp. 91-101, 1998.
[58] Suh, M., Ma, H. T., Zhao, M. R., Sharif, S., and Schwartz, T. H., "Neurovascular coupling and oximetry during epileptic events," *Molecular Neurobiology,* vol. 33, pp. 181-197, Jun 2006.
[59] Pang., C., "Parylene Technology for Neural Probes Applications," Ph.D., Electrical Engineering, California Institute of Technology, California, 2008.
[60] Bear, M. R., Connors, B. W., and Paradiso, M. A., *Neuroscience Exploring the Brain*, 2nd ed. Baltimore: Lippincott Williams and Wilkins, 2001.
[61] Takahashi, H., Suzurikawa, J., Nakao, M., Mase, F., and Kaga, K., "Easy-to-prepare assembly array of tungsten microelectrodes," *IEEE Transactions on Biomedical Engineering,* vol. 52, pp. 952-956, May 2005.
[62] Tsytsarev, V., Taketani, M., Schottler, F., Tanaka, S., and Hara, M., "A new planar multielectrode array: recording from a rat auditory cortex," *Journal of Neural Engineering,* vol. 3, pp. 293-298, Dec 2006.
[63] Schmidt, E. M., Bak, M. J., and Christensen, P., "Laser exposure of Parylene-C insulated microelectrodes," *Journal of Neuroscience Methods,* vol. 62, pp. 89-92, Nov 1995.

[64] Xu, C. Y., Lemon, W., and Liu, C., "Design and fabrication of a high-density metal microelectrode array for neural recording," *Sensors and Actuators a-Physical,* vol. 96, pp. 78-85, Jan 31 2002.

[65] A.B. Frazier, D. P. O. B., M.G. Allen, "Two Dimensional Metallic Microelectrode Arrays for Extracellular Stimulation and Recording of Neurons," in *proceedings of the IEEE Micro. Electro. Mech. Syst*, 1993.

[66] Oka, H., Shimono, K., Ogawa, R., Sugihara, H., and Taketani, M., "A new planar multielectrode array for extracellular recording: application to hippocampal acute slice," *Journal of Neuroscience Methods,* vol. 93, pp. 61-67, Oct 30 1999.

[67] Anon, "Electrodeposition method creates 3-D microstructures," *Chemical Engineering Progress,* vol. 99, pp. 20-20, May 2003.

[68] Motta, P. S. and Judy, J. W., "Multielectrode microprobes for deep-brain stimulation fabricated with a customizable 3-D electroplating process," *IEEE Transactions on Biomedical Engineering,* vol. 52, pp. 923-933, May 2005.

[69] Maciossek, A., "Electrodeposition of 3-D microstructures without moulds," in *Proc. SPIE*, 1996, pp. 275-279.

[70] Petersen, K. E., "Silicon as a Mechanical Material," *Proceedings of the IEEE,* vol. 70, pp. 420-457, 1982.

[71] Najafi, K., *Micromachined Systems for Neurophysiological Applications* vol. II: Micromachining and Microfabrication: SPIE, 1997.

[72] Najafi, K. and Hetke, J. F., "Strength Characterization of Silicon Microprobes in Neurophysiological Tissues," *IEEE Transactions on Biomedical Engineering,* vol. 37, pp. 474-481, May 1990.

[73] Muthuswamy, J., Okandan, M., Jain, T., and Gilletti, A., "Electrostatic microactuators for precise positioning of neural microelectrodes," *IEEE Transactions on Biomedical Engineering,* vol. 52, pp. 1748-1755, Oct 2005.

[74] Ji, J., Najafi, K., and Wise, K. D., "A Scaled Electronically-Configurable Multichannel Recording Array," *Sensors and Actuators a-Physical,* vol. 22, pp. 589-591, Mar 1990.

[75] Tanghe, S. J. and Wise, K. D., "A 16-Channel Cmos Neural Stimulating Array," *IEEE Journal of Solid-State Circuits,* vol. 27, pp. 1819-1825, Dec 1992.

[76] Ji, J., Najafi, K., and Wise, K. D., "A Low-Noise Demultiplexing System for Active Multichannel Microelectrode Arrays," *IEEE Transactions on Biomedical Engineering,* vol. 38, pp. 75-81, Jan 1991.

[77] Ji, J. and Wise, K. D., "An Implantable Cmos Circuit Interface for Multiplexed Microelectrode Recording Arrays," *IEEE Journal of Solid-State Circuits,* vol. 27, pp. 433-443, Mar 1992.

[78] Kim, C. and Wise, K. D., "A 64-site multishank CMOS low-profile neural stimulating probe," *IEEE Journal of Solid-State Circuits,* vol. 31, pp. 1230-1238, Sep 1996.

[79] Kim, C. H. and Wise, K. D., "Low-voltage electronics for the stimulation of biological neural networks using fully complementary BiCMOS circuits," *IEEE Journal of Solid-State Circuits,* vol. 32, pp. 1483-1490, Oct 1997.

[80] Olsson, R. H., Buhl, D. L., Sirota, A. M., Buzsaki, G., and Wise, K. D., "Band-tunable and multiplexed integrated circuits for simultaneous recording and

stimulation with microelectrode arrays," *IEEE Transactions on Biomedical Engineering,* vol. 52, pp. 1303-1311, Jul 2005.

[81] Bai, Q., Wise, K. D., and Anderson, D. J., "A high-yield microassembly structure for three-dimensional microelectrode arrays," *IEEE Transactions on Biomedical Engineering,* vol. 47, pp. 281-289, Mar 2000.

[82] Bai, Q. and Wise, K. D., "Single-unit neural recording with active microelectrode arrays," *IEEE Transactions on Biomedical Engineering,* vol. 48, pp. 911-920, Aug 2001.

[83] Y. Yao, M. N. G., S. Ghimire, J. F. Hetke, and K. D. Wise, "A Low-Profile Three-Dimensional Silicon/Parylene Stimulating Electrode Array for Neural Prosthesis Applications," presented at the IEEE Engineering in Medicine and Biology 27th Annual Conference, Shanghai, China, 2005.

[84] Cheung, K. C., Djupsund, K., Dan, Y., and Lee, L. P., "Implantable multichannel electrode array based on SOI technology," *Journal of Microelectromechanical Systems,* vol. 12, pp. 179-184, Apr 2003.

[85] Wise, K. D., Anderson, D. J., Hetke, J. F., Kipke, D. R., and Najafi, K., "Wireless implantable microsystems: High-density electronic interfaces to the nervous system," *Proceedings of the IEEE,* vol. 92, pp. 76-97, Jan 2004.

[86] Tanghe, S. J., Najafi, K., and Wise, K. D., "A Planar Iro Multichannel Stimulating Electrode for Use in Neural Prostheses," *Sensors and Actuators B-Chemical,* vol. 1, pp. 464-467, Jan 1990.

[87] Najafi, K., Ji, J., and Wise, K. D., "Scaling Limitations of Silicon Multichannel Recording Probes," *IEEE Transactions on Biomedical Engineering,* vol. 37, pp. 1-11, Jan 1990.

[88] Drake, K. L., Wise, K. D., Farraye, J., Anderson, D. J., and Bement, S. L., "Performance of Planar Multisite Microprobes in Recording Extracellular Single-Unit Intracortical Activity," *IEEE Transactions on Biomedical Engineering,* vol. 35, pp. 719-732, Sep 1988.

[89] Hoogerwerf, A. C. and Wise, K. D., "A 3-Dimensional Microelectrode Array for Chronic Neural Recording," *IEEE Transactions on Biomedical Engineering,* vol. 41, pp. 1136-1146, Dec 1994.

[90] Anderson, D. J., Najafi, K., Tanghe, S. J., Evans, D. A., Levy, K. L., Hetke, J. F., Xue, X. L., Zappia, J. J., and Wise, K. D., "Batch-Fabricated Thin-Film Electrodes for Stimulation of the Central Auditory-System," *IEEE Transactions on Biomedical Engineering,* vol. 36, pp. 693-704, Jul 1989.

[91] Chen, J. K. and Wise, K. D., "A silicon probe with integrated microheaters for thermal marking and monitoring of neural tissue," *IEEE Transactions on Biomedical Engineering,* vol. 44, pp. 770-774, Aug 1997.

[92] Hetke, J. F., Lund, J. L., Najafi, K., Wise, K. D., and Anderson, D. J., "Silicon Ribbon Cables for Chronically Implantable Microelectrode Arrays," *IEEE Transactions on Biomedical Engineering,* vol. 41, pp. 314-321, Apr 1994.

[93] Kipke, D. R., Vetter, R. J., Williams, J. C., and Hetke, J. F., "Silicon-substrate intracortical microelectrode arrays for long-term recording of neuronal spike activity in cerebral cortex," *IEEE Transactions on Neural Systems and Rehabilitation Engineering,* vol. 11, pp. 151-155, Jun 2003.

[94] Jones, K. E., Campbell, P. K., and Normann, R. A., "A Glass Silicon Composite Intracortical Electrode Array," *Annals of Biomedical Engineering,* vol. 20, pp. 423-437, 1992.

[95] Campbell, P. K., Jones, K. E., Huber, R. J., Horch, K. W., and Normann, R. A., "A Silicon-Based, 3-Dimensional Neural Interface - Manufacturing Processes for an Intracortical Electrode Array," *IEEE Transactions on Biomedical Engineering,* vol. 38, pp. 758-768, Aug 1991.

[96] Kelly, R. C., Smith, M. A., Samonds, J. M., Kohn, A., Bonds, A. B., Movshon, J. A., and Lee, T. S., "Comparison of recordings from microelectrode arrays and single electrodes in the visual cortex," *Journal of Neuroscience,* vol. 27, pp. 261-264, Jan 10 2007.

[97] C. T. Nordhausen, P. J. R., and R. A. Normann, "Chronic recordings of visually evoked responses using the utah intracortical electrode array," in *Engineering in Medicine and Biology Society*, 1993, pp. 1391-1392.

[98] Rousche, P. J. and Normann, R. A., "Chronic recording capability of the Utah Intracortical Electrode Array in cat sensory cortex," *Journal of Neuroscience Methods,* vol. 82, pp. 1-15, Jul 1 1998.

[99] Rousche, P. J. and Normann, R. A., "Chronic intracortical microstimulation of cat auditory cortex using a 100 penetrating electrode array," *Journal of Physiology-London,* vol. 499P, pp. P87-P88, Feb 1997.

[100] Suner, S., Fellows, M. R., Vargas-Irwin, C., Nakata, G. K., and Donoghue, J. P., "Reliability of signals from a chronically implanted, silicon-based electrode array in non-human primate primary motor cortex," *IEEE Transactions on Neural Systems and Rehabilitation Engineering,* vol. 13, pp. 524-541, Dec 2005.

[101] Normann, R. A., Maynard, E. M., Rousche, P. J., and Warren, D. J., "A neural interface for a cortical vision prosthesis," *Vision Research,* vol. 39, pp. 2577-2587, Jul 1999.

[102] Ensell, G., Banks, D. J., Richards, P. R., Balachandran, W., and Ewins, D. J., "Silicon-based microelectrodes for neurophysiology, micromachined from silicon-on-insulator wafers," *Medical & Biological Engineering & Computing,* vol. 38, pp. 175-179, Mar 2000.

[103] Norlin, P., Kindlundh, M., Mouroux, A., Yoshida, K., and Hofmann, U. G., "A 32-site neural recording probe fabricated by DRIE of SOI substrates," *Journal of Micromechanics and Microengineering,* vol. 12, pp. 414-419, Jul 2002.

[104] Kewley, D. T., Hills, M. D., Borkholder, D. A., Opris, I. E., Maluf, N. I., Storment, C. W., Bower, J. M., and Kovacs, G. T. A., "Plasma-etched neural probes," *Sensors and Actuators a-Physical,* vol. 58, pp. 27-35, Jan 1997.

[105] K. Cheung, L. G., K. Djupsund, D. Yang, and L. P. Lee, "A new neural probe using SOI wafers with topological interlocking mechanisms," *Microtechnologies in Medicine and Biology,* pp. 507-511, 2000.

[106] Kindlundh, M., Norlin, P., and Hofmann, U. G., "A neural probe process enabling variable electrode configurations," *Sensors and Actuators B-Chemical,* vol. 102, pp. 51-58, Sep 1 2004.

[107] Richardson, R. R., Miller, J. A., and Reichert, W. M., "Polyimides as Biomaterials - Preliminary Biocompatibility Testing," *Biomaterials,* vol. 14, pp. 627-635, Jul 1993.

[108] Rodriguez, F. J., Ceballos, D., Schuttler, M., Valero, A., Valderrama, E., Stieglitz, T., and Navarro, X., "Polyimide cuff electrodes for peripheral nerve stimulation," *Journal of Neuroscience Methods,* vol. 98, pp. 105-118, Jun 1 2000.

[109] Seal, B., Otero, T., and Panitch, A., "Polymeric biomaterials for tissue and organ regeneration," *Material Science Engineering,* vol. 34, pp. 147-230, 2000.

[110] J. F. Hetke, J. C. W., D. S. Pellinen, R. J. Vetter, and D. R. Kipke, "3-D Silicon Probe Array with Hybrid Polymer Interconnect for Chronic Cortical Recording," presented at the IEEE EMBS Conference on Neural Engineering, Capri Island, Italy, 2003.

[111] Kipke, J. S. a. D. R., "The role of flexible polymer interconnects in chronic tissue response induced by intracortical microelectrodes - a modeling and an in vivo study," presented at the IEEE EMBS Annual International Conference, New York City, USA, 2006.

[112] Takeuchi, S., Suzuki, T., Mabuchi, K., and Fujita, H., "3D flexible multichannel neural probe array," *Journal of Micromechanics and Microengineering,* vol. 14, pp. 104-107, Jan 2004.

[113] Lee, K. K., He, J. P., Singh, A., Massia, S., Ehteshami, G., Kim, B., and Raupp, G., "Polyimide-based intracortical neural implant with improved structural stiffness," *Journal of Micromechanics and Microengineering,* vol. 14, pp. 32-37, Jan 2004.

[114] Blum, N. A., Carkhuff, B. G., Charles, H. K., Edwards, R. L., and Meyer, R. A., "Multisite Microprobes for Neural Recordings," *IEEE Transactions on Biomedical Engineering,* vol. 38, pp. 68-74, Jan 1991.

[115] Carmena, J. M., Lebedev, M. A., Crist, R. E., O'Doherty, J. E., Santucci, D. M., Dimitrov, D. F., Patil, P. G., Henriquez, C. S., and Nicolelis, M. A. L., "Learning to control a brain-machine interface for reaching and grasping by primates," *Plos Biology,* vol. 1, pp. 193-208, Nov 2003.

[116] Serruya, M. D., Hatsopoulos, N. G., Paninski, L., Fellows, M. R., and Donoghue, J. P., "Instant neural control of a movement signal," *Nature,* vol. 416, pp. 141-142, Mar 14 2002.

[117] Taylor, D. M., Tillery, S. I. H., and Schwartz, A. B., "Direct cortical control of 3D neuroprosthetic devices," *Science,* vol. 296, pp. 1829-1832, Jun 7 2002.

[118] Wessberg, J., Stambaugh, C. R., Kralik, J. D., Beck, P. D., Laubach, M., Chapin, J. K., Kim, J., Biggs, J., Srinivasan, M. A., and Nicolelis, M. A. L., "Real-time prediction of hand trajectory by ensembles of cortical neurons in primates," *Nature,* vol. 408, pp. 361-365, Nov 16 2000.

[119] Musallam, S., Corneil, B. D., Greger, B., Scherberger, H., and Andersen, R. A., "Cognitive control signals for neural prosthetics," *Science,* vol. 305, pp. 258-262, Jul 9 2004.

[120] Andersen, R. A., Burdick, J. W., Musallam, S., Pesaran, B., and Cham, J. G., "Cognitive neural prosthetics," *Trends in Cognitive Sciences,* vol. 8, pp. 486-493, Nov 2004.

[121] Pesaran, B., Musallam, S., and Andersen, R. A., "Cognitive neural prosthetics," *Current Biology,* vol. 16, pp. R77-R80, Feb 7 2006.

[122] Szarowski, D. H., Andersen, M. D., Retterer, S., Spence, A. J., Isaacson, M., Craighead, H. G., Turner, J. N., and Shain, W., "Brain responses to micro-machined silicon devices," *Brain Research,* vol. 983, pp. 23-35, Sep 5 2003.

[123] Wood, N. K., Kaminski, E.J., and Oglesby, R.J, "The significance of implant shape is experimental testing of biological samples: disc vs rod," *J. Biomed. Mater: Res,* vol. 4, pp. 1-12, 1970.

[124] S. R. Taylor, D. F. G., "Effect of surface texture on the soft tissue response to polymer implants," *Journal of Biomedical Materials Research,* vol. 17, pp. 205-227, 1983.

[125] Biran, R., Martin, D. C., and Tresco, P. A., "Neuronal cell loss accompanies the brain tissue response to chronically implanted silicon microelectrode arrays," *Experimental Neurology,* vol. 195, pp. 115-126, Sep 2005.

[126] Burbaud, P., Vital, A., Rougier, A., Bouillot, S., Guehl, D., Cuny, E., Ferrer, X., Lagueny, A., and Bioulac, B., "Minimal tissue damage after stimulation of the motor thalamus in a case of chorea-acanthocytosis," *Neurology,* vol. 59, pp. 1982-1984, December 24, 2002 2002.

[127] Britt, R. H. and Rossi, G. T., "Quantitative-Analysis of Methods for Reducing Physiological Brain Pulsations," *Journal of Neuroscience Methods,* vol. 6, pp. 219-229, 1982.

[128] Fee, M. S., "Active stabilization of electrodes for intracellular recording in awake behaving animals," *Neuron,* vol. 27, pp. 461-468, Sep 2000.

[129] Spataro, L., Dilgen, J., Retterer, S., Spence, A. J., Isaacson, M., Turner, J. N., and Shain, W., "Dexamethasone treatment reduces astroglia responses to inserted neuroprosthetic devices in rat neocortex," *Experimental Neurology,* vol. 194, pp. 289-300, Aug 2005.

[130] Zhong, Y. H. and Bellamkonda, R. V., "Dexamethasone-coated neural probes elicit attenuated inflammatory response and neuronal loss compared to uncoated neural probes," *Brain Research,* vol. 1148, pp. 15-27, May 7 2007.

[131] Zhong, Y. H. and Bellamkonda, R. V., "Controlled release of anti-inflammatory agent alpha-MSH from neural implants," *Journal of Controlled Release,* vol. 106, pp. 309-318, Sep 2 2005.

[132] Kennedy, P. R., "The Cone Electrode - a Long-Term Electrode That Records from Neurites Grown onto Its Recording Surface," *Journal of Neuroscience Methods,* vol. 29, pp. 181-193, Sep 1989.

[133] Moxon, K. A., Kalkhoran, N. M., Markert, M., Sambito, M. A., McKenzie, J. L., and Webster, J. T., "Nanostructured surface modification of ceramic-based microelectrodes to enhance biocompatibility for a direct brain-machine interface," *IEEE Transactions on Biomedical Engineering,* vol. 51, pp. 881-889, Jun 2004.

[134] Sun, W., Puzas, J. E., Sheu, T. J., and Fauchet, P. M., "Porous silicon as a cell interface for bone tissue engineering," *Physica Status Solidi A-Applications and Materials Science,* vol. 204, pp. 1429-1433, 2007.

[135] Sun, W., Puzas, J. E., Sheu, T. J., and Fauchet, P. M., "Nano-to-microscale porous silicon as a cell interface for bone tissue engineering," *Advanced Materials,* vol. 19, pp. 921-924, 2007.

[136] Thomas, V., Dean, D. R., and Vohra, Y. K., "Nanostructured Biomaterials for regenerative medicine," *Current Nanoscience,* vol. 2, 2006.

[137] Najafi, K., Wise, K. D., and Mochizuki, T., "A High-Yield Ic-Compatible Multichannel Recording Array," *IEEE Transactions on Electron Devices,* vol. 32, pp. 1206-1211, 1985.
[138] Andersen, R. A. and Buneo, C. A., "Intentional maps in posterior parietal cortex," *Annual Review of Neuroscience,* vol. 25, pp. 189-220, 2002.
[139] wikipedia. *http://en.wikipedia.org/wiki/Dura_mater*. Available: http://en.wikipedia.org/wiki/Dura_mater
[140] Benham, F. V. W. a. P. P., *Mechanics of Solids and Strength of Materials*. London: Pitman, 1965.
[141] Timoshenko, J. M. G. a. S. P., *Mechanics of Materials*. Boston: PWS-KENT, 1990.
[142] Moxon, K. A., Leiser, S. C., Gerhardt, G. A., Barbee, K. A., and Chapin, J. K., "Ceramic-based multisite electrode arrays for chronic single-neuron recording," *IEEE Transactions on Biomedical Engineering,* vol. 51, pp. 647-656, Apr 2004.
[143] Timoshenko, S. P., *Theory of Elastic Stability*, 2 ed. New York: McGraw-Hill, 1961.
[144] Dinnik, A. N., "Design of columns of varying cross sections," *Trans, ASME* pp. 105-114, 1929.
[145] Watson, G. N., *Theory of Bessel's Functions*: Cambridge, 1922.
[146] Jensen, W., Yoshida, K., and Hofmann, U. G., "In-vivo implant mechanics of flexible, silicon-based ACREO microelectrode arrays in rat cerebral cortex," *IEEE Transactions on Biomedical Engineering,* vol. 53, pp. 934-940, May 2006.
[147] Wilson, C. J. and Beck, P. A., "Fracture testing of bulk silicon microcantilever beams subjected to a side load," *Journal of Microelectromechanical Systems,* vol. 5, pp. 142-150, Sep 1996.
[148] CoventorWare, "http://www.coventor.com."
[149] Micralyne, "http://www.micralyne.com/," October 5.
[150] Pearson, G. L., Read, W. T., and Feldmann, W. L., "Deformation and Fracture of Small Silicon Crystals," *Acta Metallurgica,* vol. 5, pp. 181-191, 1957.
[151] Bally, M., Halter, M., Voros, J., and Grandin, H. M., "Optical microarray biosensing techniques," *Surface and Interface Analysis,* vol. 38, pp. 1442-1458, Nov 2006.
[152] Ligler, F. S., Sapsford, K. E., Golden, J. P., Shriver-Lake, L. C., Taitt, C. R., Dyer, M. A., Barone, S., and Myatt, C. J., "The array biosensor: Portable, automated systems," *Analytical Sciences,* vol. 23, pp. 5-10, Jan 2007.
[153] Luppa, P. B., Sokoll, L. J., and Chan, D. W., "Immunosensors - principles and applications to clinical chemistry," *Clinica Chimica Acta,* vol. 314, pp. 1-26, Dec 2001.
[154] Nabok, A. V., "Planar Silicon Nitride Waveguides for Biosensing," *IEE Proc. Nanobiotechnol.,* vol. 150, pp. 25-30, 2003.
[155] Ligler, F. and Taitt, C. A. R., *Optical Biosensors: Present and Future*: Elsevier Science Ltd., 2003.
[156] Duveneck, G. L., Abel, A. P., Bopp, M. A., Kresbach, G. M., and Ehrat, M., "Planar waveguides for ultra-high sensitivity of the analysis of nucleic acids," *Analytica Chimica Acta,* vol. 469, pp. 49-61, Sep 26 2002.

[157] Narayanaswamy, R. and Wolfbeis, O. S., *Optical Sensors: Industrial, Environmental and Diagnostic Applications*. New York: Springer, 2004.
[158] McDonagh, C., Burke, C. S., and MacCraith, B. D., "Optical chemical sensors," *Chemical Reviews,* vol. 108, pp. 400-422, 2008.
[159] Wolfbeis, O. S., "Fiber-optic chemical sensors and biosensors," *Analytical Chemistry,* vol. 78, pp. 3859-3873, Jun 15 2006.
[160] Sapsford, K. E., Shubin, Y. S., Delehanty, J. B., Golden, J. P., Taitt, C. R., Shriver-Lake, L. C., and Ligler, F. S., "Fluorescence-based array biosensors for detection of biohazards," *Journal of Applied Microbiology,* vol. 96, pp. 47-58, 2004.
[161] Chodavarapu, V. P., Bukowski, R. M., Kim, S. J., Titus, A. H., Cartwright, A. N., and Bright, F. V., "Multi-sensor system based on phase detection, an LED array, and luminophore-doped xerogels," *Electronics Letters,* vol. 41, pp. 1031-1033, SEP 1 2005.
[162] Cho, E. J. and Bright, F. V., "Optical sensor array and integrated light source," *Analytical Chemistry,* vol. 73, pp. 3289-3293, Jul 15 2001.
[163] Lee, K. S., Lee, H. L. T., and Ram, R. J., "Polymer waveguide backplanes for optical sensor interfaces in microfluidics," *Lab on a Chip,* vol. 7, pp. 1539-1545, 2007.
[164] Kuhn, M., Napporn, T., Meunier, M., Vengallatore, S., and Therriault, D., "Direct-write microfabrication of single-chamber micro solid oxide fuel cells," *Journal of Micromechanics and Microengineering,* vol. 18, pp. -, Jan 2008.
[165] Lewis, J. A., "Direct-write assembly of ceramics from colloidal inks," *Current Opinion in Solid State & Materials Science,* vol. 6, pp. 245-250, Jun 2002.
[166] Therriault, D., Shepherd, R. F., White, S. R., and Lewis, J. A., "Fugitive inks for direct-write assembly of three-dimensional microvascular networks," *Advanced Materials,* vol. 17, pp. 395-+, Feb 23 2005.
[167] Ghafar-Zadeh, E., Sawan, M., and Therriault, D., "Novel direct-write CMOS-based laboratory-on-chip: Design, assembly and experimental results," *Sensors and Actuators a-Physical,* vol. 134, pp. 27-36, Feb 29 2007.
[168] Pique, A. and Chrisey, D. B., *Direct Write Technologies for Rapid Prototyping Applications: In Sensors, Electronics and Integrated Power Sources*. San Diego, USA: Academic Press, 2002.
[169] Madou, M. J., Morrison, S.R., *Chemical Sensing With Solid State Devices*. San Diego: Academic Press, Inc., 1989.
[170] Lakowicz, J. R., *Principles of Fluorescence Spectroscopy*, 2 ed. New York: Kluwer Academic/Plenum Publishers, 1999.
[171] Cho, E. J., Tao, Z. Y., Tehan, E. C., and Bright, F. V., "Multianalyte pin-printed biosensor arrays based on protein-doped xerogels," *Analytical Chemistry,* vol. 74, pp. 6177-6184, Dec 15 2002.
[172] MacCraith, B. D., McDonagh, C., Mcevoy, A. K., Butler, T., OKeeffe, G., and Murphy, V., "Optical chemical sensors based on sol-gel materials: Recent advances and critical issues," *Journal of Sol-Gel Science and Technology,* vol. 8, pp. 1053-1061, 1997.
[173] Jeronimo, P. C. A., Araujo, A. N., and Montenegro, M. C. B. S. M., "Optical sensors and biosensors based on sol-gel films," *Talanta,* vol. 72, pp. 13-27, Apr 15 2007.

[174] Chodavarapu, V. P., Shubin, D. O., Bukowski, R. M., Titus, A. H., Cartwright, A. N., and Bright, F. V., "CMOS-based phase fluorometric oxygen sensor system," *IEEE Transactions on Circuits and Systems I-Regular Papers,* vol. 54, pp. 111-118, Jan 2007.

[175] Aubonnet, S., Barry, H. F., von Bultzingslowen, C., Sabattie, J. M., and MacCraith, B. D., "Photo-patternable optical chemical sensors based on hybrid sol-gel materials," *Electronics Letters,* vol. 39, pp. 913-914, Jun 12 2003.

[176] Burke, C. S., Polerecky, L., and MacCraith, B. D., "Design and fabrication of enhanced polymer waveguide platforms for absorption-based optical chemical sensors," *Measurement Science & Technology,* vol. 15, pp. 1140-1145, Jun 2004.

[177] Lavers, C. R., Itoh, K., Wu, S. C., Murabayashi, M., Mauchline, I., Stewart, G., and Stout, T., "Planar optical waveguides for sensing applications," *Sensors and Actuators B-Chemical,* vol. 69, pp. 85-95, Sep 10 2000.

[178] Boisde, G. and Harmer, A., *Chemical and Biochemical Sensing With Optical Fibers and Waveguides*. Boston: Artech House, 1996.

[179] Maccraith, B. D., Mcdonagh, C. M., Okeeffe, G., Mcevoy, A. K., Butler, T., and Sheridan, F. R., "Sol-Gel Coatings for Optical Chemical Sensors and Biosensors," *Sensors and Actuators B-Chemical,* vol. 29, pp. 51-57, OCT 1995.

[180] Burke, C. S., McGaughey, O., Sabattie, J. M., Barry, H., McEvoy, A. K., McDonagh, C., and MacCraith, B. D., "Development of an integrated optic oxygen sensor using a novel, generic platform," *Analyst,* vol. 130, pp. 41-45, 2005.

[181] Lei, B. F., Li, B., Zhang, H. R., Lu, S. Z., Zheng, Z. H., Li, W. L., and Wang, Y., "Mesostructured silica chemically doped with Ru-II as a superior optical oxygen sensor," *Advanced Functional Materials,* vol. 16, pp. 1883-1891, Sep 18 2006.

[182] Tang, Y., Tehan, E. C., Tao, Z. Y., and Bright, F. V., "Sol-gel-derived sensor materials that yield linear calibration plots, high sensitivity, and long-term stability," *Analytical Chemistry,* vol. 75, pp. 2407-2413, May 15 2003.

[183] Raichle, M. E. and Mintun, M. A., "Brain work and brain imaging," *Annual Review of Neuroscience,* vol. 29, pp. 449-476, 2006.

[184] Grinvald, A., Slovin, H., and Vanzetta, I., "Non-invasive visualization of cortical columns by fMRI," *Nature Neuroscience,* vol. 3, pp. 105-107, Feb 2000.

[185] Malonek, D. and Grinvald, A., "Interactions between electrical activity and cortical microcirculation revealed by imaging spectroscopy: Implications for functional brain mapping," *Science,* vol. 272, pp. 551-554, Apr 26 1996.

[186] Thompson, J. K., Peterson, M. R., and Freeman, R. D., "Single-neuron activity and tissue oxygenation in the cerebral cortex," *Science,* vol. 299, pp. 1070-1072, Feb 14 2003.

[187] Thompson, J. K., Peterson, M. R., and Freeman, R. D., "High-resolution neurometabolic coupling revealed by focal activation of visual neurons," *Nature Neuroscience,* vol. 7, pp. 919-920, Sep 2004.

[188] Khine, M. T., J.K.; Bierer, S.M.; Altamirano, L.J.; Freeman, R.D.; Lee, L.P., "A combined neural-oxygen sensing multi-channel electrode array," presented at the IEEE EMBS Conference on Neural Engineering, 2003.
[189] Hajjhassan, M., Codavarapu, V., Musallam, S., "NeuroMEMS: Neural Probe Microtechnologies," *Sensors,* vol. 8, pp. 6704-6726, 2008.
[190] Hajj-Hassan, M., Chodavarapu, V. P., and Musallam, S., "Microfabrication of ultra-long reinforced silicon neural electrodes," *Micro & Nano Letters,* vol. 4, pp. 53-58, Mar 2009.
[191] Hajj-Hassan, M., Chodavarapu, V., and Musallam, S., "Reinforced silicon neural microelectrode array fabricated using a commercial MEMS process," *Journal of Micro-Nanolithography Mems and Moems,* vol. 8, pp. -, Jul-Sep 2009.
[192] Hajj-Hassan, M., Gonzalez, T., Ghafar-Zadeh, E., Djeghelian, H., Chodavarapu, V., Andrews, M., and Therriault, D., "Direct-Dispense Polymeric Waveguides Platform for Optical Chemical Sensors," *Sensors,* vol. 8, pp. 7636-7648, 2008.
[193] Tang, Y., Tao, Z. Y., Bukowski, R. M., Tehan, E. C., Karri, S., Titus, A. H., and Bright, F. V., "Tailored xerogel-based sensor arrays and artificial neural networks yield improved O-2 detection accuracy and precision," *Analyst,* vol. 131, pp. 1129-1136, 2006.
[194] Canham, L. T., *Properties of Porous Silicon*. London: Inspec, IEE, 1997.
[195] Feng, Z. C., Tsu, R. , *Porous Silicon*: World Scientific Pub Co Inc, 1994.
[196] Canham, L. T., "Silicon Quantum Wire Array Fabrication by Electrochemical and Chemical Dissolution of Wafers," *Applied Physics Letters,* vol. 57, pp. 1046-1048, Sep 3 1990.
[197] Cullis, A. G., Canham, L. T., and Calcott, P. D. J., "The structural and luminescence properties of porous silicon," *Journal of Applied Physics,* vol. 82, pp. 909-965, Aug 1 1997.
[198] Foll, H., Christophersen, M., Carstensen, J., and Hasse, G., "Formation and application of porous silicon," *Materials Science & Engineering R-Reports,* vol. 39, pp. 93-141, Nov 1 2002.
[199] Martin-Palma, R. J., Herrero, P., Guerrero-Lemus, R., Moreno, J. D., and Martinez-Duart, J. M., "Cross-section TEM and optical characterization of porous silicon multilayer stacks," *Journal of Materials Science Letters,* vol. 17, pp. 845-847, May 15 1998.
[200] Berger, M. G., Dieker, C., Thonissen, M., Vescan, L., Luth, H., Munder, H., Theiss, W., Wernke, M., and Grosse, P., "Porosity Superlattices - a New Class of Si Heterostructures," *Journal of Physics D-Applied Physics,* vol. 27, pp. 1333-1336, Jun 14 1994.
[201] Saha, H. and Pramanik, C., "Porous silicon-based sensors: Prospects and challenges," *Materials and Manufacturing Processes,* vol. 21, pp. 239-246, Mar-Apr 2006.
[202] Foucaran, A., PascalDelannoy, F., Giani, A., Sackda, A., Combette, P., and Boyer, A., "Porous silicon layers used for gas sensor applications," *Thin Solid Films,* vol. 297, pp. 317-320, Apr 1 1997.
[203] Sailor, M. J. and Link, J. R., ""Smart dust": nanostructured devices in a grain of sand," *Chemical Communications,* pp. 1375-1383, 2005.

[204] Stewart, M. P. and Buriak, J. M., "Chemical and biological applications of porous silicon technology," *Advanced Materials,* vol. 12, pp. 859-869, Jun 16 2000.
[205] Williams, R. A. and Blanch, H. W., "Covalent Immobilization of Protein Monolayers for Biosensor Applications," *Biosensors & Bioelectronics,* vol. 9, pp. 159-167, 1994.
[206] Janshoff, A., Dancil, K. P. S., Steinem, C., Greiner, D. P., Lin, V. S. Y., Gurtner, C., Motesharei, K., Sailor, M. J., and Ghadiri, M. R., "Macroporous p-type silicon Fabry-Perot layers. Fabrication, characterization, and applications in biosensing," *Journal of the American Chemical Society,* vol. 120, pp. 12108-12116, Nov 25 1998.
[207] Chan, S., Fauchet, P. M., Li, Y., Rothberg, L. J., and Miller, B. L., "Porous silicon microcavities for biosensing applications," *Physica Status Solidi a-Applied Research,* vol. 182, pp. 541-546, Nov 2000.
[208] Coffer, J. L., Whitehead, M. A., Nagesha, D. K., Mukherjee, P., Akkaraju, G., Totolici, M., Saffie, R. S., and Canham, L. T., "Porous silicon-based scaffolds for tissue engineering and other biomedical applications," *Physica Status Solidi a-Applications and Materials Science,* vol. 202, pp. 1451-1455, Jun 2005.
[209] Anglin, E. J., Cheng, L. Y., Freeman, W. R., and Sailor, M. J., "Porous silicon in drug delivery devices and materials," *Advanced Drug Delivery Reviews,* vol. 60, pp. 1266-1277, Aug 17 2008.
[210] Pavesi, L. and Dubos, P., "Random porous silicon multilayers: Application to distributed Bragg reflectors and interferential Fabry-Perot filters," *Semiconductor Science and Technology,* vol. 12, pp. 570-575, May 1997.
[211] Strehlke, S., Bastide, S., and Levy-Clement, C., "Optimization of porous silicon reflectance for silicon photovoltaic cells," in *Sol Energ Mat Sol C* vol. 58, ed, 1999, pp. 399-409.
[212] Lammel, G., Schweizer, S., Schiesser, S., and Renaud, P., "Tunable optical filter of porous silicon as key component for a MEMS spectrometer," *Journal of Microelectromechanical Systems,* vol. 11, pp. 815-828, Dec 2002.
[213] Berger, M. G., Thonissen, M., Arensfischer, R., Munder, H., Luth, H., Arntzen, M., and Theiss, W., "Investigation and Design of Optical-Properties of Porosity Superlattices," *Thin Solid Films,* vol. 255, pp. 313-316, Jan 15 1995.
[214] Striemer, C. C., Gaborski, T. R., McGrath, J. L., and Fauchet, P. M., "Charge- and size-based separation of macromolecules using ultrathin silicon membranes," *Nature,* vol. 445, pp. 749-753, Feb 15 2007.
[215] de Vasconcelos, E. A., da Silva, E.F., Santos, B.D., de Azevedo, W.M., Freire,J.A.K., "A new method for luminescent porous silicon formation: reaction-induced vaporphase stain etch," *Phys. Status Solidi A—Appl. Mat,* vol. 202, pp. 1539–1542, 2005.
[216] Smith, R. L. and Collins, S. D., "Porous Silicon Formation Mechanisms," *Journal of Applied Physics,* vol. 71, pp. R1-R22, Apr 15 1992.
[217] Escorcia-Garcia, J., Sarracino Martínez, O., Gracia-Jiménez, J. M. and Agarwal, V., "Porous silicon photonic devices using pulsed anodic etching of

lightly doped silicon," *Journal of Physics D: Applied,* vol. 42, p. 145101 (7pp), 2009.

[218] Nakagawa, T., Koyama, H., and Koshida, N., "Control of structure and optical anisotropy in porous Si by magnetic-field assisted anodization," *Applied Physics Letters,* vol. 69, pp. 3206-3208, Nov 18 1996.

[219] Winters, H. F. and Coburn, J. W., "Etching of Silicon with Xef2 Vapor," *Applied Physics Letters,* vol. 34, pp. 70-73, 1979.

[220] Patel, S. R., Schaadt, G. P., Macdonald, D. B., Shi, H., Huibers, A.G., Heureux, P., "Method for vapor phase etching of silicon," 2002.

[221] Arana, L. R., de Mas, N., Schmidt, R., Franz, A. J., Schmidt, M. A., and Jensen, K. F., "Isotropic etching of silicon in fluorine gas for MEMS micromachining," *Journal of Micromechanics and Microengineering,* vol. 17, pp. 384-392, Feb 2007.

[222] Engstrom, J. R., Nelson, M. M., and Engel, T., "The Adsorption and Reaction of Fluorine on the Si(100) Surface," *Surface Science,* vol. 215, pp. 437-500, May 1989.

[223] Vugts, M. J. M., Eurlings, M. F. A., Hermans, L. J. F., and Beijerinck, H. C. W., "Si/XeF2 etching: Reaction layer dynamics and surface roughening," *Journal of Vacuum Science & Technology a-Vacuum Surfaces and Films,* vol. 14, pp. 2780-2789, Sep-Oct 1996.